IAEA-TECDOC-1190

Instrumentation for PIXE and RBS

INTERNATIONAL ATOMIC ENERGY AGENCY IAEA

December 2000

The originating Section of this publication in the IAEA was:

Physics Section
International Atomic Energy Agency
Wagramer Strasse 5
P.O. Box 100
A-1400 Vienna, Austria

INSTRUMENTATION FOR PIXE AND RBS
IAEA, VIENNA, 2000
IAEA-TECDOC-1190
ISSN 1011–4289

Printed by the IAEA in Austria
December 2000

FOREWORD

During the past two decades the IAEA has assisted many national laboratories in its Member States in various fields where nuclear analytical methods based on ion beams have been applied. This assistance has been realised through Technical Co-operation (TC) projects, Co-ordinated Research Projects (CRPs) and other IAEA activities. The IAEA has provided low energy accelerator systems for ion beam analysis to several laboratories in developing countries. On many occasions the existing accelerator systems have been upgraded, and in many cases only measuring equipment for beam lines (end stations) has been provided, together with fellowships and expert visits. Among the range of ion beam nuclear analytical methods, the particle induced X ray emission (PIXE) and Rutherford backscattering spectrometry (RBS) are the most frequently used techniques. The successful application of these techniques depends in great extent on the proper understanding of the instrumentation needed for analysis. The purpose of this TECDOC is to give an overview of instrumentation for PIXE and RBS, including hardware and software needed to perform the analysis. The other, more general aspects of these techniques, including the physical background and analysis of application areas, are not subjects of this TECDOC.

This TECDOC will be useful to students, operators and technical staff involved in the production and maintenance of instrumentation for PIXE and RBS, staff involved in technical aspects of data analysis, and also project managers who might be involved in setting up a project in this field or involved in the process of purchasing equipment and software for such projects. In this sense, it could be useful for better implementation of TC projects related to the utilisation of small accelerators for material analysis.

The IAEA is grateful to M. Jakšić for drafting the sections related to the PIXE instrumentation, and to F. Pászti and A. Kótai for their contributions in drafting the RBS part. S. Fazinic of the Division of Physical and Chemical Sciences was the IAEA officer responsible for this publication.

EDITORIAL NOTE

The use of particular designations of countries or territories does not imply any judgement by the publisher, the IAEA, as to the legal status of such countries or territories, of their authorities and institutions or of the delimitation of their boundaries.

The mention of names of specific companies or products (whether or not indicated as registered) does not imply any intention to infringe proprietary rights, nor should it be construed as an endorsement or recommendation on the part of the IAEA.

CONTENTS

1. INTRODUCTION

The full range of analytical techniques with ion beams includes many methods based on the same principles: firstly, a beam of MeV ions is aimed at the sample. These projectiles penetrate, losing energy continuously at a well-known rate. Along their trajectories there is the chance for collisions with nuclei and with electrons. Secondly, the products of these interactions are emitted from the sample, with probabilities determined by the respective interaction cross-sections, and are finally measured and collected as spectra carrying information on the chemical composition of the sample and the elemental depth distributions.

With PIXE (particle induced X ray emission) one measures X rays arising from the filling of inner-shell vacancies produced by the projectiles. The X ray energies are characteristic for the respective elements.

In RBS (Rutherford backscattering spectrometry) one records projectiles elastically backscattered from nuclei of sample atoms. The measured energy depends on the mass of the target nucleus (and thus on the element or isotope) and also on the depth of the scattering event beneath the surface.

ERDA (elastic recoil detection analysis) is also based on elastic scattering. One records the target nuclei recoiled by the scattering of projectiles. The measured energy depends on the mass of the recoil and on the depth of the scattering event.

NRA (nuclear reaction analysis) relies on the measurement of the products (p, d, α, γ, etc.) of nuclear reactions between projectile and target nuclei. The recorded energy of the products gives information on the specific target nucleus and, in general on the depth of the reaction event.

In addition, there are many other techniques, as for example particle induced gamma ray emission (PIGE), charged particle activation analysis (CPAA), scanning transmission ion microscopy (STIM), Ionoluminescence and ion beam induced charge imaging (IBIC).

Many of these techniques may be applied simultaneously. For example, PIXE, RBS, ERDA, NRA and PIGE instrumentation may all be installed in the same vacuum chamber and applied at the same time. However, PIXE and RBS are the most frequently used ion beam analytical techniques. Therefore this TECDOC is focused on the instrumentation for RBS and PIXE only.

Sections 1 and 2 give some basic information about accelerators needed for RBS and/or PIXE applications. There are basically three types of accelerators in the energy region of interest for analytical applications. These are: electrostatic accelerators, linear accelerators (particularly radio-frequency quadrupole accelerators) and cyclotrons. The most widely used of these are the electrostatic accelerators.

Sections 3 and 4 give an overview of instrumentation for PIXE and RBS. In Section 3, the majority of the problems connected with instrumentation for nuclear analysis have been reviewed from the point of view of PIXE. RBS can be performed using an instrumentation coinciding to a large extent with that of PIXE. For example, the accelerator, the target chamber, the target holder and a large part of the nuclear electronics might be the same. Most of the conclusions presented in this section also hold for RBS. In Section 4, the range of problems has been presented with special emphasis on RBS related points.

2. ACCELERATORS FOR MATERIAL CHARACTERISATION

The most common type of accelerators used for the application of ion beam analysis techniques, from their early development until today, are the electrostatic accelerators. The most widespread ion beam analysis techniques, PIXE and RBS, define most of requirements on the accelerator. Protons and alpha databases in the energy range 1–3 MeV are the most frequently needed ions. Broader range of energies (both lower and higher) and ions (heavier ions) will in principle enable a wider range of analytical possibilities. Beam currents of less than 1 μA (easily delivered by the typical electrostatic accelerator) are sufficient for all existing characterisation techniques.

Electrostatic accelerators are operated today in basically the same way as their prototypes constructed at the beginning of thirties. The most successful of these were Cockcroft-Walton and van de Graaff accelerators.

In 1932 J. Cockcroft and E. Walton built at Cambridge the accelerator based on voltage multiplication which was able to accelerate protons to 380 keV energy. Cockcroft-Walton accelerators were used for decades mostly as neutron generators (using (d,n) reactions), until the recent revival of the similar principle found in new MeV tandem accelerators built without moving parts (HVEC singletron and tandetron) [1].

Producing a 1 MV potential difference between the terminals of two belt charged generators, R.J. van de Graaff demonstrated in Princeton in 1931 a principle of the most known electrostatic accelerator — the Van de Graaff. Since then a large number of MeV accelerators using the Van de Graaff generators were built enabling numerous experiments in the field of nuclear structure research.

The main part of the Van de Graaff accelerator is the high voltage generator. It consists of a continuous conveyor belt that carries electrostatic charges (sprayed by the DC power supply) up to a hollow terminal. The high DC potential is maintained by a charge continuously flowing back to the ground through a voltage divider of very high resistance. A beam of positive ions is extracted from the chamber with a RF oscillator ionised gas inside the terminal (a positive ion source). The positive ions are then accelerated through the accelerator tube to the ground potential. Such single-ended accelerators are used for the production of protons and αdatabases between a few hundred keV and a few MeV energy. Positive ions can be produced from any atom of the periodic table with many available ion sources. However, a difficult access to the ion source that needs a power at a potential of some million volts limits the range of ions that can be conveniently produced. A review by Alton [2] describes the principles of existing positive and negative ion sources.

More versatile Van de Graaff accelerators are tandems, having a negative ion source outside the accelerator and a two stage acceleration with a pair of accelerator tubes. A stripper channel inside the high voltage terminal is used to strip the electrons from the accelerated beam of negative ions. Either a thin carbon foil (2–5 $\mu g/cm^2$), or a low pressure gas in a narrow channel is used as a stripper. Already accelerated ions are accelerated again over the same potential difference. The total energy which ions acquire is (n + 1)V, where n is the charge state of the ion emerging from the stripper at the terminal voltage V.

Larger range of energies and most of the ion species can be produced in tandem accelerators. Voltages as high as 20 MV could be achieved in tandems. However, tandems that accelerate ions in the low MeV energy range are today the most common, due to the frequent application of ion beams to materials characterisation. Instead of the conventional belt, many of the new accelerators today have a chain of insulating and metallic links (NEC pelletrons) [3].

Electrostatic accelerators are mounted inside a pressure vessel (tank) that contains the high pressure insulating gas. Perhaps the best gas for this purpose is sulphur hexafluoride (SF_6), but various mixtures of N_2 and CO_2 are also used.

Ions emerging from the accelerator pass through the analysing magnet, used for the selection of particular energy and ion having the same magnetic rigidity:

$$Br=(2mE/q^2)^{1/2} \quad (1)$$

where, B is magnetic induction, mE particle mass and energy, q its charge and r radius of curvature. After the analysing magnet, the beam passes through the switching magnet, which directs the beam to the appropriate beam line. Magnetic and/or electrostatic focussing (quadrupoles) and steering (deflectors) are needed to direct the beam towards the experimental target chamber.

More about the fundamentals of charged particle acceleration and beam transport can be found in numerous books and reviews. In particular book by Humphries [4] and the review of the history of electrostatic acceleration by Bromley [5] are suggested.

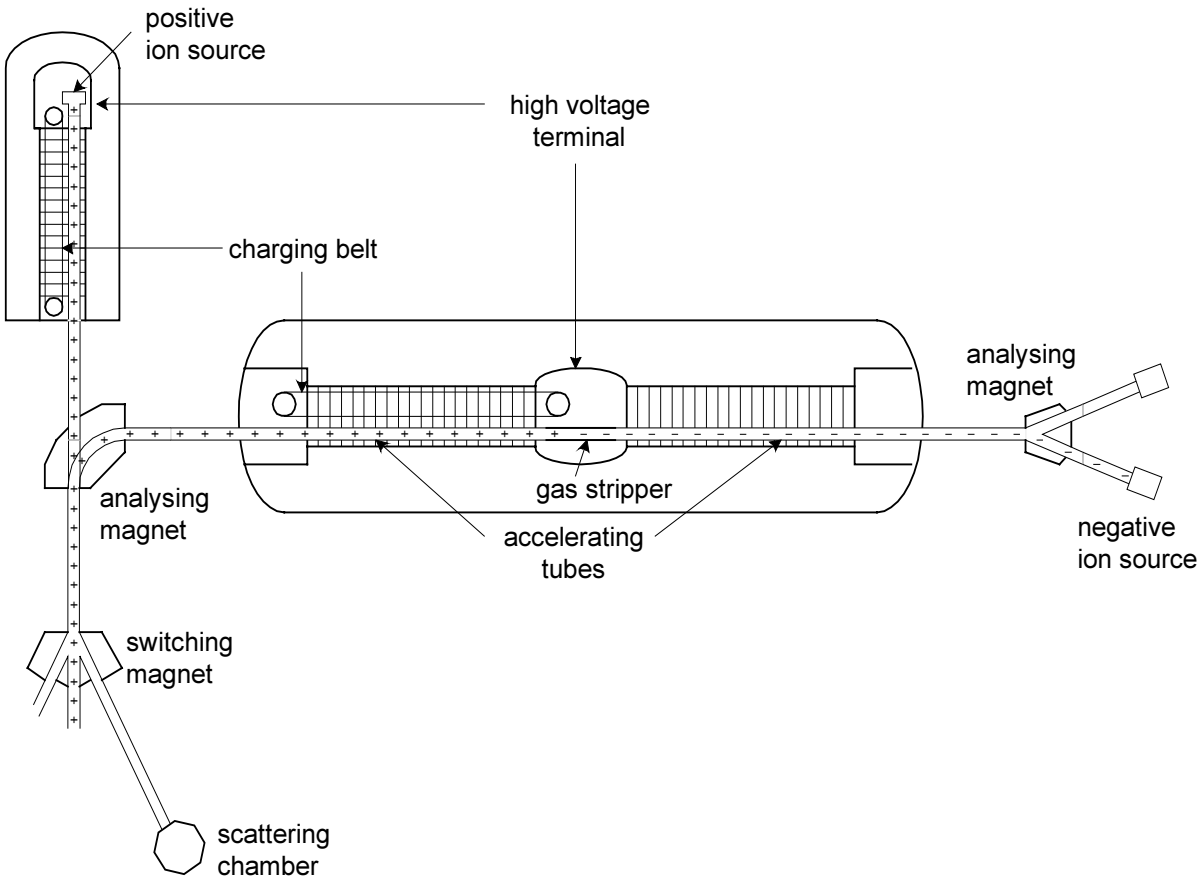

FIG. 1. Schematic drawing of electrostatic single ended and tandem accelerators usually used for ion beam analysis. The drawing serves to illustrate possibilities to use single stage (top left) or tandem (central part of the figure) accelerator.

3. INSTRUMENTATION FOR PIXE

3.1. INTRODUCTION TO PIXE

In 1970 Johansson et al. [6] presented PIXE as a novel and powerful analytical method. Characteristic X rays produced in sample being irradiated by MeV protons, were for the first time detected by semiconductor Si(Li) X ray detector that had just become available. This analytical method soon became widely accepted in different accelerator laboratories, known under the acronym PIXE — particle induced X ray emission spectroscopy.

There are four main physical processes of importance to PIXE: (i) when a charged particle (proton or heavier ion) enters the material it encounters numerous inelastic collisions by sample atoms; (ii) the energy of the ion along its trajectory decreases according to the specific energy loss (stopping power); (iii) from some of the numerous ionised atoms along the particle path, characteristic X rays are emitted with a probability given by the X ray production cross section; (iv) finally, X rays emerging from the sample are attenuated in the material.

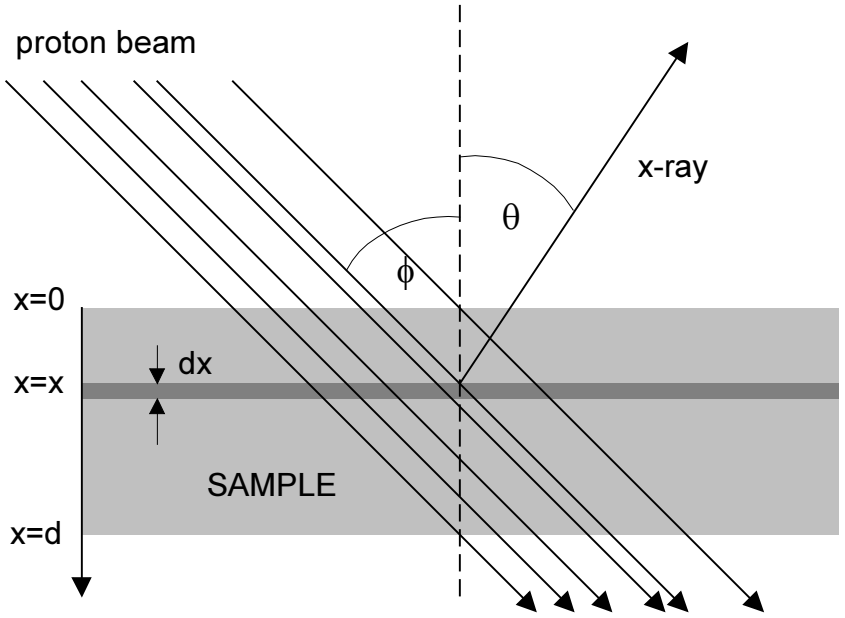

FIG. 2. Schematic presentation of the PIXE experiment for sample with finite thickness d.

In addition to X ray production probability, the composition of the target has influence on particle energy loss and X ray attenuation as well. In a general case of PIXE analysis as given in Fig. 2 the X ray yield Y_i for the characteristic X ray of the i-th element in the sample towards the direction of the detector will be:

$$Y_i = \frac{Q}{e}\int_0^d c(x)\sigma_i(E(x))e^{-\mu x/\cos\theta}\,dx \qquad (2)$$

The incoming particles lose their energy while passing through the sample according to:

$$E(x) = \int_0^x S(E)\, dx' \quad \text{where } S(E) = \frac{dE}{dx'} \tag{3}$$

If the concentration profile of the i-th element c(x) is constant, while the X ray detector has efficiency ε, the relationship between the observed X ray intensity and element concentration is given by:

$$I_i = Q\, C_i\, K_i \tag{4}$$

The calibration constant K_i is independent of the sample if both geometry of the experiment and sample matrix composition do not change.

$$K_i = \varepsilon \int_0^d \sigma_i(E(x)) e^{-\mu x/\cos\theta}\, dx \tag{5}$$

It is clear from Eqs (4) and (5) that for the reliable PIXE analysis several conditions have to be fulfilled. Successful analysis can be performed on well-characterised sample (flat surface, known thickness and matrix composition), and fully controlled experimental conditions (in case of thin samples, analysis is much simplified). For the quantification procedure, one can either use the fundamental parameter approach (by calculation of K_i from X ray production cross sections σ_I, particle stopping power S(E) and X ray attenuation μ) or comparison of unknown sample with standards (calibration constants K_i are experimentally determined). The most important uncertainties among parameters of the experimental set-up that will influence accuracy and precision of PIXE as analytical technique are the following:

- particle energy (E_0),
- total exposure of sample by incoming particle beam (Q),
- geometry (θ,ϕ),
- detection efficiency (ε),
- matrix composition,
- statistical uncertainty in the determination of peak area I_i .

In the context of instrumentation for PIXE these will be discussed in following sections in more details. More about other aspects of quantitative PIXE analysis can be found in various books and articles. Strongly suggested is the comprehensive book by Johansson, Campbell and Malmquist [7]. Several articles about this subject [8,9] and PIXE Conference Series Proceedings published in the international journal *Nuclear Instruments and Methods in Physics Research* are suggested as well [10].

3.2. TARGET CHAMBERS AND ASSOCIATED EQUIPMENT

Target chambers are designed for the performance of experiments using charge particle beams. Their characteristics will depend on the requirements determined by the technique for which the chamber is needed. There are numerous desired characteristics of the Target chamber for the PIXE measurement. These are in practice not always achievable due to the particularly available experimental space, available parts (such as pumps, valves, detectors), or restrictions imposed by the samples to be analysed. However, independently of any restrictions, certain rules have to be followed. The beam of ions (usually protons) should be uniform and collimated, the X ray detector (usually Si(Li) detector) has to be positioned to view the characteristic X rays emitted from the surface of the sample. The chamber has to be easily re-evacuated and hold sufficiently good vacuum, while all the geometrical parameters (distances and angles between the beam, sample and detector) have to be reproducible (Fig. 3).

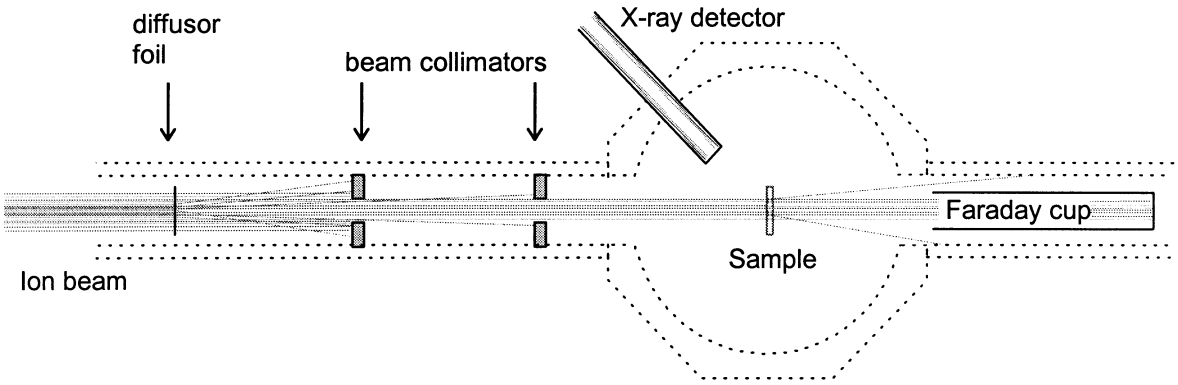

FIG. 3. The essential parts of the PIXE set-up.

If the PIXE quantification procedure is based on the standardless or fundamental parameter approach (which is today mostly the case), reliable measurement of the total charge that emerged to the target is also one of the essential chamber functions. Depending on the type of the detection system, filter transmission and detector efficiency should be known together with characteristics of the sample itself (area, matrix composition, thickness and surface morphology). More about functions that the chamber needs to fulfil will be discussed in the following sections of this section. General considerations about the X ray detection and its efficiency will be given in Section 3.3.

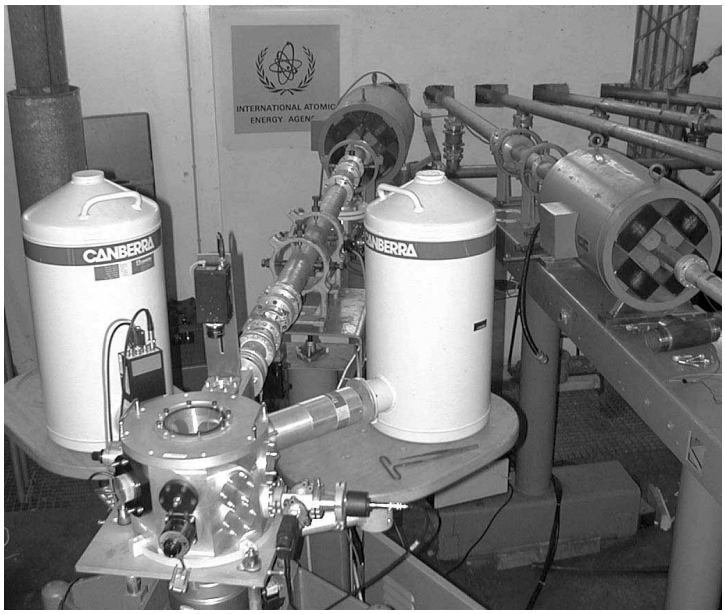

FIG. 4. IAEA PIXE beam line at the Ruder Boskovic Institute, Zagreb, Croatia.

3.2.1. Vacuum systems

The beam of high-energy ions is transported to the target chamber along a drift tube that is maintained at high vacuum. A vacuum between 10^{-3} to 10^{-4} Pa pressures will be sufficient for the minimum collision probability between the fast ions and residual gas molecules. The energy loss of fast ions in such a high vacuum will be negligible (less then 1 eV per 1 m of drift length for the most of the light MeV ions) as presented in Table I. The energy loss for protons will be negligible even at pressures one or two orders of magnitude higher (10^{-1} to 10^{-2} Pa). The only factor that needs to be

considered at such a medium vacuum is the increase of a beam Target with a residual gas. Scattering increases the beam halo and disturbs the shape of the beam profile which can increase the intensity of background peaks in PIXE spectrum.

TABLE I. RANGE IN AIR AND ENERGY LOSS FOR DIFFERENT ION SPECIES AND ENERGIES. ENERGY LOSS VALUES ARE THE SAME IF GIVEN FOR AIR (IN KeV/μm), OR VACUUM WITH PRESSURE 10^{-4} Pa (eV/m)

Ion/energy	Range in air (mm)	ΔE (keV/μm) in air, or ΔE (eV/m) in vacuum 10^{-4} Pa
p, 1 MeV	23.25	0.0273
p, 2 MeV	71.25	0.0169
p, 3 MeV	140.52	0.0126
α, 1 MeV	5.21	0.232
α, 2 MeV	10.24	0.107
^{12}C, 3 MeV	5.21	0.868
^{28}Si, 6 MeV	6.27	1.860

The drift tubes (beam lines) and the chamber are preferably made of materials having low outgassing rate and low vapour pressures. Materials that become part of the vacuum system must have also sufficient mechanical strength to withstand the pressure difference. Stainless steel, glass windows and metal seals are in all respects the best solutions having the lowest outgassing rates. Aluminium chambers with Perspex windows and rubber seals are also frequently used due to much easier machining, but these are not recommended for the ultra high vacuum.

Vacuum stations attached to the target chamber or to the drift tubes are consisting of the high vacuum pump and the fore pump, since no single pump has yet been developed which is able to pump down from atmospheric pressure to the high vacuum range. The selection of pumping principle for the particular application is defined by the main parameters: the lowest pressure, the pressure range, the pumping speed and the exhaust pressure.

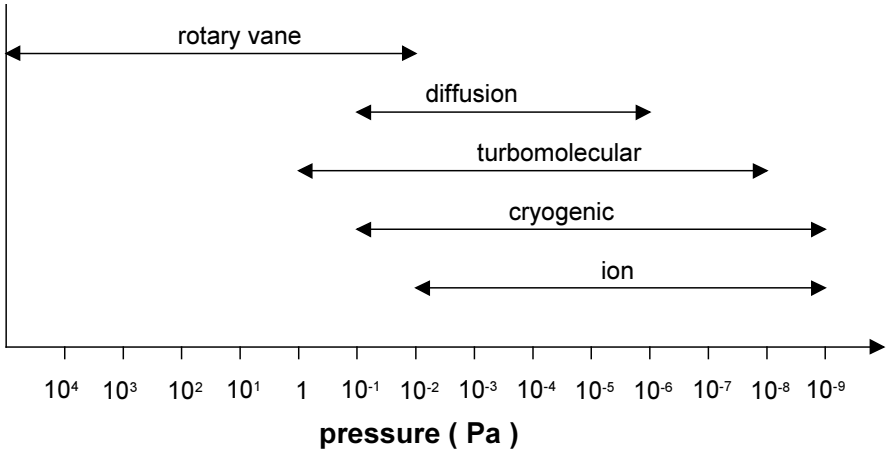

FIG. 5. Approximate pressure ranges of various vacuum pumps.

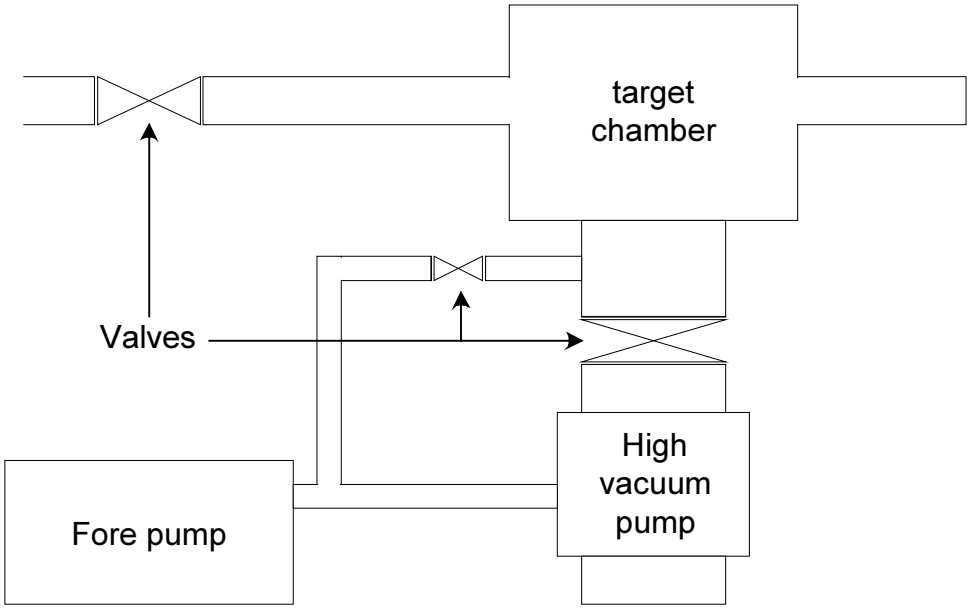

FIG. 6. Schematic presentation of a typical vacuum system.

In Fig. 5 pressure ranges of the typical vacuum pumps are given. In order to obtain the lowest pressure in the range 10^{-3} to 10^{-4} Pa, use of the mechanical pump for the initial (roughing) and exhaust (backing) pumping is the most convenient, while diffusion, turbomolecular, ion and cryogenic pump can be used for reaching the final pressure. Pumps that eventually exhaust gases to the atmosphere (diffusion and turbomolecular) require a backing pump, while pumps that immobilise the gases within the system (cryogenic and ion pumps) require no outlet.

The most common, mechanical rotary-vane fore-pump is used initially to reduce the pressure in the pumping volume until the high vacuum pump can take over. It also removes the exhaust from the high vacuum pump. In a mechanical rotary-vane pump compression-expansion of the gas is used as a pumping principle. A large volume of the incoming low pressure air is compressed by a continuos reduction and exhausted to the atmosphere.

In the past the most frequently used high vacuum pumps were the oil diffusion pumps. In spite of their high power consumption and need for a cold trap that eliminates oil vapours, diffusion pumps are easily maintained and reliable. It is important to be aware of a thin oil layer, which is gradually deposited at the all surfaces inside the chamber (including the sample and detector surface) during the pumping process.

Turbomolecular pumps are the most widely used high vacuum pumps today in MeV ion accelerator applications. Easy to operate, they enable fast start, which can be of interest for the use at the target chamber. However, vibrations of the mechanical bearing pumps may affect the semiconductor detector energy resolution.

Cryogenic and ion pumps are the gas immobilisation pumps used especially when lower final pressure (ultra-high vacuum) is required. More about the principles of operation of all vacuum pumps as well as about the fundamentals of vacuum technology can be found in books such as one written by Roth [11].

A typical layout of the vacuum system that is used for pumping the target chamber is shown in Fig. 6. Valves are arranged between the different sections of the beam tubes and target chambers, in a way to isolate different parts of the system from the vacuum pumps.

3.2.2. Collimators and diffusers, chamber materials

The cross section (profile) of the ion beam entering the chamber has ideally the Gaussian distribution. To prepare the beam for the sample analysis, it needs to have the uniform distribution along the appropriately shaped cross section.

The shape of the beam cross section is defined by a series of collimators. They are typically circular holes of diameter ranging from less than mm (milliprobes), up to 1 cm, but most often between 3 and 8 mm. Collimators can also consist of two series of x and y slits that can limit the beam to different rectangular shapes.

In any case, a minimum of two series of collimators is needed (Fig. 7). The first collimator or collimators define the beam shape, while the last one is the antiscattering collimator. The antiscattering collimator reduces the beam that is scattered on the edges of the beam defining collimator. Without it, the scattered part of the beam can excite X rays of the elements in a sample frame, chamber and other parts that can be "seen" by the X ray detector.

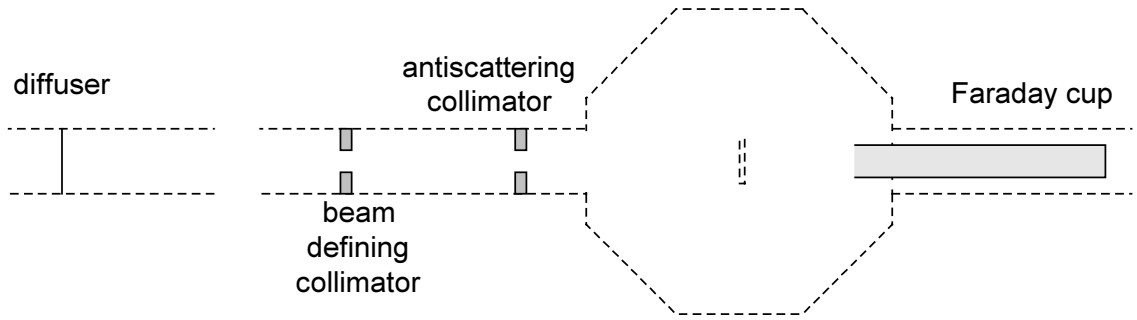

FIG. 7. Diffuser and collimators.

Uniform distribution of the beam across the cross section defined by a collimator is achieved generally in two ways: (i) by intentionally diffusing the beam before it enters the collimator, or (ii) by scanning the focused beam across the particular region of the sample. In the first procedure, a large portion of the beam current will be lost, while in the focused and scanned beam all current will be used.

Using the beam transport system lenses, the beam can be defocused before it enters the collimators system. Quartz (retractable) viewing of the beam shape or beam profile monitor just before the collimators can be essential to inspect the beam homogeneity.

If the diffuser foil is selected a rigid material having high thermal and electric conductivity material has to be used. The most convenient elements for that purpose are Al, Cu, Ag and Au. Based on the Mayer [12] theory of multiple scattering, Montenegro et al. [13] found a relationship that can be used to compute the uncertainty in the beam uniformity ε_f across the collimator diameter. The uncertainty in the beam uniformity as the function of diffuser thickness has the shape of *tanh* function. In Fig. 8, an uncertainty in the beam uniformity is given for a 3 MeV protons and a gold diffuser in two different geometrical configurations. For the values of uncertainty in the beam uniformity between 5% and 10%, between 10% and 20% of the total beam current pass through the collimator. The fact that the initial energy of the beam ions is changed due to the energy loss has to be also taken into account.

Appropriate shape of the sample irradiation can also be achieved by using the nuclear microprobe system. In nuclear microprobe the ion beam is focused by a series of magnetic quadrupoles (doublet, triplet or quadruplet) to a micron spot-size [14, 76–82]. A focused beam is

scanned over the sample surface using the scanning system (magnetic or electrostatic deflection). With a sufficiently high scanning frequency, a uniform irradiation can be achieved. In addition, scanner can be controlled in such a way to produce different shapes of irradiation, which are determined on the basis of particular analytical problem (Fig. 9). Although nuclear microprobe PIXE will not be further discussed here, the basic idea of scanning the beam uniformly over the surface of some particular shape can be used successfully even with conventional focusing capabilities available at many accelerators.

TABLE II. THICK TARGET γ RAY YIELDS FOR SOME PURE LIGHT ELEMENTS, AS GIVEN BY ANTTILA ET AL. [16] AND KISS ET AL. [17]. ONLY γ RAYS WITH YIELD HIGHER THAN 10^6 COUNTS/μC Sr AND 1.7, 2.4 AND 3.1 MeV PROTON ENERGY ARE GIVEN

Element	E γ (keV)	γ ray yield (x 10^6 counts/μC Sr)			Reaction
		1.7 MeV	2.4 MeV	3.1 MeV	
Li	429	-	-	9.2	$^{7}Li(p,n_1\gamma)^{7}Be$
	478	8.6	26.0	56.0	$^{7}Li(p,p_1\gamma)^{7}Li$
Be	3562	-	0.02	2.5	$^{9}Be(p,\alpha_1\gamma)^{6}Be$
B	429	0.9	3.5	7.2	$^{10}B(p,\alpha_1\gamma)^{7}Be$
	718	-	0.12	1.3	$^{10}B(p,p_1\gamma)^{10}B$
	2125	-	-	4.8	$^{11}B(p,p_1\gamma)^{11}B$
F	110	0.1	7.2	11.0	$^{19}F(p,p_1\gamma)^{19}F$
	197	0.2	20.0	37.0	$^{19}F(p,p_2\gamma)^{19}F$
	1236	-	3.0	5.4	$^{19}F(p,p\gamma_{3\text{-}1})^{19}F$
	1349	-	1.3	2.1	$^{19}F(p,p\gamma_{4\text{–}1})^{19}F$
	1357	-	1.4	4.2	$^{19}F(p,p\gamma_{5\text{–}2})^{19}F$
	1459	-	0.9	3.9	$^{19}F(p,p_4\gamma)^{19}F$
	6129	2.6	67.0	95.0	$^{19}F(p,\alpha_2\gamma)^{16}O$
Na	440	0.8	9.6	16.0	$^{23}Na(p,p_1\gamma)^{23}Na$
	1634	0.2	9.9	19.0	$^{23}Na(p,\alpha_1\gamma)^{20}Ne$
Mg	1369	0.1	0.9	5.1	$^{24}Mg(p,p_1\gamma)^{24}Mg$
Al	844	-	0.1	2.3	$^{27}Al(p,p_1\gamma)^{27}Al$
	1014	-	0.3	4.6	$^{27}Al(p,p_2\gamma)^{27}Al$
Si	1779	-	-	1.2	$^{28}Si(p,p_1\gamma)^{28}Si$
P	1266	-	1.6	5.2	$^{31}P(p,p_1\gamma)^{31}P$
Cl	1219	-	0.2	1.5	$^{35}Cl(p,p_1\gamma)^{35}Cl$

Any interaction of the incoming beam ions with a surrounding material, can be the source of X ray or γ ray background. Background X rays can originate directly from collimators and Faraday cup (if detector can "see" the last antiscattering collimator or Faraday cup). If the beam is not well collimated, particles from the beam halo can excite X rays in sample frame or chamber walls. In order to check for the presence of background X ray peaks, a PIXE spectrum of an empty frame should be

recorded (see Fig. 12). Any background peaks should be eliminated by appropriate changes in geometry, either by X ray detector collimation, or by covering the exposed chamber parts by materials that do not emit detectable X rays.

Contrary to the background X rays, which are directly visible in PIXE spectrum, γ rays emitted in the chamber environment are more difficult to detect. Compton scattering of γ rays in the X ray detector increases the continuum background of PIXE spectrum. If this background is too high, a lead shield has to be positioned between the source of γ rays and detector. Elements with the highest γ ray yields are given in Table II. The typical source of γ ray background is aluminium tubing in the collimation system. High γ ray background can be expected also if the samples with high amount of listed elements are analysed by PIXE. Due to the high cross section for (p, pγ) and (p, αγ) nuclear reactions, fluorine is the element with the highest γ ray yield. This is the reason why Teflon backings are not the best option for PIXE.

If samples with high γ ray yield are analysed frequently, an anti Compton shield might reduce the unwanted background. An appropriately shaped plastic scintillator surrounds the X ray detector and detects a photon scattered inside of X ray detector by a Compton scattering. An anticoincidence setup rejects some of the background pulses, produced by an electron. Anticoincidence shields are more frequent in γ ray spectroscopy, but some are used in PIXE as well [15].

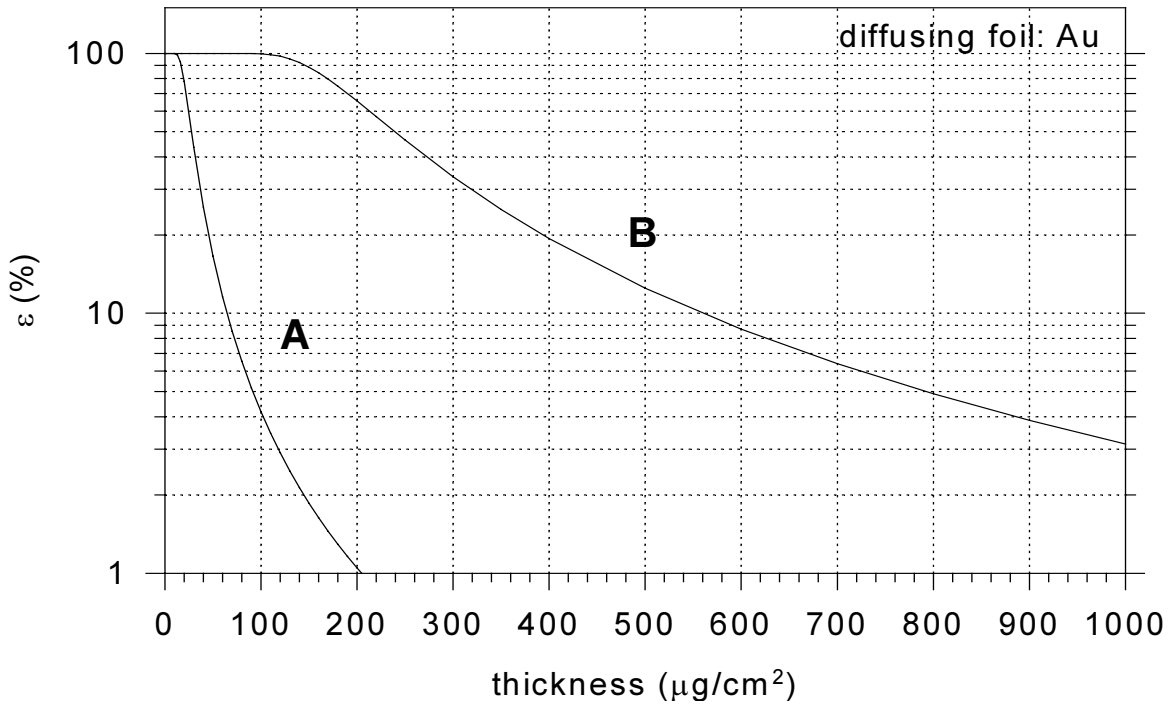

FIG. 8. Variation of the uncertainty in the uniformity of the 3 MeV proton beam after passing different thickness of an Au diffuser for two different geometries. A — 110 cm diffuser to collimator distance, collimator 2 mm and B — 30 cm diffuser to collimator distance.

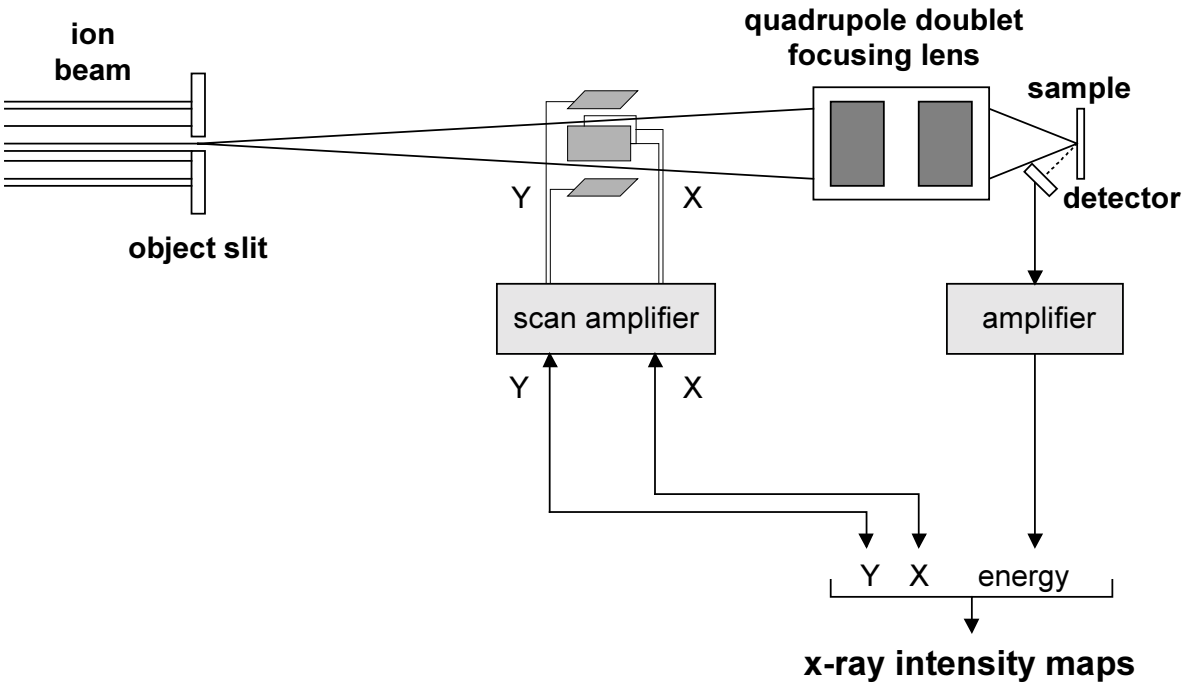

FIG. 9. Schematic presentation of the beam scanning and focusing in the nuclear microprobe set-up. Depending on the construction of the system, magnetic coils or electrostatic deflectors can be positioned either in front of, or after the focusing lenses.

3.2.3. External beam

For samples that cannot be introduced in vacuum, introduction of air into the target chamber has to be used (e.g. liquid samples). However, the range of the protons and attenuation of the X rays in air may be a limitation. Therefore, the helium atmosphere having more than 10 times lower energy loss is often used instead of air (Table II). In addition, X ray absorption in helium is also lower while its thermal conductivity is higher than in air.

For samples that can on no account be situated in the target chamber (e.g. art and archaeological objects), or when air is intentionally left in the chamber, the beam of ions has to be transmitted through the exit foil to the air. It is evident that protons will be the most suitable for such a purpose, due to their lowest energy loss. The exit foil needs to be made of light material (low energy loss, straggling and bremsstrahlung, no X rays), with low probability for nuclear reactions induced by the beam. The foil has to be vacuum tight for as much as possible of beam time. It is good also to have the high thermal conductivity. Williams reviewed available materials for the exit foil [18]. The most common of these are listed in Table III. In the review given by Menu [19], Kapton foil was presented as the most widely used exit foil material. However, development of ultra thin foils (important for external microbeam applications), such as Si_3N_4 foil used on AGLAE facility of the Louvre museum [20], is introducing many other possibilities for the future external beam experiments.

Simultaneous PIXE and RBS in air is not possible. However, the total charge that emerged on the target can be easily estimated by introduction of RBS detector that detects backscattered protons from the exit foil or from the air between the exit foil and target. If the exit foil is made of aluminium, (p, γ) reactions on ^{27}Al can be used as beam current monitor with Ge detector placed in the vicinity of the exit foil (with Al exit foil, increased background can be expected in PIXE spectra). Total charge can be measured from the target as well but with a less reliable measurement. There is also a possibility to measure the total charge employing the light emitted by the fluorescence in air.

As is seen from the Fig. 10, in PIXE setup with external beam, distance between the exit foil and the sample has to be small to minimise the energy loss of the beam. To detect low energy part of the PIXE spectrum, the X ray detector has to be close to the sample as well. That is why the most of the existing arrangements have a nozzle with its top carrying the exit foil. This enables close positioning of any object as a sample. If the energy loss and X ray absorption is still too high, a helium atmosphere around the set-up can improve the detection efficiency.

Higher background in PIXE spectrum is observed due to the bremsstrahlung and gamma radiation emitted along the beam path (exit foil and air). However, performance of the external beam PIXE in terms of detection limits, can be still close to the conventional PIXE in vacuum. This is possible by increasing the beam current, since samples in air are cooled much easier. Specimen damage by such high currents can be further minimised by cooling the specimen with a stream of a cooled gas. The same method should be used for the cooling of the exit foil.

Various solutions for PIXE analysis of bulk materials using the external beam are discussed by Demortier [21].

TABLE III. SOME CHARACTERISTICS OF AIR, HELIUM AND EXIT FOIL MATERIALS

Material	Density (g/cm^3)	dE/dx, (3 MeV protons)	Range (mm)	Thermal conductivity [Ref. 22] (W/m K)
air	0.00125	12.60 keV/mm	139	0.026
He	0.00017	2.21 keV/mm	767	0.156
Be	1.85	18.54 keV/μm	0.095	200
C (graphite)	2.25	24.20 keV/μm	0.073	5.7 (⊥), 1950(II)
C (diamond)	3.50	37.53 keV/μm	0.047	895–2300
kapton	1.43	15.81 keV/μm	0.110	–(0.1–0.3 nylon)
Al	2.70	22.42 keV/μm	0.081	237
Au	19.31	72.17 keV/μm	0.026	317

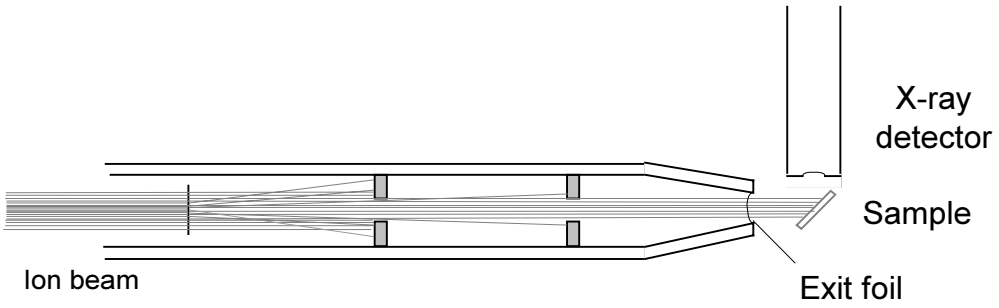

FIG. 10. PIXE setup with external beam [23].

3.2.4. Charge measurement

In the most of the PIXE quantification procedures, the exact knowledge of the total charge that arrived at the sample is essential. The accuracy of the charge measurement can often be the weakest point of the PIXE quantification procedure using fundamental parameter approach. If no internal standard is added to the sample or no any other normalisation procedure is possible, one of the two ways of charge measurement has to be performed. The first way is the direct measurement using the charge integrator connected to the Faraday cup (and the sample). The second possibility is the indirect charge measurement using some other process that is charge dependent.

The direct measurement of the total charge delivered to a sample can be done by connecting electrically the sample holder (insulated from the chamber) and the Faraday cup to the charge integrator. If the sample is thin enough the beam transmitted through the sample will be stopped in the beam stop (Faraday cup). For the thick specimens, the charge will be collected directly from the sample holder. The beam stop is often lined with a graphite, to prevent high energy gamma or X ray emission that can increase the PIXE background if other materials such as aluminium are used.

Unfortunately, secondary electrons that escape from the sample can cause an overestimation of the total charge. This can be solved if secondary electron suppression electrode(s) is added in front of or around the sample holder and the Faraday cup. A negative potential of few tens or hundreds of Volts on suppression electrodes (see Fig. 11) will prevent electrons from escaping the sample holder/Faraday cup. It is also possible to isolate the whole PIXE chamber, which will then act as the single Faraday cup. Such a set-up can suffer from electrical interference due to the capacitive pick-up. Probably the most efficient way of electron suppression can be achieved by similar principle if Faraday cup and sample holder are polarised by positive potential. This can be performed by battery (~100 V) connected in series between the Faraday cup and charge digitizer. Cables having high resistance insulation have to be used. If the Faraday cup is used for the measurement of ions heavier than protons, the net charge will depend on the charge state of the ion selected at the analysing magnet. However, bad vacuum in beam lines downstream of the magnet can cause beamline charge exchange and change of the average charge state.

There are numerous ways of indirect charge measurement. This is usually done in between the last collimator and the sample. Current can be measured directly from the rotating vane that intercepts the beam certain percentage of the total time. If the beam variations are not excessive, instabilities of the beam can be averaged out.

A counting of ions backscattered from the foil placed in the same position, or from the foil at the surface of the rotating vane is another alternative way of indirect charge measurement. Careful and frequent calibration of such systems is necessary, since the life times of thin foils can be limited. Whatever kind of indirect charge measurement is chosen, care has to be taken to prevent the X rays emitted in the foil from reaching the X ray detector. This is essential for the PIXE measurements of thin specimens when higher beam currents, and larger solid angles of detector are needed.

For the purpose of PIXE analysis, a quite useful method of charge measurement can be performed using the simultaneous RBS analysis. Simulation of RBS spectrum for any kind of sample can be successfully made on well-calibrated RBS experimental set-up. As suggested by Grime [24], the total accumulated charge of the particular experiment and the sample matrix composition are results for such simulation.

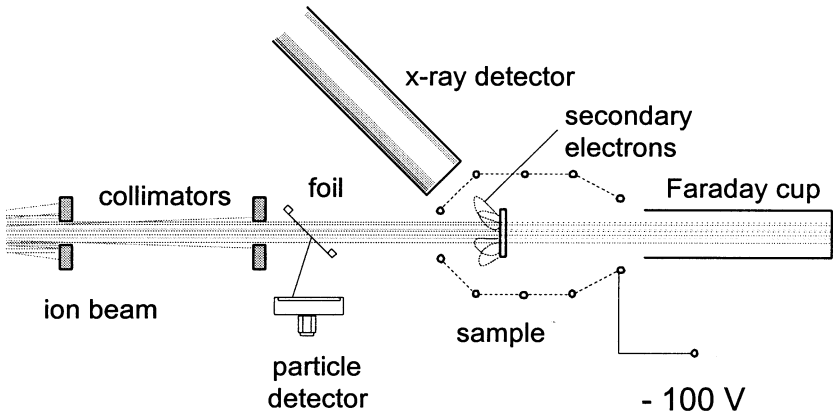

FIG. 11. Schematic presentation of direct and indirect charge measurement.

In some particular analytical cases, the charge measurement is not needed. For example, addition of internal standard or knowledge of exact concentration for any element visible in PIXE spectrum with sufficient statistics will give the important normalisation factor. In the case of some alloys, X rays of all elements will be visible, allowing the normalisation of all elements to 100%. For some minerals, oxide normalisation is also possible.

3.2.5. Sample changers and target holders

Reaching the state of maturity, the PIXE spectroscopy became a routine analytical method for the analysis of large number of samples. It is therefore essential for the PIXE set-up, to be equipped with automated target changer. Signal needed to trigger the target changer to step onto the next sample is usually send by a data acquisition computer allowing fully automatic analysis.

The sample holder itself (especially if the targets are thick) needs to be conductive and electrically connected to the earth, directly or through the charge integrator. To keep the geometry constant, the sample surface that will be exposed to the beam has to be always in the same plane. Errors caused by the changes in geometry can be quite significant. Some of the typical geometrical imperfections that can be attributed to the inappropriate sample positioning and corresponding errors in quantitative analysis are listed in Table IV. It is visible that higher uncertainty can be expected for light elements (low energy X rays) and samples with heavier matrix composition.

Construction of the sample holder depends mainly on the typical samples that are analysed. At the moment there is no standard sample holder shape, but each PIXE laboratory has its own approach. Still, care is needed when the size of the beam cross section is close to the size of the frame. Inappropriate collimation can allow beam scattered from the slits to hit the sample frame and thus produce unwanted background peaks in the spectrum (see Fig.12. for example) as discussed in Section 3.2.2.

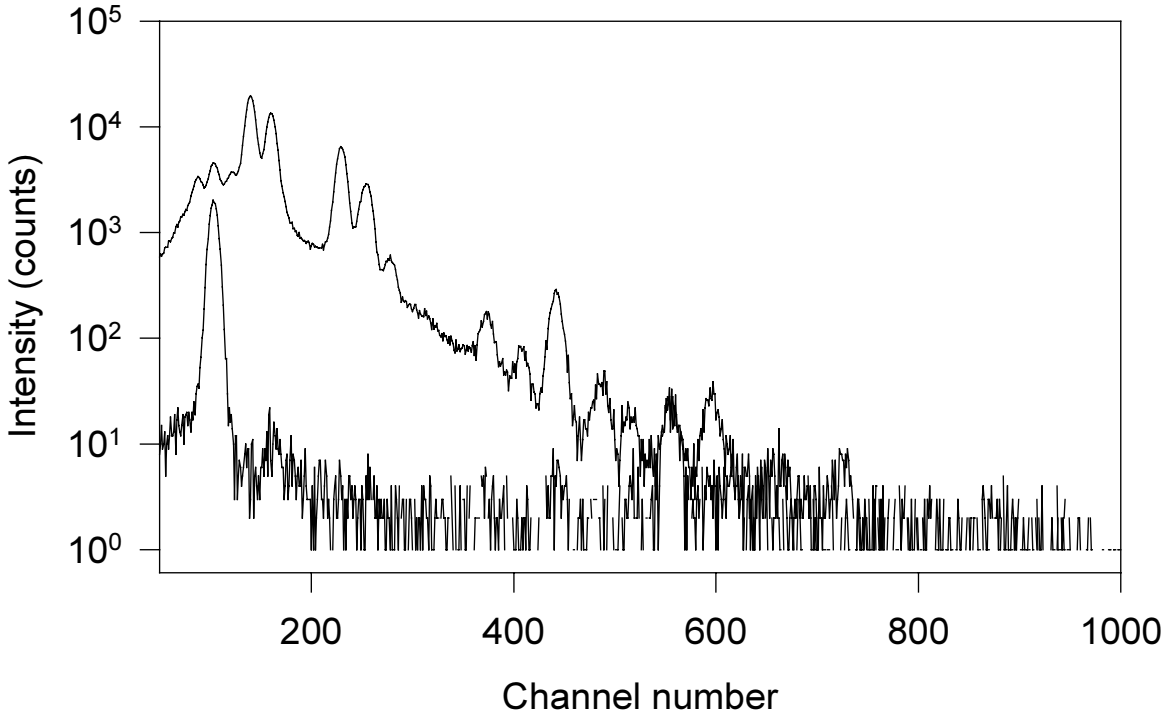

FIG. 12. PIXE spectrum of the thin sample of candidate reference material IAEA 393 Algae on a nucleopore filter (A) and empty Al frame (B), with the same collected charge. Background peaks (aluminium, iron and copper) visible in spectrum B are indicating inappropriate beam collimation.

In some cases (aerosol sampling with time increments), subsequent analysis of many positions along the sample is required. An automated translator or rotator controlled by a data acquisition computer needs to be used for this purpose. More flexible sample movement is achievable with an external beam set-up. As described by Boisseau [25], it is possible to construct a computer controlled sample scanning system.

For some specific applications of PIXE in materials research a goniometer stage is used for the sample positioning. These are PIXE channelling, TPIXE (total reflection PIXE) [26] and grazing angle incidence PIXE.

In order to perform exact positioning of the sample in respect to the beam, the target chamber can be equipped with a CCD camera that permits viewing the sample surface. If the quartz is positioned instead of the sample, the position of the beam spot can be viewed directly.

TABLE IV. CHANGES IN THE Si, Ca AND Fe K X RAY INTENSITIES IN TWO DIFFERENT MATRICES (C AND Si) AND 3 MeV PROTONS FOR 1^{o} CHANGE IN SAMPLE TILT, OR 1 mm CHANGE IN SAMPLE TO DETECTOR DISTANCE (D)

	$\alpha = \theta = 45^{o}$	$\alpha = 0^{o}, \theta = 45^{o}$	$\alpha = \theta = 22.5^{o}$	D =100 mm	D = 50 mm
	1^{o} tilt C/Si matrix	1^{o} tilt C/Si matrix	1^{o} tilt C/Si matrix	1 mm change in d	1mm change in d
Si (Kα)	3.4%/3.3%	1.7%/1.7%	1.4%/1.4%	2.0%	4.0%
Ca (Kα)	0.9%/3.3%	0.6%/1.6%	0.4%/1.4%	2.0%	4.0%
Fe (Kα)	0.1%/1.9%	0.1%/1.1%	0.1%/0.8%	2.0%	4.0%

3.2.6. Geometrical arrangement

The ion beam energy loss, the X ray attenuation and the bremsstrahlung emission by secondary electrons are physical processes that will be strongly affected by the geometrical arrangement of the main components in the PIXE target chamber.

The largest analysed depth can be obtained if the incoming beam direction is orthogonal to the sample surface and if the X ray detector views the sample in the same orthogonal direction. In such an arrangement, the influence of the surface imperfections is the smallest. Unfortunately, this is practically impossible since the X ray detector is housed in a cryostat attached to a large dewar. Therefore the most commonly used angle of the detector is 135^{o}.

Such an arrangement is also favourable since the lowest contribution of the secondary electron bremsstrahlung radiation is in angles far from the 90^{o} angle [27]. In case of very low count rates it may be important to maximise the detector solid angle, and if the used detector (cap) has a large diameter, it might be better to place the detector at 90^{o}.

The arrangement shown in Figs 3 and 4 is suitable for the introduction of the second PIXE detector at -135^{o} angle. Some PIXE laboratories are using such an arrangement with two detectors. The large solid angle X ray detector has a filter that transmits only higher energy X rays (K X ray lines of heavier elements, having much lower X ray production cross sections than low Z elements). The second detector, without a filter, further away from the sample, is dedicated to the detection of characteristic X rays of low Z elements (Fig. 13). If this detector has an ultra thin detector window, magnetic deflection of backscattered protons that can be transmitted into the detector might be needed.

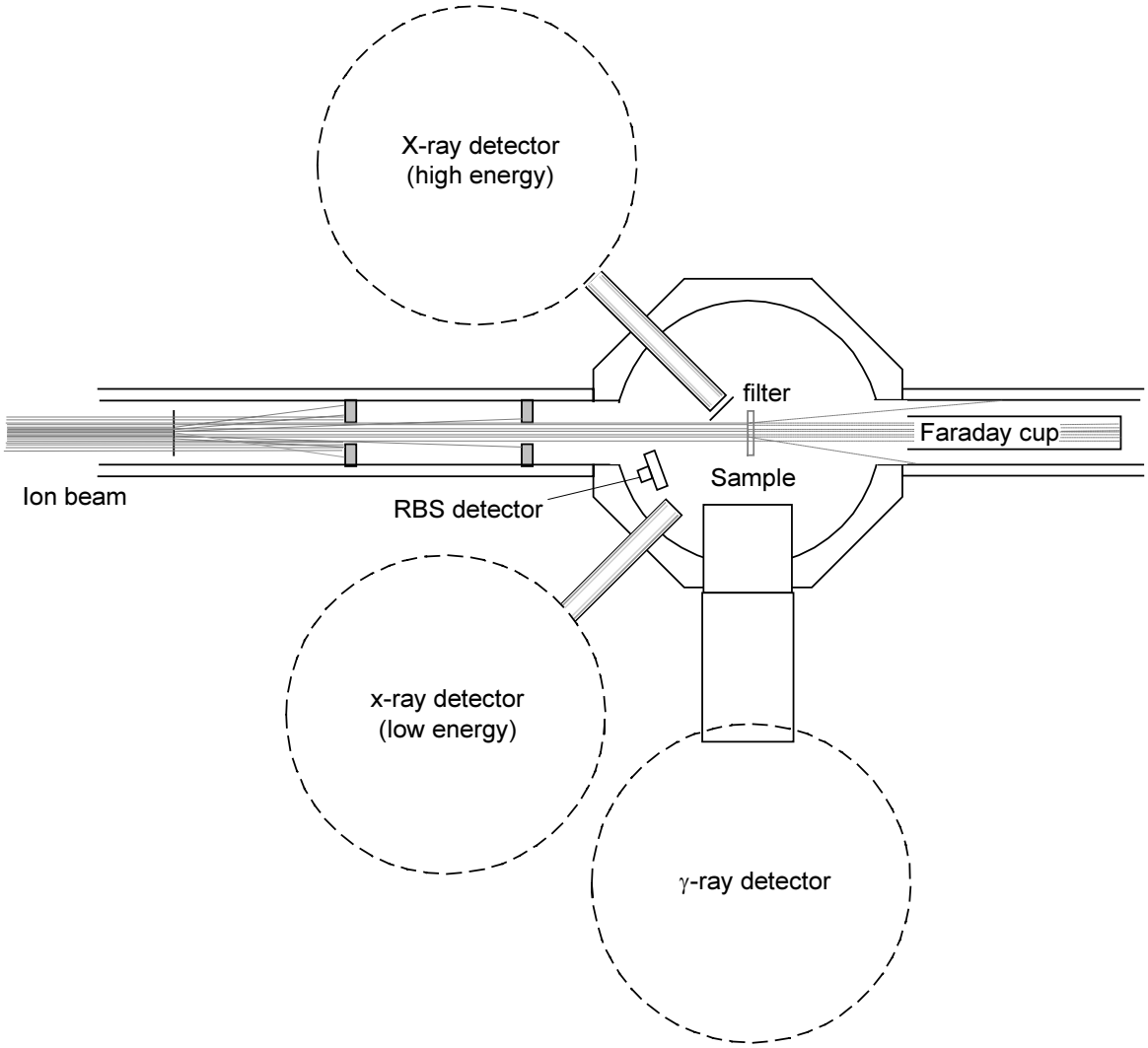

FIG. 13. One of the possible detector arrangements in the target chamber.

Positions of the PIXE detector and the sample are of importance for the positioning of other detectors that might be simultaneously used. One of these is the detector positioned into the backward angles usually between 150^{o} and 170^{o} (typically 165^{o}). Sometimes a γ ray detector for PIGE measurement is used simultaneously, positioned usually at an angle of the 90^{o} (lowest Doppler peak broadening). Since both X ray and γ ray detectors are cooled with liquid nitrogen, a dewar will furthermore limit arrangement possibilities. In Fig. 13. one possible arrangement for two PIXE detectors together with PIGE and RBS detectors is given.

All geometrical parameters have to be very well defined. Otherwise, significant errors can occur if some of the angles are not consistent. Since the direction of the beam and the detector are mostly very well defined, the sample surface itself is the only one that can be unintentionally changed among different samples. Quantitative analysis will be incorrect if target tilt is present. In Table IV effect of target tilt in different beam-target-detector arrangements is given.

3.3.1. X ray spectrometers

Moseley laid the foundations of the X ray spectrometry in 1914, recording a spectrum of X rays using a diffraction crystal spectrometer and a photographic plate. The principle of today's wavelength dispersive X ray spectrometers is basically the same, with a position sensitive detector used instead of the photographic plate. In spite of the superior energy resolution, the rather low efficiency of such a detector limits its applications in PIXE to specific problems when better energy resolution is essential [28, 29]. Higher solid angles can be achieved with the use of already available curved crystals, which are still not used very often for high resolution PIXE measurements.

The energy dispersive X ray spectrometry (energy of X ray is measured by radiation detector) using scintillator or proportional counters could not be widely used in past due to their poor energy resolution. By the development of semiconductor detector technology, energy dispersive X ray spectrometry became superior in many fields of application and for all types of X ray excitation (electrons, ions or photons). In 1970 the first energy dispersive PIXE spectra were recorded in Lund using the Si(Li) X ray detector [30]. Since then, semiconductor Si(Li) detectors were further developed and remained the most suitable choice for the PIXE spectroscopy [31].

The intrinsic Ge detectors are a second choice of semiconductor detector, with slightly better energy resolution. Unfortunately, higher efficiency for high energy X ray region (above 20 keV), made the Compton scattering of particle induced γ rays emitted from the sample much more probable, increasing the background in the final PIXE spectrum.

Silicon is the material of choice in some other types of X ray detectors. In a thermoelectrically (Peltier effect) cooled Si p-i-n photodiodes (<10 mm^2 area, <0.5 mm thick), low capacitance of the detector and close positioning of the FET enables reduction of noise below 200 eV [32]. The charge-coupled device (CCD) used normally for imaging of visible light was also developed for the X ray detection. Such systems are used as position sensitive detectors in wavelength dispersive spectrometers. Materials with larger band gaps can be used as room temperature detectors, with mercury iodide giving the best-obtained results. Increasing number of other X ray detection principles such as semiconductor based microcalorimeters [33] or superconductor tunnel junction cryogenically cooled detectors [34] may soon increase use of alternative X ray detectors. In the review of solid state X ray detectors given by Kalinka [35], cryogenic calorimeters were mentioned as detectors with a theoretically best energy resolution.

3.3.2. Semiconductor detectors

When n-type and p-type silicon are brought into contact (pn diode), free electrons (from n type) and holes (from p type) near the junction recombine to create a region that is depleted of charge carriers. The space charge from the fixed sites creates an electric field in the depleted region. If radiation enters the depletion region and creates electron-hole pairs, the result is similar to that of an ionisation chamber. Electrons flow in one direction, holes in the other, and an amplitude of electronic pulse collected at the electrodes, corresponding to their total numbers, is proportional to the radiation energy.

In practice, a reverse bias voltage is applied to the diode, increasing the electric field (better charge collection) and increasing the size of the depletion region (larger sensitive volume of detector). This thickness is sufficient for the charge particle detection (surface barrier detectors).

For detectors intended for X ray or γ ray spectroscopy, much greater thickness of the depletion layer is needed. Since it is not possible to produce silicon with so low level of impurities to reach the properties of pure or intrinsic material, a Li compensation process was developed. Lithium (donor impurity) is diffused into the original p material by exact amount to balance donor with acceptor

impurities. Once the diffusion process is completed the large volume of material with properties similar to that of intrinsic material is formed. The excess lithium at back surface forms a n+ contact, while on the other surface (detector front) a metallic p contact (evaporated or implanted) makes the second electrode of the Si(Li) p-i-n diode (Fig. 14) [36, 37].

The photoelectric absorption of X rays in silicon is the predominant absorption process below 50 keV X ray energy. At some 10 keV, Compton scattering probability is just 1% of the photoelectric effect probability in silicon. During the photoelectron slowing down process, numerous electron hole pairs are produced. In a high electric field (typical bias of detector is 1000 V for diodes around 3 mm thick), electron and holes are collected in a very short time (less than 100 ns). The mobility of charge carriers in silicon is similar for both charge carriers (2.1×0^4 cm^2/Vs for electrons and 1.1×0^4 cm^2/Vs for holes at 77K).

The number of electron-hole pairs produced by a keV energy X ray photons in silicon is of the order of 1000 (3.76 eV per electron-hole pair). Thus, the main limitation of the Si(Li) detector′s energy resolution is coming from the statistical nature of the electron-hole creation process. Thermal contribution to the noise is the other limitation parameter. At room temperature, leakage current in reverse biased diode is significant and its random fluctuations represent a significant noise source. This noise and the noise generated in the input stage of preamplifier are reduced by cooling the detector and the first stage of a preamplifier to the liquid nitrogen temperature of 77 K.

Apart from the noise, incomplete charge collection (ICC) is another Si(Li) detector limitation [38, 39, 40]. In periphery regions of the detector, insufficient electric field gives rise to the events where part of the created electron hole pairs are recombined before they are collected at the electrodes. In order to improve the detector performance, manufacturers frequently mount internal collimators, positioned between the detector and the window. Additional collimators can be positioned externally by the user if unwanted ICC effects need to be reduced. However, the front contact layer has always a thin region (from few tens up to few hundred of nanometers) with incomplete charge collection. Some of the ICC features (low energy tail of the Gaussian peak) that are further discussed in Section 3.2.4 are therefore always present in the PIXE spectrum.

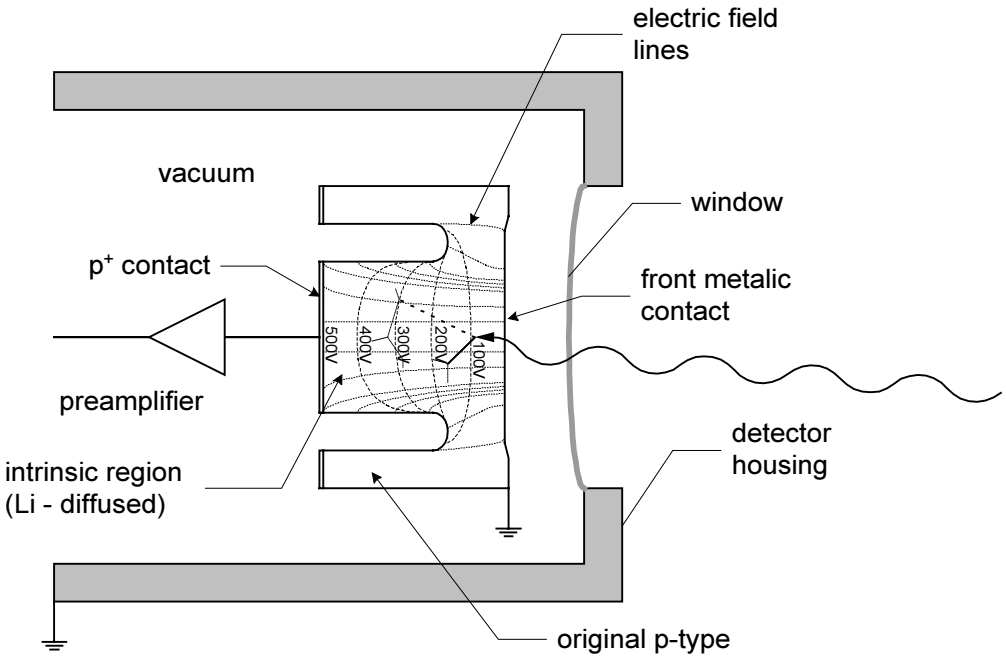

FIG. 14. Schematic presentation of the cross section of the typical Si(Li) detector configuration.

3.3.3. Pulse processing

3.3.3.1. Preamplifier

Output of most pulse type radiation detectors is a charge pulse Q. A voltage pulse produced by integrating this charge pulse across the summed capacitance of detector, connecting cable and input of the amplifier, is too small to be useful for all semiconductor detectors. Therefore a charge sensitive preamplifier has to be used.

The preamplifier is usually located as close as possible to the detector, minimising the capacitance and consequently the noise. The input FET of the Si(Li) detector preamplifier is located inside the cryostat, and is cooled to reduce the noise level. The charge pulse from the detector is integrated by the feedback capacitor of the preamplifier. Unlike most integrating amplifiers that use a passive resistor in parallel with the feedback capacitor to discharge it, the Si(Li) detector preamplifier has no resistor, and allows the voltage to build up in a random staircase signal (Fig. 15). Periodically, a pulse of light on the drain of the input FET discharges the integrating capacitor. The information about the charge collected by detector is contained in the height of the step. During reset and reset recovery time, an inhibit signal is generated in order to prevent data collection during this period.

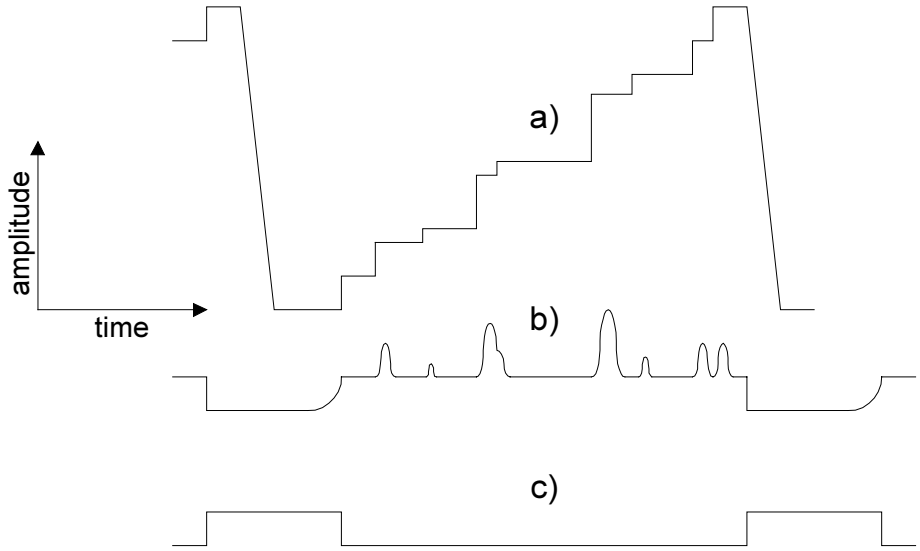

FIG. 15. a) The output from the pulsed reset preamplifier, b) the same events after passing through an amplifier, c) the inhibit signal.

The high voltage detector bias is not connected to the diode directly, but through a filter consisting of high value resistor (typically 10 MΩ) and a capacitor. The power required for the operation of the preamplifier is supplied through a multiconductor cable from the amplifier.

3.3.3.2. Amplifier

Spectroscopy amplifier is needed to improve the signal to noise ratio, to retain the information about the event's energy, and to shape the pulse for further transmission in the nuclear instrumentation chain. It accepts the signal from the preamplifier and produces output pulse that is approximately Gaussian in shape, proportional in amplitude to the input pulse step. Relatively long shaping constants (higher than 4 μs) are preferably used in Si(Li) detector amplifiers. The discharge of the preamplifier capacitor produces a very large, negative, saturated pulse in the amplifier. This signal is eliminated from further processing by the inhibit signal, from the preamplifier (Fig. 16).

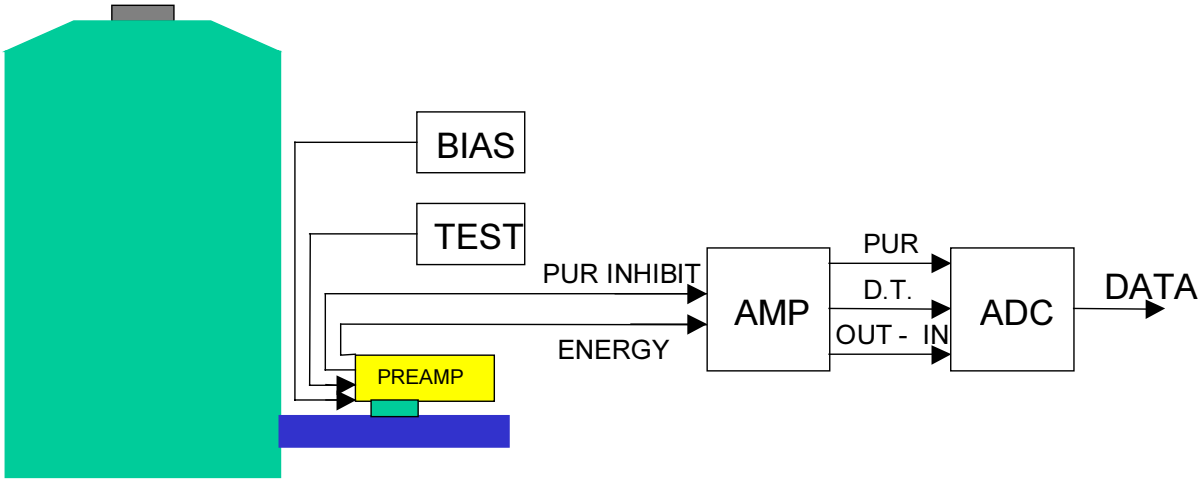

FIG. 16. Schematic presentation of the pulse processing.

The signal from the amplifier is analysed by the analog-to-digital converter (ADC). The ADC analyses the maximum amplitude of each pulse and converts it to a digital value (further discussed in Section 3.4).

Some of the detector producers are supplying detector with a custom pulse processor unit that comprises of amplifier, bias supply and ADC. Also a digital preamplifier/amplifier design was recently presented, having superior signal to noise characteristics.

The physical design of Si(Li) detector and dewar assembly are numerous (Fig. 17). Dependent on the geometrical set-up of the chamber the most suitable detector design can be selected. However in the most common PIXE set-up, a 135^{o} angle in the horizontal plane is used. To enable the largest solid angle of the PIXE detector (that will indirectly minimise sample damage), diameter of the detector housing has to be as small as possible, with the detector crystal as close as possible to the detector window.

3.3.3.3. Energy and FWHM calibration

The energy of an X ray is converted during the process of charge creation in semiconductor diode to the charge pulse and subsequently after amplification to the voltage pulse. The analog voltage pulse height is converted further to the digital output from the ADC (channel number). Channel number N_{ch} is linearly proportional to the initial X ray energy (E) according to relation:

$$N_{ch} = A_1 + A_2E \tag{6}$$

Coefficients A_1 and A_2 are energy calibration coefficients that define positions of X ray peaks at the PIXE spectrum. These coefficients are needed for the procedure of fitting theoretical spectrum to experimental one. Since the energy resolution of the Si(Li) X ray detector depends on energy as well, it also has to be calibrated. Usually, peak's full with at half maximum (FWHM) is calibrated, using simple relationship like:

$$FWHM = (A_3 + A_4E)^{1/2} \tag{7}$$

where A_3 and A_4 are FWHM calibration coefficients which have to be determined.

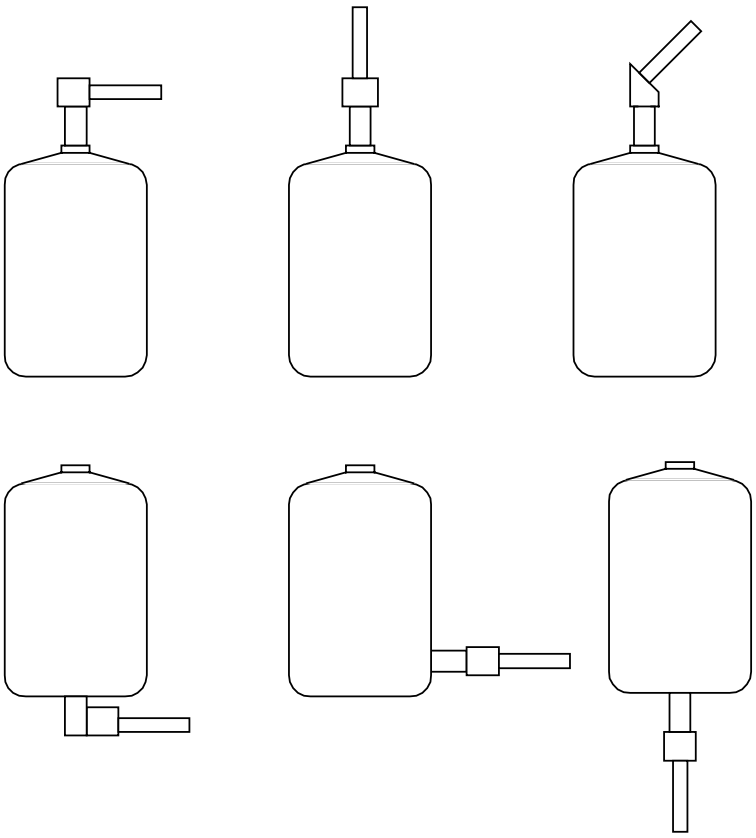

FIG 17. Some configurations of the Si(Li) detector.

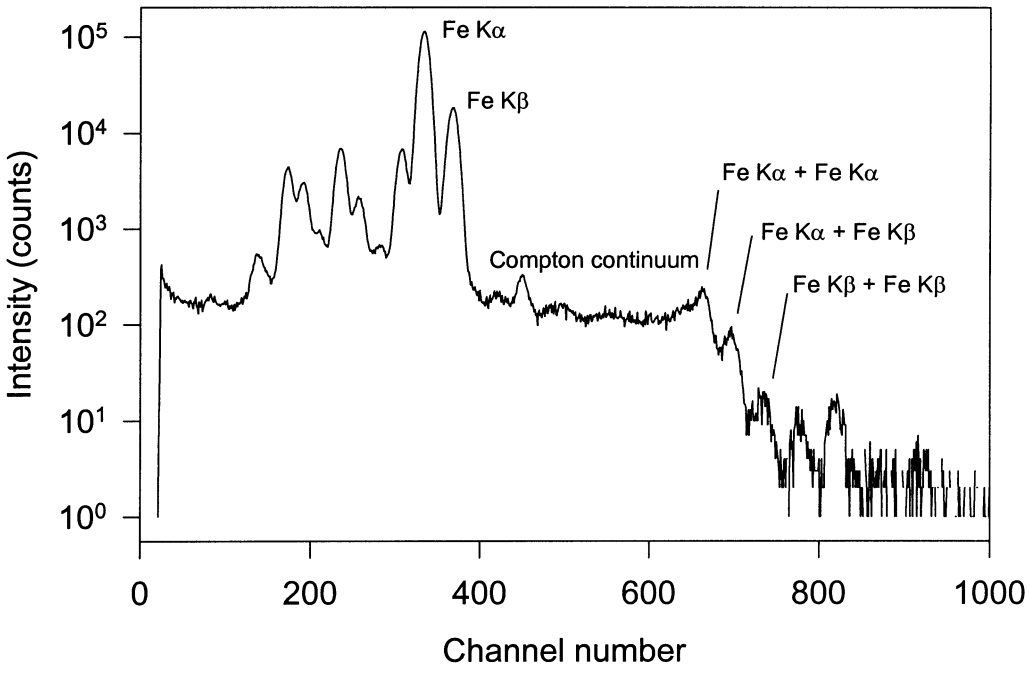

FIG. 18. PIXE spectrum with typical pile-up structures.

In order to easily compare the quality of different X ray spectrometers, the FWHM of the 5.895 keV Mn Kα X ray line (the principal line of the ^{55}Fe radioisotope source) is reported. With Si(Li) X ray detectors a value better than 200 eV should be obtained (typically 160–180 eV for common Si(Li) detectors). The best values achievable with a long shaping constants and small count rates with a state of the art Si(Li) diodes and pulse processing systems today can be as small as 130 eV.

However, real measurement conditions are far from ideal, with many reasons that can degrade the performance of the PIXE spectrometer. Some of these are discussed bellow.

3.3.3.4. Noise pickup

Shielded coaxial cables are used in all connections to minimise the pickup of noise from stray electromagnetic fields. Nearby equipment having high frequency switching of large currents can still induce transient signals. It is necessary sometimes to remove such equipment away from the X ray detector. Mechanical vibrations and intensive sound around the target chamber can also serve as the source of noise that will degrade the performance of the PIXE spectrometer.

The outer shield of the cable serves also as a connection between the chassis of all the components and the ground. If some of the components are widely separated, and therefore internally not connected to the same ground point, a common ground potential will be maintained with some current flow through the cable shield (ground loops). In such conditions grounding of the chamber, detector, amplifier and data acquisition system to the same ground point must be ensured in order to eliminate ground loop noise.

Most of such problems will result in degraded energy resolution of a X ray spectrometer. Any modulation of the main noise level observed by an oscilloscope at the output from the spectroscopy amplifier can indicate the noise pickup.

For the windowless, or ultra thin window Si(Li) detectors, transmittance of outside light to the detector diode has to be considered as well.

3.3.3.5. Backscattered protons in Si(Li)

The entrance window of the most common X ray detectors is made of beryllium foil. Protons scattered from the target, having energy higher than 1.3 MeV can pass through 25 μm of beryllium with the rest of their energy being deposited in detector. In addition to significantly increasing the reset pulse frequency and consequently the dead time, such events can also degrade the performance of the preamplifier. Response of the pulse processor to the backscattered protons can be quite different, from tolerable dead time increase to significant increase of background and worsened energy resolution.

Backscattered protons can be avoided either by introduction of an additional filter (stopper foil) or by an appropriate proton deflection system. The first possibility will reduce the X ray energy region covered by detector, resulting in smaller range of elements being analysed by PIXE. Deflection system seems to be the more appropriate choice, but relatively large dimensions required will cause significant reduction of the detector solid angle. However, if two PIXE detectors are used with one of these displaced to a larger distance from sample, a magnetic deflector system can be positioned in the space between [41]. Small solid angle of such X ray detector will not be a serious disadvantage due to the much higher production cross sections for the K X ray lines of light elements.

The effects of backscattered protons are also very dependent on the sample itself. Matrix component dependence of the number of backscattered protons per X ray is studied by Calligaro et al. [42] in more detail.

3.3.3.6. Pile up

Since Si(Li) X ray detectors require relatively long pulse processing time, the probability that two pulses arrive within the resolving time of the system, becomes significant at the signal rates above 1000 Hz. Distortion of PIXE spectrum results with an additional "sum" peak at the double energy of the parent peak. In addition pile-up continuum at the spectrum region above the parent peak energy, is also observed (Fig. 18).

Substantial reduction in the pile-up background can be achieved using a pile-up rejector, frequently incorporated into the spectroscopy amplifier [43]. It provides an output logic pulse for the associated analog to digital converter (ADC), that disables the collection of piled up events (Fig. 16). Recently, Homman [44] developed technique of pile-up rejection using the pulse shape analysis.

The most elegant way of the elimination of pile-up effect is the use of on-demand beam deflection. After the arrival of the pulse to the detector, the preamplifier pulse triggers the electrostatic deflector that deflects the beam off the collimator system and keeps it deflected during the whole pulse processing time. There are several advantages of this approach. Pile-up effect is eliminated almost entirely, sample damage is decreased, and the dead time correction is not needed since the measured collected charge at the Faraday cup is actually the live charge. Technical details about the on-demand beam deflection can be found in paper of Thibeau [45].

And finally, reducing the most intense peaks in the PIXE spectrum can reduce pile-up too. This can be achieved either by the reduction of detector count rate (decrease of current or increase of the sample to detector distance), or by the use of appropriate X ray absorbers that will decrease intensity in selective parts of PIXE spectrum. Use of X ray absorbers will be discussed in more details in Section 3.2.5.

3.3.3.7. Test pulse, dead time

In order to check the overall functioning of the pulse processing system, a test pulse from a pulser can be attached to a test input at the preamplifier. A noise contribution from the preamplifier and amplifier, as well as the noise pickup can be controlled prior to the measurements.

Test pulse processing through a whole system during the measurements can be also a convenient way of determination the system dead time, which is very important in the quantitative PIXE analysis using the fundamental parameter or standardless procedure. The most significant contributions to the dead time are those from ADC and amplifier.

3.3.4. X ray line shape

If the statistical nature of the detection process is the only departure from the ideal X ray energy analysis by a Si(Li) detector spectrometer, a monoenergetic X ray will produce a pure Gaussian lineshape in the spectrum. But, neither the characteristic X rays in the PIXE spectrum are monoenergetic peaks, neither the lineshape of the Si(Li) detector is pure Gaussian [46].

3.3.4.1. PIXE line shape

The fine structure of the characteristic X rays emitted after the ionisation by fast ions can not be resolved by a Si(Li) detector with limited energy resolution. However, these features need to be considered for the reliable PIXE analysis. Using the high-resolution X ray spectrometer, some of the PIXE lineshape features become visible [47]. X ray spectrum of iron obtained by a high resolution crystal X ray spectrometer is presented in Fig. 19.

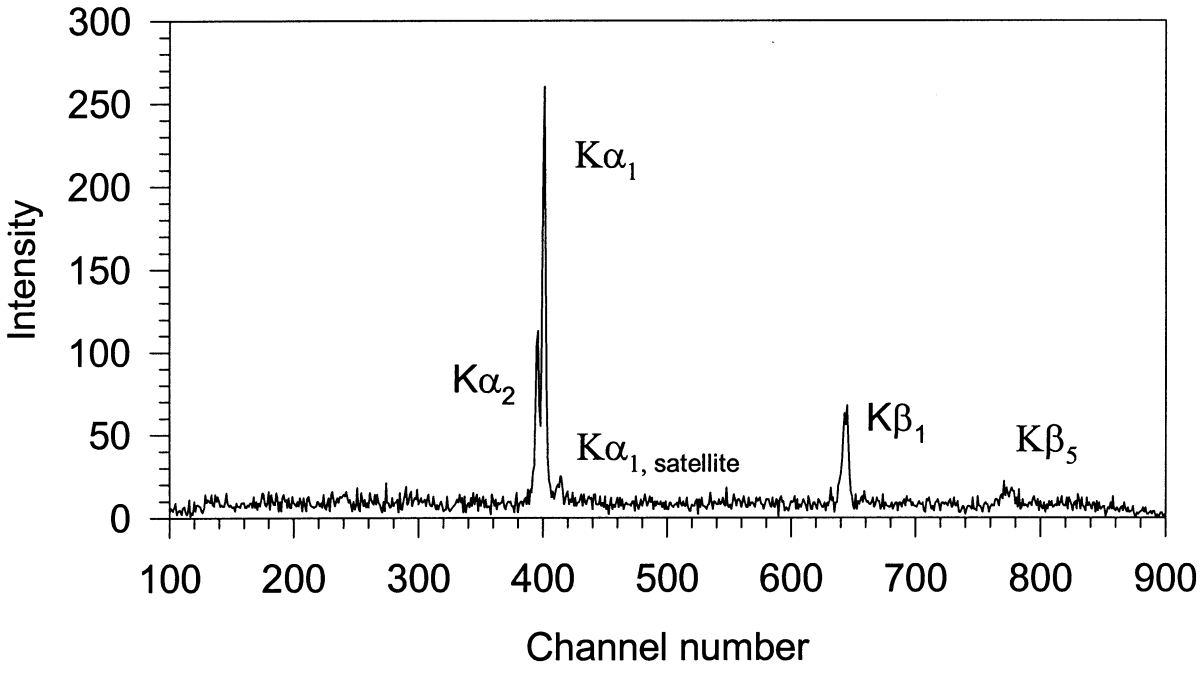

FIG. 19. X ray spectrum of iron using the high resolution crystal spectrometer.

The natural width of an X ray line is rather small (from almost zero to 30 eV) when compared to the Si(Li) detector energy resolution. Since the intrinsic X ray line shape has the Lorenzian distribution, wide Lorenzian tails distort the peak shape even for the detectors with low resolution. Lorenzian peak broadening is mostly visible in the L line X ray series [48].

High energy satellites arising from the simultaneous creation of one or more higher shell vacancies (multiple ionisation) are especially important in the heavy ion PIXE. Satellite lines are present at energies slightly higher than the energy of the main line, resulting in the small energy shift when Si(Li) detector is used.

Radiative Auger effect (RAE) is the most significant for the light elements. Both Kα and Kβ lines are accompanied by asymmetric low-energy band structures arising from simultaneous emission of an X ray photon and an Auger electron. Due to the overlapping of these bands with a low energy tailing of the Si(Li) detector, inclusion of RAE lines into the fitting code can be important [49].

If PIXE is performed on thick target samples, intensive X ray peaks above about 15 keV are accompanied by a finite tailing feature at the low energy side of the main peak. This contribution comes from the detection of photon that is emitted from the Compton scattering of the particular X ray that took place in the sample itself. Therefore, this effect cannot be seen in the thin samples.

3.3.4.2. Si(Li) detector line shape

Response of the Si(Li) detector to the monoenergetic X rays is dominated by a Gaussian peak, corresponding to the full energy transfer from the X ray to the electron-hole pairs. Due to the noise and statistical nature of the process, distribution of the pulse height has a Gaussian distribution.

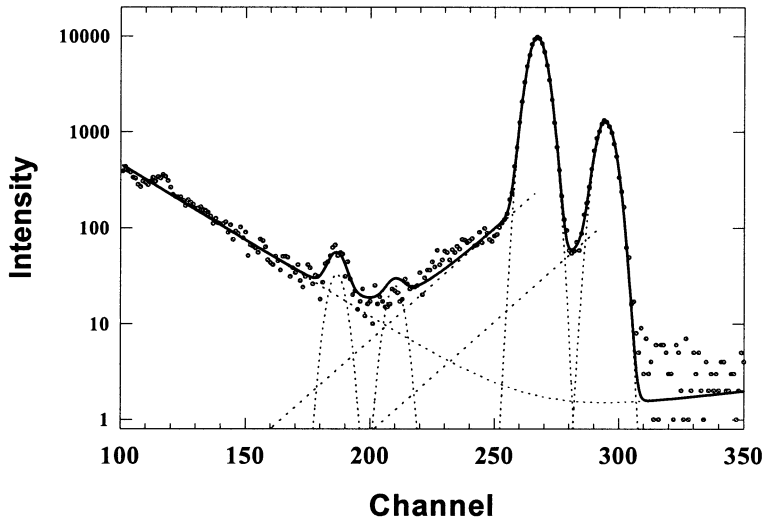

FIG. 20. PIXE spectrum of the Mn K lines, indicating contributions of the Kα and Kβ photopeaks, escape peaks, long exponential tail and background.

Apart from the main peak, each X ray peak in the spectrum is accompanied by the escape peak at the energy approximately 1.75 below the parent peak energy. This energy is slightly higher than the 1.742 keV energy of the silicon Kα line. The escape peak arises from the escape of the characteristic X ray of silicon emitted inside the detector crystal after the photoelectric absorption of the detected X ray. Relative contribution of the escape peak is energy dependent and can be predicted using the simple model [50]. Larger contribution to the escape peak have low energy X rays (about 2% for Ca).

Other components of the peak shape are tailing features, which can be in most cases described by just one, two, or maximum three simple functions. These functions are the flat shelf extending to the zero energy below the parent peak, and one or two exponential "tails" (long and short), below the parent peak (see Fig. 20).

The origin of these features is less obvious and is still subject of research. Most of the tailing contribution can be explained by an ICC in the surface regions of the Si(Li) detector. Energy dependence of the tailing contribution (increases with decreasing energy) is the first argument that indicates its near surface origin. Existence of the Si absorption edge in efficiency curves of the Si(Li) detectors also indicate the presence of silicon surface absorber. This region is historically named as a “dead layer”. However, the concept of single dead layer was abandoned, introducing zones of incomplete charge collection. The ICC surface zone consists of regions with zero and partial charge collection. More about the nature of ICC in Si(Li) detector and consequences to the PIXE spectrum analysis can be found in a number of papers by Campbell [38].

Tailing features are generally different among the different detectors, depending mostly on the production characteristics. The height of flat shelf feature is for example quite sensitive on the thickness of the front metal contact of the detector. To a certain extent some relationship of the exponential tail and ICC was also observed. Unfortunately until now, modelling of these features is made on a pure empirical base. Therefore in order to perform reliable PIXE spectrum analysis, it is necessary to model the lineshape of each particular detector including the energy dependence of the lineshape components. For this purpose a set of pure single elements samples can be used.

Apart from the tail shape, there were reports that some detectors exhibit time dependent shape or intensity of the tailing features. In the case of some old detectors with elevated ICC, tailing features can be unusually high. In some cases, aperture that limits the sensitive region of the detector to its central regions can significantly improve the peak shape.

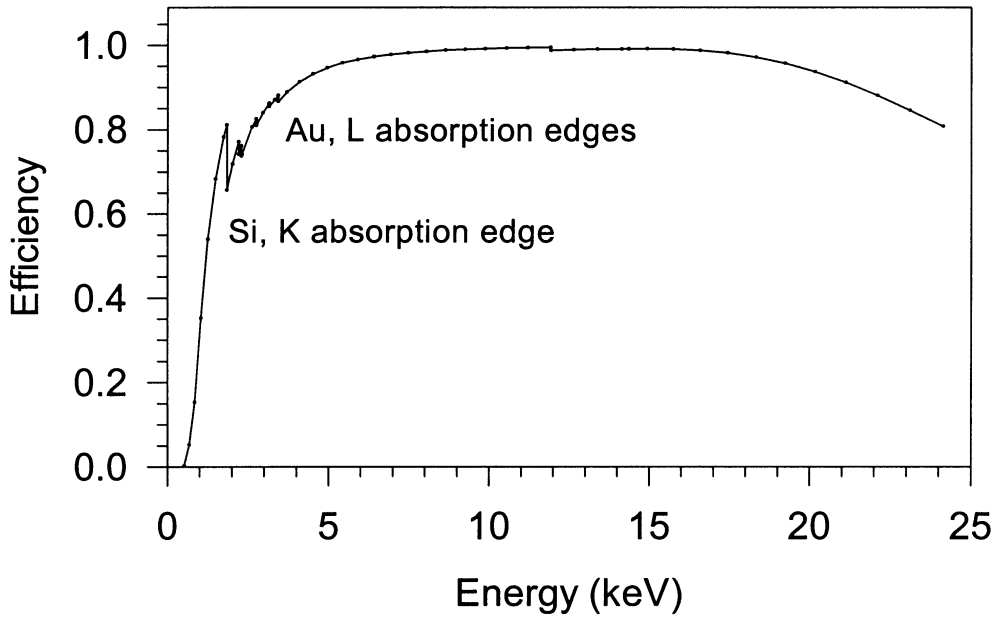

FIG. 21. Intrinsic efficiency curve of an Si(Li) X ray detector calculated for 8 μm thick Be window (for details see text).

3.3.5. Detector efficiency

Energy efficiency of the Si(Li) detector can be determined by either direct measurements or by the theoretical predictions. Theoretically, the absolute efficiency ε of the detector is the product of detector solid angle Ω/4π, and its intrinsic efficiency ε_i. By neglecting the energy dependence of detector solid angle (due to the different X ray mean interaction depth in the detector), the detector efficiency is:

$$\varepsilon = \frac{\Omega}{4\pi} e^{-\sum_{i=1}^{4} \mu_i t_i} f_E (1 - e^{-\mu_{Si} D}) \tag{8}$$

The exponential term corresponds to the absorption in each one of the 4 layers in front of the detector (window, ice layer, contact layer and ICC layer). Factor f_E reflects the loss of events due to the Si K X ray escape, while the last term in Eq. (8) describes the effect of the finite detector dimensions. For 3 mm thick Si(Li) detectors, this term becomes important at the X ray energies higher than 10 keV.

As example, intrinsic efficiency for the 3 mm thick Si(Li) detector with 8 μm Be window, 20 nm of gold contact, 200 nm of ICC layer and no ice on detector surface, is calculated and presented in Fig. 21. The most important and the most complex part of the efficiency curve is its low energy part (from 0.5 to 5 keV). Direct measurement of efficiency in this range is impossible, since no such standard radioisotope source exists. The acceptable solution for the efficiency measurement can be found in the direct use of pure element standards (thin or thick) and PIXE measurements. Using the existing database for the fundamental processes involved in emission of the characteristic X rays, detector efficiency is the only unknown component. In this way, user can check validity of the assumptions for the ICC and contact layer thickness.

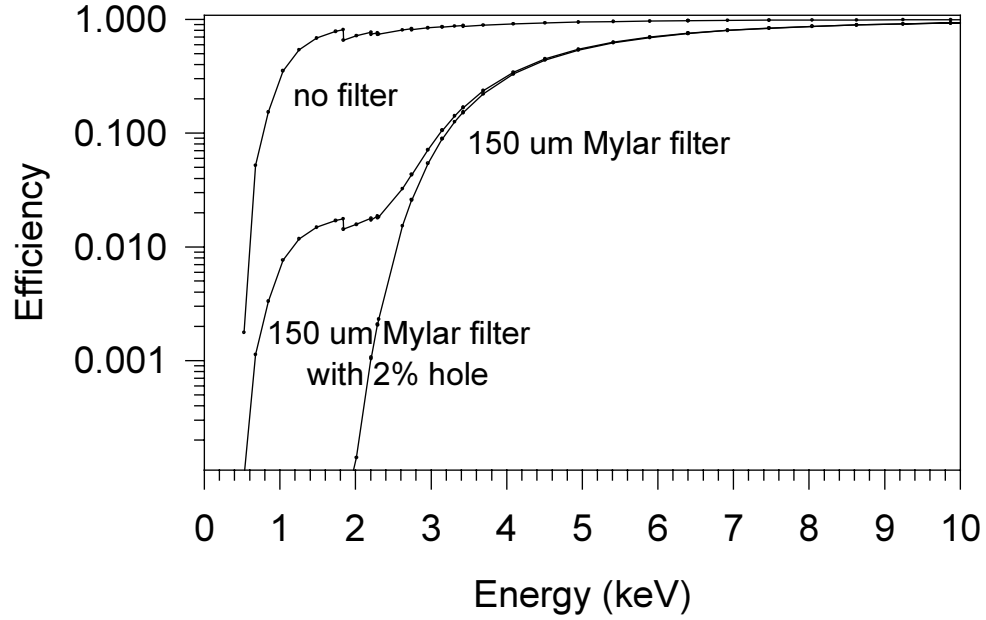

FIG. 22. Efficiency curve of the Si(Li) detector without any filter, with 150μm Mylar filter, and 150μm Mylar filter with a 2% hole.

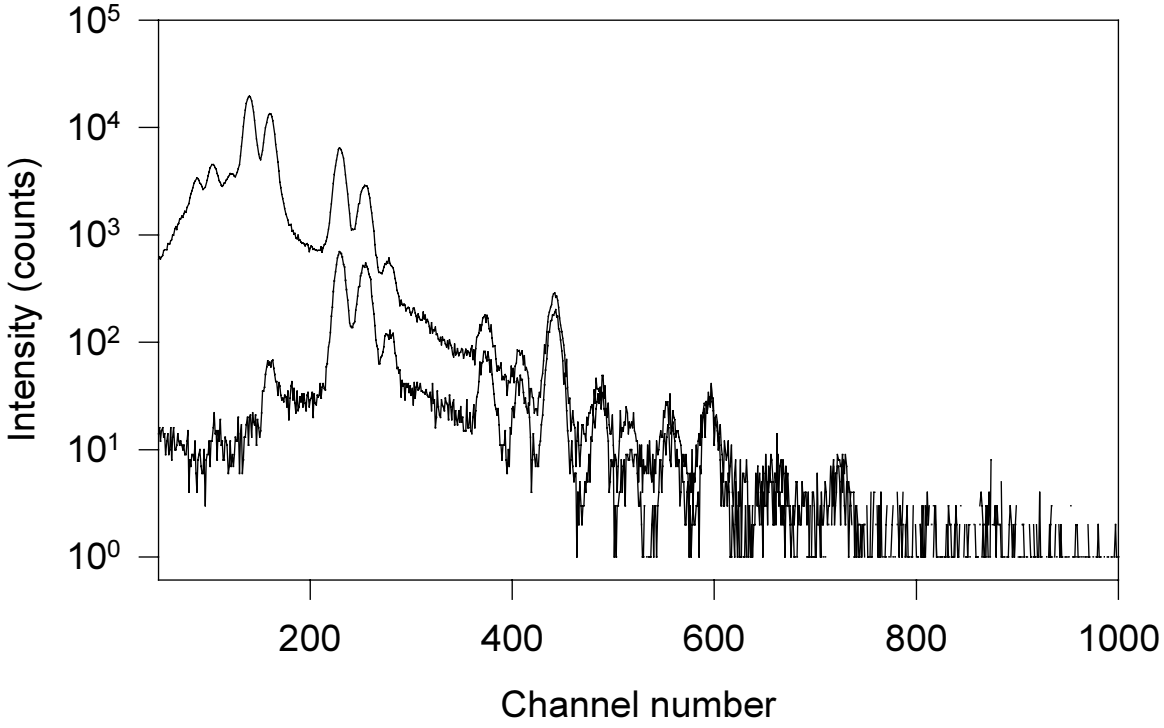

FIG. 23. Two PIXE spectra using the same current of 2 nA and total accumulated charge of 1 μC, with (B) and without (A) the filter. Much lower total number of counts in spectrum B, shows that significant increase of the beam current or detector solid angle can be allowed. This will increase sensitivity for high-energy part of the spectrum.

3.3.6. X ray absorbers

Much higher X ray production cross section for light elements and their generally higher natural abundance results in much higher yield of low energy X rays (below 5 keV). Practical limitations of Si(Li) detector to accept high count rates make it frequently important to use X ray absorbers (filters) that are placed in front of the X ray detector. In that way the intensity of low energy X rays is decreased (see Figs 22 and 23).

Filters are usually placed in front of the detector mounted on a cap attached just in front of the detector window. If one needs to change filter during the experiment, without opening the chamber, a remotely controlled filter changer can be designed as well.

Among the most suitable filters are foils made of different polymer materials such as Mylar, Kapton, Perspex and similar. Since these are composed of light element carbon, oxygen and hydrogen, energy dependence of X ray transmission is a convenient smooth function without absorption edges. A few hundred microns thick foil will attenuate almost completely K X rays of aluminium and silicon, while the X rays of elements such as potassium and calcium will be significantly reduced (Fig. 23). Aluminium foil of different thickness is another material of choice for the absorbers.

However, there is significant disadvantage in use of such thick filters. The information about the light element abundance is completely filtered out. This is why filters with central hole (few percent of detector area) are sometimes used. These "magic" or "funny" filters are ideal in qualitative PIXE analysis. In case of quantitative analysis, geometrical effects of central hole on energy dependence of X ray transmission have to be carefully estimated.

Selective filtering [51] uses the presence of absorption edges in X ray attenuation. For specific samples where just one or group of elements limits the sensitivity in particular part of PIXE spectrum, by appropriate choice of filter material one can significantly improve PIXE capabilities. Sera and Futatsugawa [52] gave also several examples of the X ray absorber design in their comprehensive review.

For the quantitative analysis, exact thickness of the filter needs to be known. Direct filter thickness measurement often does not match the X ray attenuation characteristics that are modelled by the particular quantification software. This is because the mean path of the X ray through an absorber may not match its physical thickness and because of the existence of errors in data for filter density, its stoichiometry and X ray attenuation database. Therefore a set of standard reference materials can be used to adjust the filter thickness that gives the best matching of reference values with a measured ones.

3.4. DATA ACQUISITION SYSTEMS

3.4.1. Multichannel pulse height analysis

Energy of the detected X ray is converted in the pulse processing electronics to the voltage pulse delivered at the output of the spectroscopy amplifier. This is an analog signal (pulse amplitude) which has to be converted to a digital number in a device called multichannel analyser (MCA). The MCA spectrum consists of a certain number of channels which number is a linear function of X ray energy. Each channel is actually a counter that counts events in the corresponding energy interval, forming the final energy spectrum on the MCA screen.

The key element of a MCA is the analog to digital converter (ADC — mentioned already in the Section 3.2.3.) and MCA storage memory. The ADC output is stored in memory with as many addressable locations as the maximum number of channels into which the recorded spectrum can be subdivided. Number of memory locations (channels) is usually made a power of two, with 1024 or 2048 channels being the most common choice in PIXE experiments.

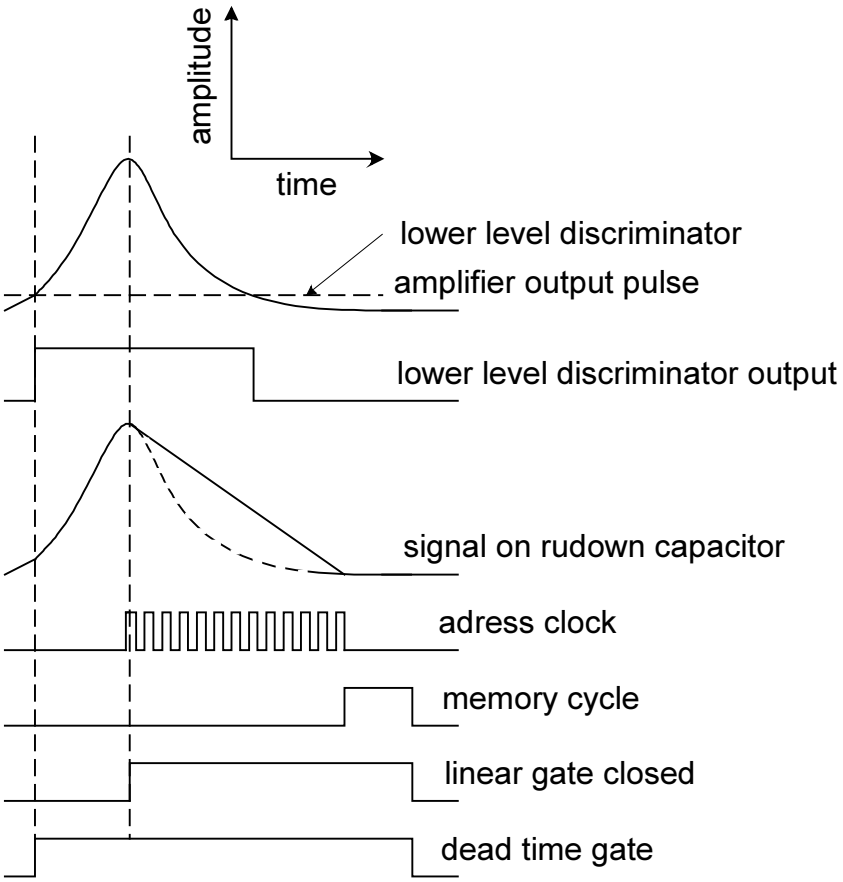

FIG. 24. Signals in the Wikinson ADC.

The construction of most ADC's is of Wilkinson type. It uses the input pulse to charge the capacitor until the peak of the pulse is reached. The time of the peak maximum is detected by the zero crossing of the pulse derivative. Using the constant current source, the capacitor is then linearly discharged. A clock (usually 100 MHz) measures the time of the ramp decrease, while the address register counts a discrete number of these periodic clock pulses. The number of pulses will correspond to the particular channel number in the spectrum. The memory section of an MCA provides one addressable location for every channel.

The important specifications of an ADC are its speed, linearity of conversion and resolution of the conversion. Signals between 0 and typically 10 Volts are accepted and converted to a number of channels determined by a conversion gain. Typical resolution and linearity of the conversion are usually acceptable for the routine PIXE applications and can be easily tested using a reference pulser. The lower level discriminator incorporated in the ADC is used to recognise the arrival of the amplifier output pulse. It is usually set just above the noise level. In Fig. 24, schematic presentation of the signals in the Wilkinson ADC during the process of conversion is given.

The other ADC feature important in particular for the PIXE analysis is its conversion speed, or the ADC dead time. During the conversion the ADC is unavailable for processing. This time is typically between 10 and 100 μs. It is therefore important to measure the "live" time, to account for lost pulses inhibited while the ADC is "dead". In order to account for all contributions to the dead time, inhibit signal from the amplifier has to be connected to the ADC. The total dead time will be superposition of the amplifier and ADC dead time.

3.4.2. MCA hardware and software

A multichannel analyser consists of an ADC, digital memory and display. Historically a stand alone MCA incorporating all these functions was for many years used as the main data acquisition instrument for various spectroscopies employing pulse height analysis. After the acquisition, data were transferred to the data analysis computers.

By the development of computer technology, data acquisition became one of the tasks of the data analysis computer. For the simplest single parameter pulse height analysis, MCA is today just an electronic module inserted in one of the slots of a personal computer, with an external ADC, or ADC being incorporated into the module. The memory needed to store the data is now the main computer memory and the hard disc, while the computer screen is used for the spectrum display.

3.4.2.1. NIM modules

Most of the commercial nuclear electronic instrumentation is designed in accordance to NIM (nuclear instrument module) standard. In addition to the various bias power supplies and analog or logic electronic modules, NIM modules of ADCs or complete MCAs are also available. In such devices, data output is connected to a personal computer with appropriate software MCA emulation.

ADC as a separate module is used mostly in the multiparameter data acquisition connected to the computer through the data bus box (e.g. in the nuclear microprobe PIXE experiments). Digital output of the ADC needs to be stored in a separate buffer module or in the PC plug-in card memory.

MCA NIM modules generally consist of an ADC and buffer memory and are connected to the standard ports of the PC. Such modules can be used in a single input or multiple input (multiplexer) modes. Multiplexer/router can enable simultaneous use of more detectors (e.g. two PIXE detectors or PIXE and RBS detectors), but care has to be taken in the dead time correction procedure of such a system.

3.4.2.2. PC cards

The most economical MCAs today are plug-in cards for personal computers providing a computer-controlled data acquisition. Most of these cards have built in ADC, microprocessor and program memory and are generally single input plug-in cards with a software support. In the case of PIXE spectrometry, PC cards with built in ADC that can accept inhibit signal from the preamplifier are recommended. Otherwise, PC cards which are able to accept digital pulses from external ADCs are recommended.

3.4.2.3. CAMAC

The CAMAC standard differs from NIM standard in one important way. Instead of just providing modules with power (as NIM bins), the CAMAC crate has a built-in, digital data bus to provide computer communications with the modules. This system is designed for use in more complex data acquisition systems (multiple detectors, many dependent parameters, large detector arrays) than generally found in conventional PIXE set-up. More often CAMAC based data acquisition is found in multiparameter systems such as those required for work with nuclear microprobe.

3.4.2.4. MCA software

Data acquisition software today offers many advanced functions that are useful for online interpretation and qualitative analysis of PIXE spectra. Typical functions of interest for PIXE are:

— energy calibration, peak search and peak identification,
— peak centroid and peak shape (FWHM) calculations — needed for the energy calibration calculations and energy resolution control,
— calculation of integral or net area counts in the peak by a simple background subtraction and statistical uncertainty,
— different spectrum display features (expand, overlap, log/lin vertical scale,...),
— hardware control functions.

Different hardware and software capabilities of particular multichannel analysis systems can be found in materials supplied by the producers of such instruments [31].

3.5. DATA ANALYSIS SOFTWARE

The extraction of X ray peak areas from the PIXE spectrum and their correlation to the concentration of particular element, form the basis of quantitative PIXE analysis. A large variety of PIXE software packages exist today, with most of them available to calculate both X ray peak areas (intensities) and respective elemental concentrations.

Extraction of X ray intensities from PIXE spectrum is the first step in the quantification procedure. This was historically also the first step that was processed using the computer routines. Almost exclusively, programs are based on the least squares fitting of the model spectrum to the experimental one. The main difference between them arises from the different approaches in background and peak shape treatment.

Relationship between X ray intensities and elemental concentration was in early days of PIXE experimentally determined producing empirical calibration curves. These were valid just for particular sample type such as thin samples, or thick samples of particular matrix composition. This approach was limiting application possibilities of PIXE significantly. Improvements in the accuracy of the data base describing all physical processes involved in X ray detection, enabled computer modelling of the whole PIXE experiment. One of the most complete programs for simulation of PIXE spectra is recently developed VIVA-Lab [53]. In addition to the fitting routines, most of the present PIXE software packages are now available to calculate elemental concentrations directly from a PIXE spectrum.

The quantification procedure is based on Eq. (2). This equation is given here as the energy integral that describes the intensity I of each X ray line of the element Z as measured by particular detector of efficiency ε_Z (see Eq. 8):

$$I(Z) = \frac{N_{Av}\,\omega_Z\,b_Z\,\varepsilon_Z}{A_Z}\,\frac{Q}{e}\,C_Z \int_{E_o}^{E_f} \frac{\sigma_Z(E)\,T_Z(E)}{S(E)}\,dE \qquad (9)$$

Here, N_{Av} is Avogadro number, A_Z atomic mass, ω_Z and b_Z are fluorescence yield and branching ratio of particular X ray line, while Q/e is the total number of beam particles arrived at the target. C_z is element concentration (if it is function of depth it is inside the integral), σ_Z is X ray production cross section, T_Z is X ray absorption in the sample and S is the stopping power of ions in the material.

$$T_Z(E) = \exp\left(-\left(\frac{\mu}{\rho}\right)_{Z,M} \frac{\cos\phi}{\cos\theta} \int_{E_o}^{E_f} \frac{dE}{S(E)} \right) \qquad (10)$$

and

$$\left(\frac{\mu}{\rho}\right)_{Z,M} = \sum_i C_i \left(\frac{\mu}{\rho}\right)_i \tag{11}$$

where μ/ρ is mass absorption coefficient, α and θ are angles defined in Fig. 2.

The integral from Eq. (9) in most of the quantification programs transforms to the sum of a number of target layers that contribute to the resulting X ray yield for particular X ray line.

There now exist many software packages for fitting and/or quantification of PIXE spectra. Some of them are listed in Table V. With bold letters are programs that integrate all fitting and quantification routines. Some of the main characteristics of the programs are also listed in the table. Most of these run on personal computers having graphical presentation of experimental and modelled spectra.

TABLE V. EXISTING SOFTWARE FOR PIXE

AXIL [54]	Nonlinear least squares fitting routine, originally developed for XRF but may be used for simple (e.g. thin target) PIXE spectra. Background estimation (SNIP algorithm), background modelling (different functions).
DATTPIXE [55]	Intermediate and thick target corrections of inhomogeneous targets. Program designed for analysis of layered samples.
GEOPIXE [56]	Package that includes both spectrum fitting and quantitative analysis routines, designed for mainly geological samples. Includes large number of corrections such as secondary fluorescence, self absorption, background absorption edges (SNIP — statistics-sensitive nonlinear peak-clipping algorithm), escape peak and tailing features.
GUPIX [57]	Package that includes spectrum fitting and quantitative analysis. Digital top hat filter removes the background and doubly differentiates a Gaussian peak. Using the complete fundamental parameter data base and by appropriate modelling of the peak lineshape, number of parameters is reduced to one per element. Filtered data are compared to filtered model spectrum using the nonlinear least squares fit.
PIXAN [58]	Package that includes both spectrum fitting and quantitative analysis. Using the iterative background estimation (SNIP algorithm) and least squares fitting, intensities are converted to concentration using the routine for thick target yield calculation.
PIXYKLM [59]	PFIT — routine for least squares fitting of experimental spectrum KLM — calculations of effective cross sections developed for the routine aerosol analysis
SAPIX [60]	Nonlinear least squares fitting routine for PC98 (widely spread in Japan) and IBM PC computers + utilities: TRPC (spectrum format conversion), DEFF (detector efficiency calculations), XABS (X ray absorber transmission), ICPER (X ray production cross sections)
SESAMX [61]	Linear and nonlinear least squares fitting routine with interactive parameter input.
TROCON [62]	Intermediate and thick target corrections using iterative procedure that varies elemental composition of the sample towards the result. (TROJAX routine can be used for spectrum fitting).
TTPIXAN [63]	Intermediate and thick target corrections and various utilities (cross sections, attenuation, etc.). New versions have possibility of simulation of microPIXE images and reconstruction of 3D elemental composition.
TTPIXE [64]	thick target corrections using alpha parameter ($\alpha = \mu/S(E)$) method (α parameter is determined experimentally from the subsequent PIXE measurements of the same sample with different geometry and ion energy parameters)
WITS-HEX [65]	Fitting routine developed from the HEX code originating at FSU. Polinomial background or series of convex/concave parabolas. Developed for the aerosol analysis.

Many of these programs have proven their versatility by their usage in different PIXE groups. While selecting the particular software, attention has to be given to the database used in the program, modelling of the peak shape and treatment of the spectrum background. Among such universal programs able to treat the wide spectrum of different analytical problems, one has to mention GUPIX that is today probably the most wide spread PIXE analysis software. The type of the samples that is analysed mostly can be the other important criterion for the appropriate software selection (e.g. GEO-PIXE for the geological samples).

Apart from the routines for fitting and quantification, there are many routines (utilities) needed in the planning stage of the PIXE experiment. Choice of particular filter to be used for the analysis of some specific sample, X ray yield of particular element in particular matrix, range of ions in different samples, the mean interaction depth, and many other similar problems can be solved much easily using some of the available utilities. These are available as a separate programs (partially listed in Table V), or as a part of the main PIXE software package.

4. INSTRUMENTATION FOR RBS

4.1. INTRODUCTION TO RBS

RBS [66, 67] can be performed using the instrumentation coinciding in a large extent with that of PIXE. For example, the accelerator, the target chamber, the target holder and a large part of the nuclear electronics might be the same. That is why the majority of the laboratories applies both methods alternatively or simultaneously.

In the first part of this book (Section 3) the majority of the problems connected with instrumentation for nuclear analysis have been reviewed from the point of view of PIXE. While most of the conclusions presented there also hold for RBS, the problems will be presented here again with special emphasis on RBS related points. For example, hydrocarbon deposition on the investigated specimen is a fundamental problem in RBS, while this effect in PIXE is less pronounced. On the other hand, while vibration might destroy the performance of PIXE detectors, its effect in RBS is almost negligible. As a result, while a similar vacuum system is needed in both cases, their specifications might be quite different.

Before dealing with the technical details of instrumentation for RBS, let us summarise briefly the method itself. RBS differs from PIXE in the kind of radiation detected. Instead of characteristic X rays, those incident ions of M_1 mass and Z_1 atomic numbers are detected, that scatter back elastically from the target nuclei (M_2, Z_2). Due to the conservation of momentum and energy, the energy of scattered ions, E, is unambiguously determined by M_2 (for defined scattering angle), i.e. the energy distribution of scattered ions (energy spectrum) describes the elemental composition of the investigated target specimen:

$$E = E_0 k, \quad \text{where} \quad k = \left[\frac{\sqrt{M_2^2 - M_1^2 \sin^2 \Theta} + M_1 \cos \Theta}{M_1 + M_2} \right]^2 \tag{12}$$

Here k, the *kinematic factor,* characterises the target atom; E_0 is the energy of the incident ions and θ is the scattering angle. For RBS the energy and type of the incident ions are chosen in such a way that their scattering from the target atoms will be predominantly pure *coulomb scattering* (e.g. 0.5–5 MeV He ions). In this case the scattering probability (*cross section)*, $\sigma(E_1,M_1,M_2,Z_1,Z_2,\Theta)$, can be calculated from basic principles using the Rutherford formula [65, 66]. Therefore, without applying any calibration standards, the area, A, of the various peaks in the energy spectrum gives the areal density, Nt, of the various elements in absolute sense:

$$(Nt) = \frac{A \sin \gamma}{Q \eta \Omega \sigma} \tag{13}$$

where γ is the incident angle of the ions, Q is their number while Ω and η are the solid angle and the efficiency of the applied detector, respectively.

The above simple picture holds only for infinitesimally thin target foils. For thicker samples those ions that scatter back from atoms buried in the sample at various depths, x, loose some energy along both their inward and outward trajectories. Consequently, the peaks characterising the different elements of a buried layer in the sample will shift towards lower energies. For moderate energy losses the relation between this energy shift and the depth is

$$\Delta E = \left[\frac{k S_{in}}{\sin \gamma} + \frac{S_{out}}{\sin \delta} \right] x \tag{14}$$

where δ is the exit angle of the ions. The S_{in} inward and S_{out} outward *stopping powers* depend on the type of ions, on their energy along their inward and outward paths and on the composition and atomic density of the investigated sample. The distorted shape of the peaks describes the depth distribution of

the various elements. Obviously, by allowing determination of the depth profiles of almost all elements present in a sample from a single measurement, RBS is a rather versatile analytical tool.

Ions traversing along major crystal axes or planes of single crystalline samples might penetrate deep in the sample without suffering close interaction with the nuclei of the sample atoms positioned in atomic rows or planes [68, 69]. This so called "*channelling effect*" is caused by those repulsive electrostatic forces that arise between the positively charged atomic nuclei of ions and sample atoms and steer the ions between the atomic rows or planes in a crystalline sample. Combination of channelling effect with RBS (or PIXE), hence gives information on such details as crystalline quality of the sample and lattice location of various impurity atoms. Depth distributions of the above properties can also be obtained by RBS.

For valuable measurements, from which quantitative information might be obtained with reasonable precision, all the so far mentioned parameters have to be precisely known or defined by the experimental setup.

To perform RBS analysis, typically the following instrumentation is necessary. An instrument that generates the suitable energetic *ions;* a *beam line* that shapes the ions into a well-defined beam and directs it onto the sample, which is positioned in *a target chamber*. There a *detector* together with the necessary *electronics* observes the energy distribution of the backscattered ions that is then handled and evaluated by a suitable *computer* (see Fig. 25).

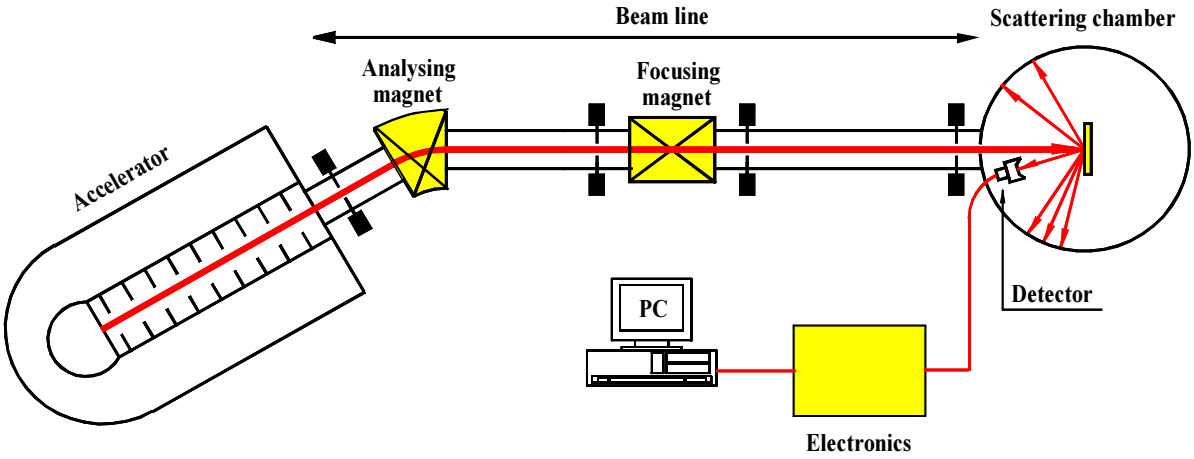

FIG. 25. Schematic overview of the RBS set-up. Energetic ions are generated by the accelerator and directed to the sample by the beam line. The scattered ions are detected by the detector, which signal is evaluated by the electronics and the PC.

4.2. INCIDENT IONS

Ions in a typical case are produced by a Van de Graaff type accelerator of a few MeV energy and of ~10^{-4} energy resolution, but other accelerator types might also be suitable (see Section 1). The accelerated ions in most cases are $^{4}He^{+}$ but, because of their better mass and depth resolution and detection limit for heavy elements, heavier ions (e.g. $^{14}N^{+}$) might also be useful [70] (see Fig. 26). These advantages frequently are completely overwhelmed, however, by the much faster sample deterioration (sputtering, ion beam mixing, lattice damage, etc.) and by the weaker performance of the widespread applied solid state detectors [71] for heavier ions as for light ones [72–74]. Application of $^{1}H^{+}$ ions in some cases is also beneficial, because one can detect by this way also the light elements down to M_2=2AMU with much better sensitivity than by using He ions. This is so because the cross section of proton backscattering from light elements is several times (3–300 times) higher than the Rutherford values. Sometimes however, these advantages are counterbalanced by less accurately known cross section values and weaker element separation for heavier elements.

According to the above arguments, it is practical to apply a flexible accelerator capable to produce ions of various kinds and energies and switch easily between them. In some cases, e.g. planetary [75, 76] or geological research, instead of accelerators a radioactive α source is used.

The beam line directs the ions to the sample. Generally, the beam line consists of a long vacuum tube (drift tube) of typically 10^{-4} Pa pressure equipped with the various beam handling elements, as follows.

Diaphragms define the position, shape and size of the incident ion beam (typically $\sim 1 \times 1$ mm^2). For channelling experiments two diaphragms are mounted at least at 1m from each other, because the angular divergence of the beam has to be limited below 0.1°. The necessary direction and position of the beam can be ensured by *beam steering elements* (small electromagnets or electrostatic deflector plates). Magnetic *quadrupole lenses* focus the beam to reach high intensity at a given beam size (typically a few tens of nA is necessary for RBS). By *microprobes* (a precisely built set of diaphragms and quadrupole lenses [77–83]) it is possible to reach μm or sub μm sized beams at a reasonable beam intensity (~0.1 nA). Scanning this beam over the sample one can map the lateral distribution of the different features (elemental composition, crystal quality, etc.). In contrast to PIXE, diffuser foils (see Section 2.2.2.) are not practical for RBS, because they enhance the energy spread and angular divergence of the incident ions through energy straggling and multiple scattering, respectively.

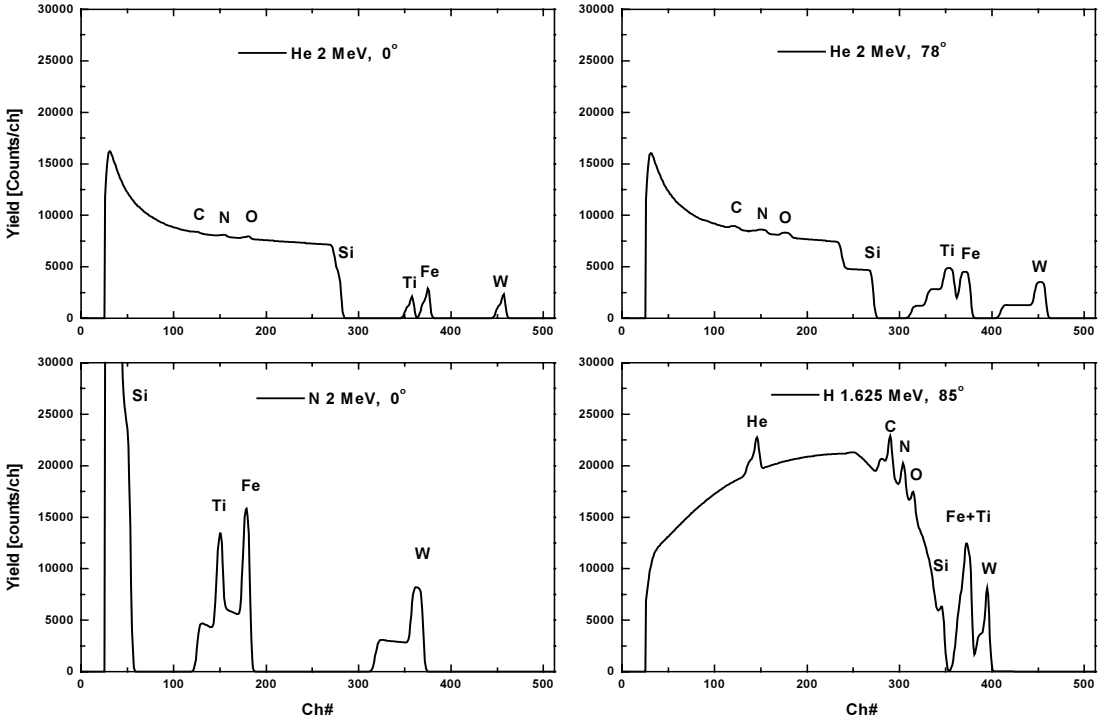

FIG. 26. Typical RBS spectra of a bilayer structure (1.3 × 0^{17} atoms/cm^2 of $He_1C_1N_1O_1Ti_1Fe_1W_1$ and 3.2 × 10^{17} atoms/cm^2 of $He_1C_1N_1O_1Ti_1Fe_1W_1Si_{10}$) on Si substrate. The spectra are simulated by the RBX code (see Section 3.4) using the indicated incident ions, energy and sample tilt angles. When necessary, the actual non-Rutherford cross sections for various elements were taken into account, as well. (Ω = 2.5 msr, Q = 40μC ≈ 2.4 × 10^{14} ions).

To perform absolute RBS measurements, one has to know precisely the number of incident ions (Q in Eq. 13). This typically is determined by integrating the electric charge carried by the ions [84, 85]. This information is much more important in RBS than in PIXE, because in some cases light elements do not contribute significantly by counts to the spectra, they are seen only through their energy stopping. In these cases the yield of the thick samples decreases, which effect might be easily

misinterpreted as a result of a smaller number of incident ions. In case of reliable determination of the measuring dose, the decreased yield unambiguously indicates the presence of light elements and calls the attention of the experimentalist to repeat the measurement under conditions more sensitive for the light elements, e.g. p-RBS (RBS performed by protons, see Fig. 26) or ERDA (Elastic Recoil Detection Analysis, i.e. observation of target atoms that are expelled from the sample when the incident ions scatter back elastically from them [86, 87]).

The *beam current* can be measured directly at the sample or by a beam chopper that periodically intersects the beam [84, 85]. In both cases, it is crucial to suppress the false current carried by secondary electrons or ions scattered from the edge of various diaphragms determining the shape and size of the beam. For this purpose, it is useful to mount behind the last beam-forming diaphragm an additional diaphragm that has a larger opening than the beam size and is raised at a few hundred Volts negative potential. This diaphragm will force back the majority of the secondary electrons and catch the scattered ions, as well (*anti-scattering diaphragm*). Secondary electrons emitted from the sample or the beam chopper also might effect the current measurement. This problem can be solved either by applying the Faraday-cup principle, or by surrounding the sample by suppressor plates/grids. In the case of a Faraday-cup the sample or the beam chopper is surrounded as completely as possible by a cage, which is connected electrically to it and collects the majority of the secondary electrons. To force back the secondary electrons to their origin, suppressor plates/grids are raised usually to ~ −100V.

In some cases, e.g. movable detectors or detectors of large solid angle, a suppressor plate or a Faraday-cage around the sample would be disadvantageous, because they would seriously disturb the measurements. In such cases, the whole target chamber might be used as a Faraday-cage or a suppressor. The former solution cannot be easily applied for small beam currents (<10 nA), because the large unshielded chamber picks up a high level of noise. Concerning the second solution, it is not advisable to apply high voltage at the chamber, because it is dangerous (accidental electrical shocks) and it might be problematic to isolate all the accessories from the chamber. It is better to put the sample at a few hundred Volts *positive* potential instead (e.g. by introducing a group of batteries between the charge integrator and the sample).

Especially in the case of heavy ions, charge exchange (electron loss or uptake) of ions also might lead to incorrect determination of the number of incident particles. Therefore, charge exchange must be kept as low as possible. As an alternative solution, in some cases the number of the incident particles is determined by the intensity of the ions backscattered from a reference sample or a beam chopper.

The number of the incident ions is determined with a typical precision of ~5–10%. With special precautions ~1% precision also might be reached [84].

Applying the above instrumentation one can ensure that the selected part of the sample will be bombarded with a well-determined ion beam. In the following we will describe in more detail, how the sample is mounted in a target chamber, what kind of detectors can observe the energy distribution of the backscattered particles and how this information is acquired and evaluated.

4.3. TARGET CHAMBERS AND ASSOCIATED EQUIPMENT

The measurement itself is performed in a so-called *target chamber*. It is connected to the accelerator through the *beam line* and consists of the following parts. A *vacuum vessel* that is evacuated by a *vacuum system*; a *sample holder* that holds and moves the sample(s) in a suitable way; and *detectors* mounted to suitable *detector holders*, that observe the backscattered particles.

Several laboratories design (or have designed) their own target chamber(s) and built it from purchased and/or home manufactured components. For routine measurements complete target chambers with full automation are also available [88].

4.3.1. Vacuum system

To avoid the interaction of incident or emitted ions with gas atoms in the target chamber, the *vacuum* there must be at least in the range of 10^{-3} Pa. A typical vacuum is ~ 1×10^{-4} Pa. An effortlessly readable description of definitions and equipment connected to vacuum production and measurement can be found in Ref. [89]. For a more comprehensive study see Ref. [90].

Unfortunately, *hydrocarbon molecules* from the vacuum ambient continuously deposit to the sample surface. There, being excited by the incident ions at the beam spot, they decompose into chemically reactive fragments. These fragments form new chemical bonds resulting in a non-volatile polymer layer on the surface [91–93]. This layer might substantially disturb the RBS measurements, e.g. by shifting down all the characteristic energies as both the incident and backscattered ions loose energy when crossing it. Hydrocarbon build up might be checked by repeating RBS measurements several times at the same spot. To avoid this problem, *the hydrocarbon content of the residual gas in the target chamber has to be as little as possible*. If possible, oil diffusion pumps with or without baffles cooled by liquid nitrogen (LN_2) should be avoided, because in the case of failures or mistaken use they can fatally contaminate all the system. Ion getter pumps or liquid He cooled cryopumps are better, but their pumping speed for He is low. The most commonly used solution is evacuation by turbomolecular pumps ("turbo pump") backed by oil filled rotary vane roughing pumps [89]. There are several companies selling vacuum components, [e.g. 94–101]; turbo pumps are available, e.g. from [94–99].

Unfortunately, even the turbo pump cannot guarantee a completely oil free solution. There is always a weak oil back-flow from the backing pump and from the oil lubricated ball bearings of the turbo pump. Furthermore, when the turbo pump is stopped the oil vapour can freely pass through it. Therefore, it is advisable to run the pump continuously and change the samples through a load-lock system.

It is also recommended to use oil traps at certain places. Large LN_2 cooled surfaces in the target chamber might reduce the hydrocarbon build up by a factor of 10 or more. A similar trap mounted in the beam line right in front of the chamber reduces the oil vapour flow from the accelerator. It is also recommended to mount foreline oil traps between the backing pumps and the turbo pumps. Several solutions (e.g. zeolite filled traps, Peltier element or LN_2 cooled traps, ceramic micromaze traps) are offered by the various vacuum companies [94–101].

If the turbo pump is hybrid type (a few turbine stages at the exhaust-side are replaced by a special spiral) [94–98], a moderate backing vacuum of ~100–1000 Pa is enough. In this case a relatively cheap diaphragm pump can serve as backing pump (their principle is similar to those used to ventilate hobby aquariums) [94–96]. In this case the oil contamination from the backing pump is completely eliminated, but the turbo pump still might be an oil source. The best (and most expensive) solution is to built a modern, oil free ("dry") vacuum system. This consists of a lubricant free (e.g. magnetically levitated) turbo pump [e.g. 94, 95, 97, 99]) backed by an oil free backing pump (e.g. a dry VRC [96] or a scroll pump [95–97]). By choosing this solution, one can use the roughing pump as an ideal unit to perform oil free evacuation of the load-lock chamber, as well.

If one wants a really oil free setup, it is recommended to built all the system oil free, including the accelerator and the beam line, as well. If this is not possible, as a minimum requirement, a vacuum isolating element has to be introduced into the beam line. This means a differentially pumped and/or LN_2 trapped tube section, which is connected to both the accelerator and target chamber through vacuum chokes (narrow tubes or diaphragms).

In some cases, e.g. microprobes or if supplementary analytical methods of high lateral resolution (e.g. atomic force microscope) or vibration sensitive PIXE detectors are also incorporated in the target chamber, the *vibration* of the turbo pump might be a serious problem. In such cases, the turbo pump has to be fastened to a separate platform and connected to the target chamber through a soft flexible bellow. However, a vibration free pump, e.g. an ion getter type one, might be the best solution.

4.3.2. Target chamber

The size and shape of target chambers typically varies between 1 and 100 dm^3 and they are completed by several flanges and feedthroughs as follows.

Through a large *viewing port* one can observe the chamber interior *(optional)*.

The samples might be changed through the viewing port (if it is large enough) or simply by removing the whole sample manipulator from the chamber. In the case of UHV systems for both solutions, it might be worth considering to use at these flanges viton gaskets instead of copper seals.

A dedicated *load-lock system (optional)*, however, can be more useful, because through it the samples might be changed quickly without breaking the vacuum in the main target chamber. A typical load-lock operates as follows. The samples are mounted first in the load-lock chamber in a rack which is fastened to a long transfer rod. The load-lock chamber is then evacuated by its own vacuum system and the transfer rod introduces the rack through a gate valve into the target chamber, where a catcher fastened to the sample holder receives it. Then the rod is removed and the gate valve is closed. To remove the samples, the above procedure has to be reversed. One has to select the pumping system of the load-lock chamber with especial care. For example, if one uses here an oil filled rotary vane pump, it might introduce into the target chamber more oil contamination than the main pumping system would do it alone. Therefore, at least a foreline oil trap has also to be added or an oil free roughing pump has to be applied. For ultra high vacuum (UHV) target chambers the load lock chamber is a must (except if one wants to subject the same sample to various in situ modifications and investigations for several days or weeks). For faster UHV recovery, the load-lock chamber might be evacuated also by a turbo pump.

Incident ions detailed in Section 4.2. enter the target chamber through the *entrance flange*. Inside or near this flange the following elements can be mounted (see Fig. 27).

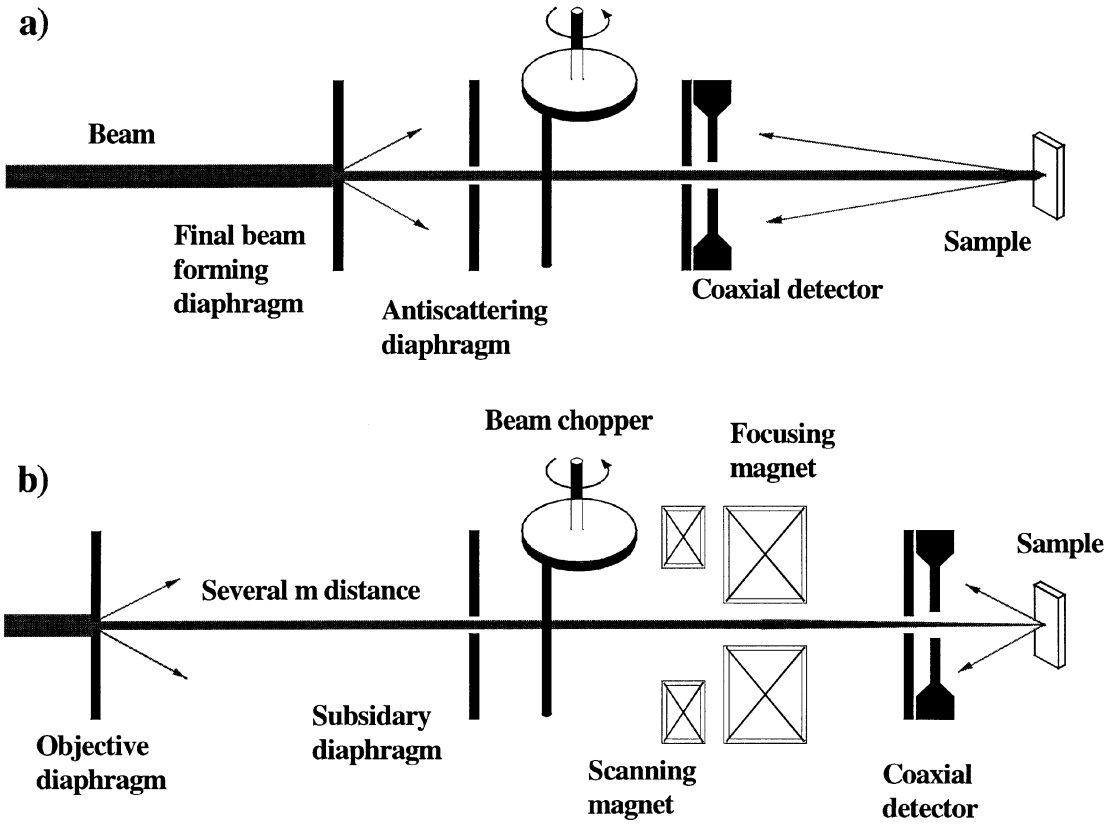

FIG. 27. Elements frequently mounted at the beam entrance of the target chamber: a) ordinary set-up; b) microprobe.

(1) The *final beam forming diaphragm* determines the position and shape of the beam spot on the sample. To minimise the number of ions suffering small angle scattering at the edge of this diaphragm it has to be manufactured carefully. Its edges have to be smoothed and rounded (elaborated edge profiles are discussed in refs. [102–104]). During long term usage (years), because of hydrocarbon deposition and/or flaking, the quality of this diaphragm might deteriorate, hence it has to be regularly inspected and, if necessary, repaired or replaced. The beam shape determined by this diaphragm might be circular, but it is more practical if it is rectangular and is determined by four independently movable edges. In this case, both its shape and size can be easily varied. The diameter of the beam is typically ~1 mm. For small samples or tiny features on the sample even smaller diameters also might be necessary. By careful preparation of the final diaphragm a beam diameter of ~0.2 mm is still achievable without increasing the level of ions scattered from the diaphragm to an unreasonable extent. Even smaller beams can be achieved only by microbeam systems (Fig. 27b) [77–83].

(2) To investigate radiation sensitive samples or to perform measurements at high beam currents a large beam diameter, e.g. 4 mm, might also be necessary. Even larger beam diameters are not practical, because the scattering angle of ions would change significantly over the beam spot resulting in intolerable deterioration in the quality of the measured energy spectra. It is frequently necessary to change the shape or size of the beam between various measurements. If the beam forming diaphragm is not constructed from independently movable edges, this might be solved by mounting various diaphragms on a long bar fastened to a linear motion feedthrough, or on a polygonal prism held by a rotary motion feedthrough.

(3) For beam intensity determination towards the sample the last beam forming diaphragm might be followed by a *beam chopper or a transmission Faraday-cup (optional).*

(4) *Antiscattering diaphragms (optional)* might stop those ions that, in spite of careful edge preparation, suffered small angle scattering at the edge of the final beam forming diaphragm. Their openings have to be slightly larger than the beam size, in order to avoid further cutting and scattering of the measuring beam.

(5) Finally, an *annular detector (optional)* can also be mounted directly facing the sample. The beam passes through the central opening of this detector and ions backscattered from the sample can be detected at a scattering angle very close to 180° and/or with a large solid angle. In the latter case the main advantage of such detectors is, that the scattering angle changes relatively little along the sensitive area of the detector and so the quality of the spectra deteriorates as little as possible. It is worth noting, however, that in this case, if the sample is tilted into a large angle, due to the variation in the glancing exit angle, δ, spectrum details corresponding to deeper regions in the sample will be smeared out.

If the final beam forming slit is far from the sample, due to the angular divergence of the beam the beam spot smears out on the sample. In some cases, for example when performing measurements at grazing incident angle where the beam spot on the sample expands several times in one direction, this problem has to be minimised. Therefore, the beam forming slit has to be as close to the sample as possible. The same holds for the quadruple magnets of the microprobe, otherwise it would be impossible to achieve the necessary magnification factor when projecting the objective slit onto the sample. Therefore, all the above components have to be as compact as possible.

Another flange of the target chamber is equipped with the *sample holder* (manipulator). This unit might be of various constructions again. In the following we will briefly discuss a few typical solutions.

Some sample holders can hold a *single sample* only. In such cases, it is useful to install the target chamber with a load-lock system, so that the sample might be changed without breaking the vacuum. It is frequently necessary, however, to measure the sample at a few different spots (e.g. to find various parts of the sample or just to move the beam to a fresh spot). In these “single-sample” manipulators this movement is frequently done by using the following technique: The vacuum flange through which the manipulator is introduced is fastened to the target chamber through a flexible bellows.

Three dimensional (3D) positioning of the flange is placed outside the vacuum by micrometer screws driven either manually or by the stepping motors (*3D bellows type positioning*, see Fig. 28).

It is less complicated if the sample is fastened to a linear motion feedthrough. In this case only *1D movement* is achievable, however. If the feedthrough allows the movement for a longer distance, the same sample holder can accommodate several samples.

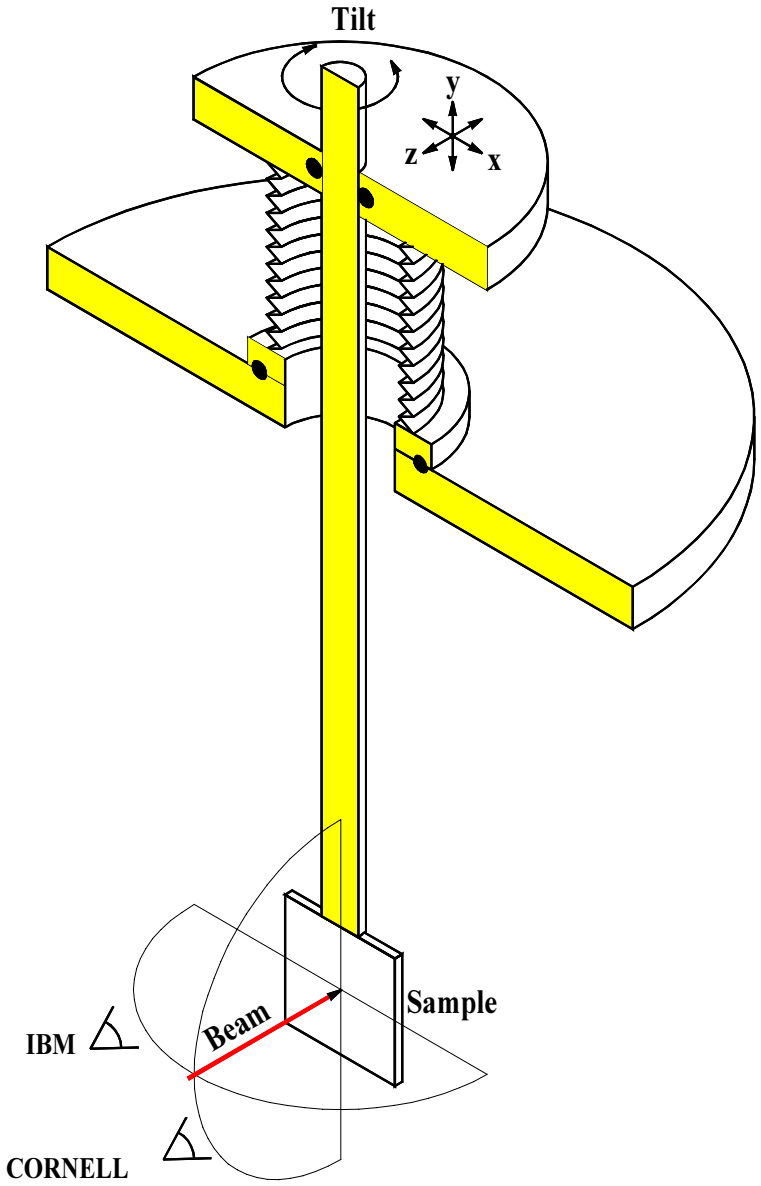

FIG.28. Bellows type sample positioning system. The whole sample holder is fastened to the target chamber through a bellows and it can be moved from outside the vacuum through precise positioning of the movable flange. Problem: If the surface of the sample and the beam does not intercept on the tilt axis, when the tilt is changed the beam spot on the sample moves. Special detector positions are also indicated. CORNELL geometry: the detector is in the plane containing the tilt axis and the beam direction. IBM geometry: the detector is mounted in the plane which contains the beam line and is perpendicular to the tilt axis.

In some cases it is impossible to reconstruct the depth distribution of all elements present in a sample from a single measurement, hence one would have to change the energy or type of the incident ions. This, however, would be a rather time consuming process. It is easier to change the incident

angle, γ, by tilting the sample, instead. This solution has a further advantage: if the beam hits the sample at a grazing incident angle (i.e. the tilt angle is large), for the near-surface regions the depth resolution and the sensitivity of the measurement significantly improves (approximately by a factor of 10). Therefore, it is very useful if the sample can be tilted around a *tilt axis* without breaking the vacuum. This task is easily reachable if the sample holder is fastened to a rotary motion feedthrough. In some cases the sample can be tilted even by 180°, so that its back side is also available for the measurement.

Of course, combination of tilting possibility with the 3D bellows type positioning system or with the 1D movement will considerably increase the effectiveness of the set-up.

To ensure the bombardment of the sample along any selected crystallographic direction during channelling measurements, the sample has to be rotatable precisely around at least two independent axes (see Fig. 29). To reach this goal, besides the above mentioned tilt axis the sample has to be tiltable around a second tilt axis (Fig. 29a) or to be rotatable around an azimuth axis (Fig. 29b). Either additional axis should intercept the first tilt axis perpendicularly. Such sample manipulators are called *two axis goniometers*. In the case of tilt-azimuth type goniometers it is crucial to ensure by fine adjustments of the manipulator a precise coincidence between the azimuth axis and the beam at tilt 0°. For such purposes the so called *three axis goniometers* are equipped with an auxiliary tilt, as well (Fig. 29c).

For all kinds of goniometers the beam spot has to remain at the same position at any tilt or azimuth angles, i.e. all the axes should intercept each others in the point where the beam hits the surface of the sample. For this goal, the goniometer has to be precisely built and the beam position as well as the elevation of the sample surface from the sample holder should be adjustable. Alternatively, if the beam is fixed, the goniometer has to be adjustable instead, e.g. through the already mentioned bellows type positioning system. This latter solution, however is not ideal, because the beam spot will stand fixed only for one single point of the sample. For other positions, all the tilt and rotation actions should be counterbalanced by appropriate movements of the manipulator. This, of course, is uncomfortable, but in this case the setup remains relatively simple and it can be built with the desired precision more easily.

Single-sample type manipulators are frequently heatable (e.g. up to 900°C) and/or coolable by liquid N_2 or He. The samples have to be cooled, e.g. to investigate the ion irradiation induced effects (lattice damage, etc.) at low temperatures where no dynamic annealing occurs, or to analyse radiation sensitive samples (e.g. polymers or biological dissections). The heating possibility might be useful for various tasks, e.g. in situ investigation of solid-phase intermetallic reactions or the recovery of lattice damage. Cleaning the sample surface by evaporating contaminants or the oxide layer is also an indispensable capability of heatable sample holders.

Some sample manipulators are built to measure *multiple samples,* each of them at various spots if necessary. If no goniometer is required, the most simple solution is when the sample holder is movable in one direction at large distances (typically a few centimetres), e.g. through the positioning bellows or a linear motion feedthrough. If there is one single tilt axis, the linear movement should be done parallel to it, i.e. the linear motion feedthrough should be also rotatable or, in the case of bellow type positioning, a rotary feedthrough should be fastened into the centre of the positionable flange. In the case of the latter solution, tilting actions might have to be counterbalanced as was already mentioned in connection with goniometers.

In multiple-sample goniometers, the samples are fastened to a plate that can be moved relative to the “interception point” of the goniometer axes and the beam (Fig. 30). It is rather difficult and complicated to construct a mechanism that ensures this movement by rotary or linear motion feedthroughs that are connected permanently to the sample holder. As an alternative solution, the sample holder plate can be moved by an additional manipulator, typically a rotatable and extractable stick. At a special position of the goniometer one can connect this stick temporarily to a special handle of the sample holder then by rotating it the sample holder plate can be transferred into the wanted position. Since this solution is inconvenient and cannot be controlled by a computer, it is more

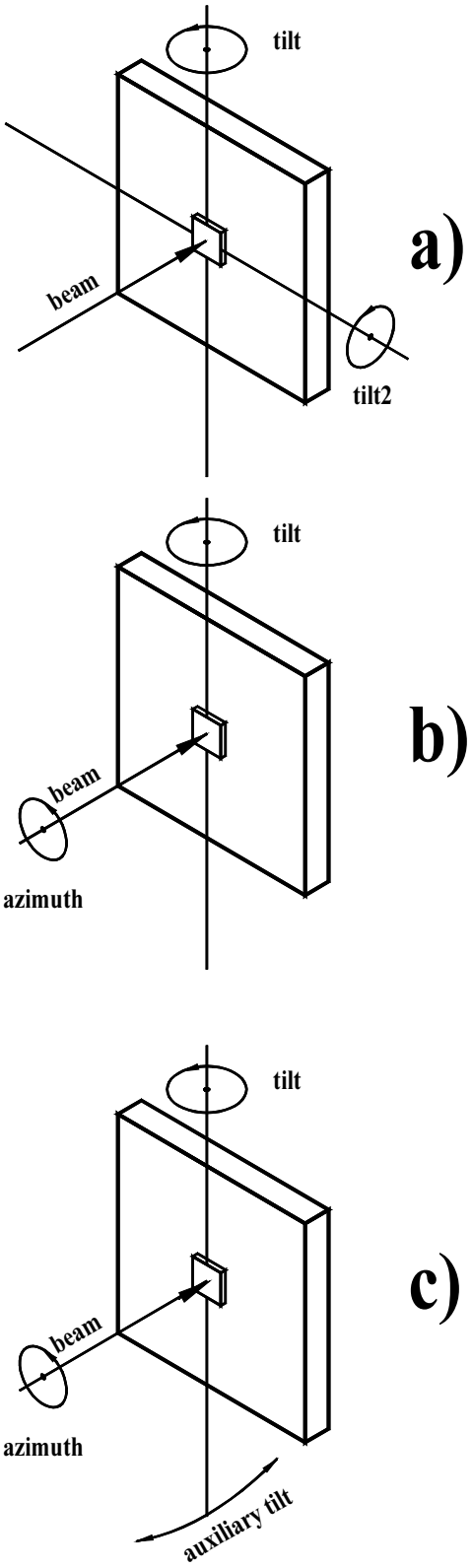

FIG. 29. Goniometer types: a) two tilt axes; b) tilt and azimuth axes; c) 3 axis goniometer (the azimuth axis is adjustable to the beam using an auxiliary tilt).

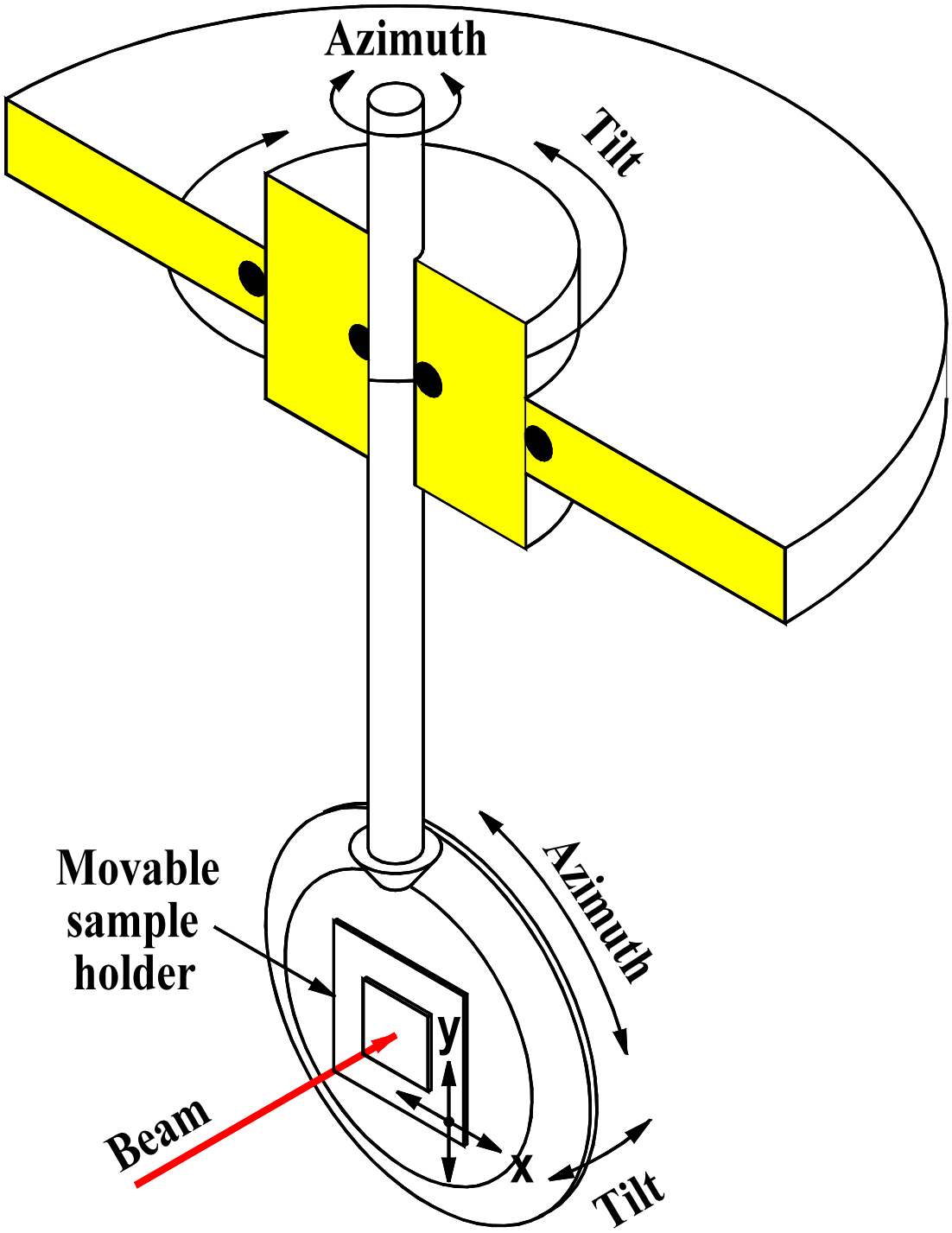

FIG. 30. Multiple-sample goniometer. The sample holder plate can be translated independently of the goniometer. By this solution orientation of the sample can be performed at a fixed beam spot on the sample and vice versa, the sample can be moved without changing its crystallographic orientation.

practical, if the sample holder plate is moved by stepping motors that are fastened to the goniometer. These motors are driven by flexible cables of vacuum compatible type, hence they can be operated at any position of the goniometer. In most cases commercial stepping motors do not influence much the high vacuum. Special UHV compatible stepping motors are also available (e.g. from Caburn MDC [100]).

A universal sample manipulator, e.g. a heatable-coolable multi-sample goniometer where the samples are changed through a load-lock, would be too complicated and vulnerable to failures, hence one has to choose which functions are really necessary. It is more practical to build target chambers of different abilities. For example, for delicate research a good solution might be a UHV goniometer, where the single sample can be heated, cooled and changed through a load-lock system. For routine measurements another chamber, where several samples can be loaded to a large plate and measured automatically by a controlling computer might serve better.

The samples have to be fastened to the sample holder. The solution, of course, can be various again. In the case of heatable and/or coolable sample holders in most cases only samples of special shape and size can be fixed on (e.g. disks of special diameter and thickness), because they have to be fastened to the sample holder with a good heat contact, e.g. by pressing them around their perimeter. For routine measurements, a more versatile solution has to be chosen. The samples can be glued on, e.g. by conductive vacuum pastes, or by sticking papers. These solutions might be problematic, because the glues or papers emit organic vapours that spoil the vacuum near the beam spot resulting in accelerated hydrocarbon deposition. The best solution is to press the samples to the sample holder by springy claws or paws. They can fasten samples of various shape without contamination problems. Unfortunately, they protrude from the sample holder higher than the sample itself, hence in the case of grazing incidence or exit angles they might cast unwanted shadows on the samples. This problem can be avoided, if the applied springs are flat enough and/or the geometry of the measurements is chosen carefully, i.e. the incident beam and the detector are seen from the beam spot in such directions that are far from the claws.

When measuring insulating samples the following problems might arise. The sample repeatedly charges up to a large positive voltage, e.g. several kilovolts, resulting in a shift in the energy spectrum (the emitted ions are accelerated by the voltage), then discharges towards the sample holder. The intensive ultraviolet light accompanying these discharges increases the noise in the measured spectra and might damage the applied solid state particle detectors (see below). The discharges have to be suppressed by an electron source (e.g. a simple electron gun [40]) that floods the sample by low energy electrons and keeps it close to the ground potential. In this case it might be problematic to measure the beam current on the sample with a reasonable precision (i.e. <5%), hence it is better to use a beam chopper instead.

4.4. DETECTORS AND RELATED COMPONENTS

4.4.1. Detectors

Applying the above detailed instruments, we can ensure that a well controlled ion beam bombards the chosen spot of the sample. Now, we have to select the direction and solid angle where the backscattered ions are detected and determine their energy distribution by a suitable detector.

The main task of the detector, therefore, is to determine the energy of the detected ion. It is rather difficult to measure this quantity directly, because it is just a few fJ (femto Joule), but not impossible. Detectors measuring the heat deposited by single particles (*bolometric detectors*) are under development.

It is easier to measure the energy through the ionisation of the particle in a suitable medium, e.g. in a semiconductor material. Here the number of the generated electron-hole pairs, i.e. the amount of the mobile charge is proportional to the total energy loss of the particle in the sensitive volume of the detector. The proportionality factor is typically a few eV/pair (e.g. 3.62 eV/pair in Si at room temperature), or ~0.1 fC/keV. The mobile charge carriers can be collected by an electrostatic field developed between the collector electrodes of the detector. The collected charge is then processed by an electronic system that generates the energy distribution spectrum of the detected particles (see Section 3.3). In RBS practice these semiconductor particle detectors are the most commonly used, so we will discuss them in more detail.

Basic principles of semiconductor detectors are shortly introduced in the Section 3.3.2. and are treated in more detail in Ref. [71]. Typical semiconductor detectors for charged particle detection are made of slightly doped crystalline Si wafers of ρ = 500–2500 Ωcm resistivity. Front and back sides of typical detectors are contacted either by thin evaporated metal layers, ('surface barrier Si detectors', see Fig. 31), or are made through doping very thin layers by ion implantation (ion-implanted or PIPS — 'Passivated Implanted Planar Silicon' — detectors).

These detectors, in principle, serve as diodes that are reverse-biased for suitable operation, i.e. to build up a thick enough depleted layer at their front sides from which the free charge carriers created by the incident particles can be effectively extracted and collected. The thickness of the depleted (i.e. sensitive) layer, D depends on the applied voltage U,

$$D = \sqrt{2\varepsilon_0 \varepsilon_r \mu_e \rho (U_0 + U)} \tag{15}$$

where ε_0 and ε_r are the absolute and relative dielectric constants and U_0 is the contact potential. In partially depleted detectors the thickness of the depleted layer is smaller than the physical thickness of the semiconductor wafer. Totally depleted detectors are made of thin Si wafers and they are sensitive through their whole thickness.

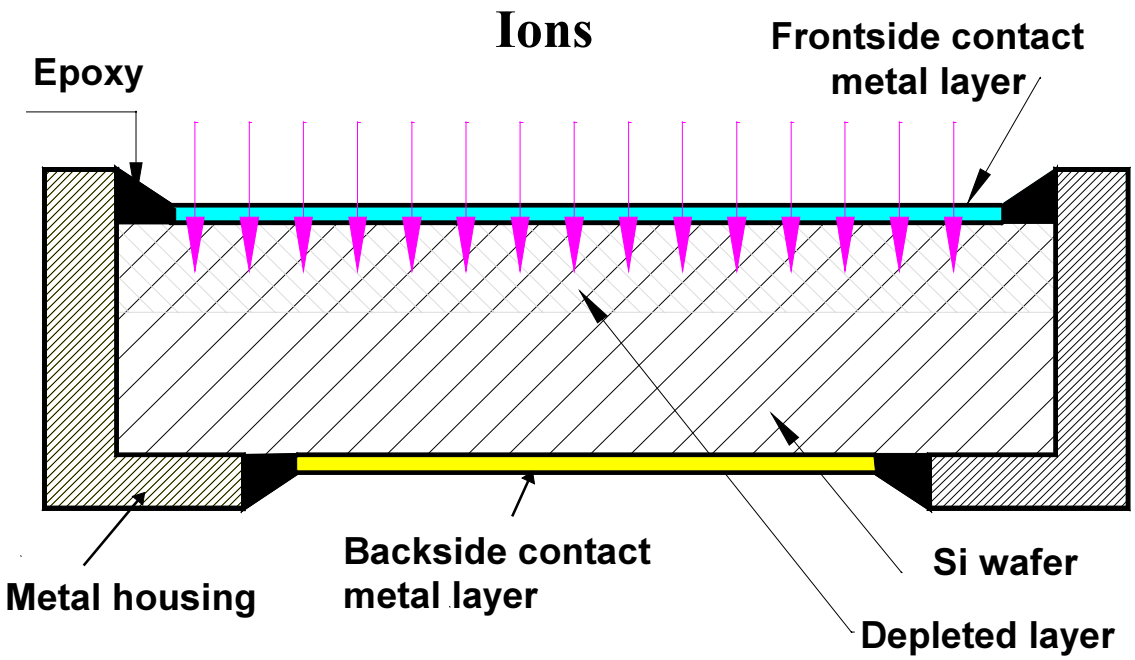

FIG. 31. Schematic drawing of a surface barrier detector. The Si wafer is fixed into a metal housing by epoxy glue, then contacted by two layers of different metals (e.g. Au and Al). Finally, the whole unit is completed with an electric junction (e.g. microdot or BNC). The thickness of the depleted region varies with the reverse bias applied on the metal contacts (Eq. 15).

The applied voltage has to be carefully chosen. If it is too small, the thickness of the depleted layer might be shorter than the range of the ions in the detector; furthermore, the energy resolution of the detector will be worse than at the ideal voltage (always given by the manufacturer). At too high voltages, because of electric breakdown, high current might flow through the detector, destroying it completely. The same might happen, if the sensitive surface of the detector is illuminated by intense light. Light emitted by insulating samples through ionoluminescence might also damage the detectors. In such cases so called 'blind' detectors (the surface of which is covered by a thin light tight metal layer) have to be used.

If the sensitive layer is thick enough to stop the particles completely, as it is the case in typical applications of partially depleted detectors, the collected charge represents the total energy of the incident ions. Otherwise, e.g. in totally depleted detectors, one can obtain only the average stopping power for the detected particles. Since at a given particle energy this quantity depends only on the atomic number of the particle, these detectors are frequently used for particle identification. (Such detectors might also give the START signal in time of flight (TOF) experiments).

The main advantage of modern PIPS detectors originates in their front contact. It is less sensitive to mechanical damage (e.g. can be cleaned by careful wiping) and is much thinner than the evaporated metal contacts, i.e. the incident ions lose less energy before entering the sensitive depleted layer. This means that, especially for low energy and/or heavy ions, the smallest detectable ion energy is lower and the energy resolution is improved.

Charged particle semiconductor detectors are available from a few companies, i.e. ORTEC [71], CANBERRA [106] or OXFORD [107].

Unfortunately, these relatively cheap and versatile detectors are not always suitable to detect the backscattered particles or to determine their energy distribution. For example, RBS measurements using low energy (<200 keV) or heavy particles are also performed, because of the restricted energy of the ion source (e.g. in the case of a focused ion beam equipment [108, 109]), or to reach improved sensitivity for heavy impurities [110, 111]. In these cases, in the dead layer at the front surface of the detector the backscattered ions would lose too high a portion of their original energy and/or suffer too high energy straggling, restricting the performance of the RBS method, or even prohibiting its application.

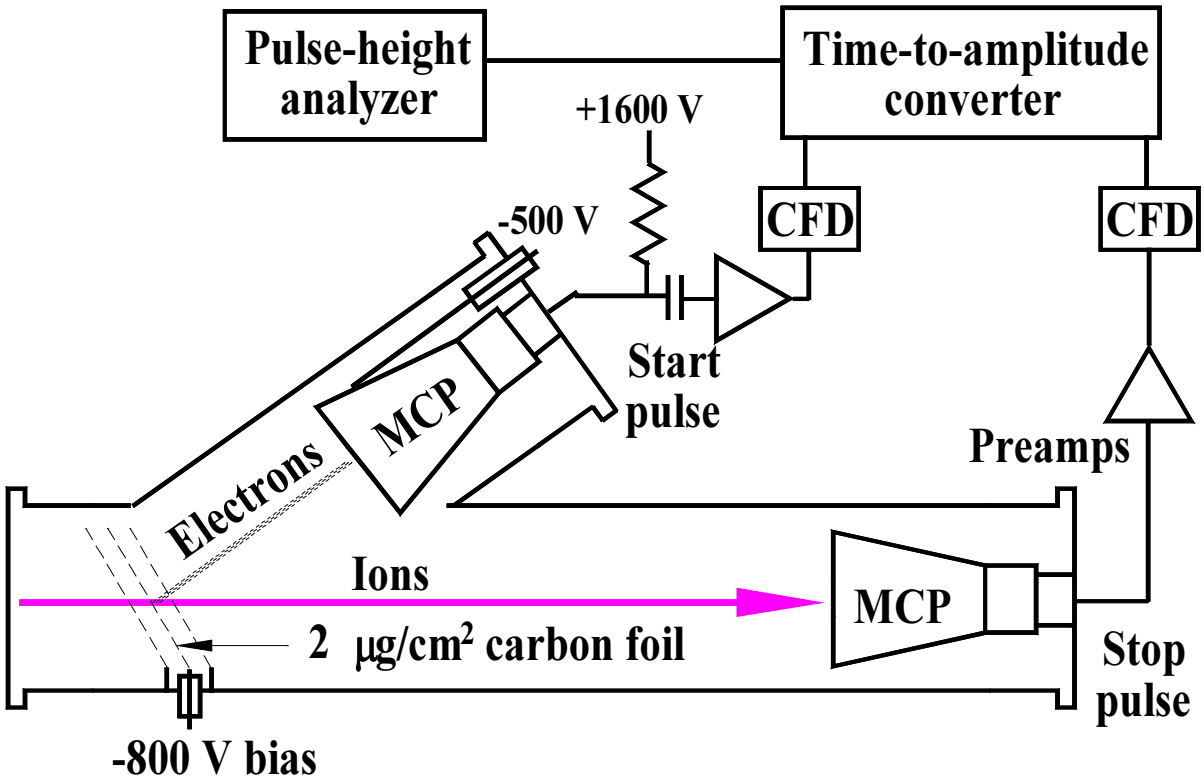

FIG. 32. A time of flight detector system (MCP — multi-channel-plate, CFD — constant-fraction-discriminator).

In these situations, another type, e.g. TOF detectors might be more useful [110, 111]. Here the energy of the ions is determined through their velocity via measuring the time they spend traversing a given distance. For this purpose the START signal might be generated in various ways, for example, via pulsing the beam of the accelerator (as is the case with cyclotrons), or applying a device which gives a signal when the ion passes through it. This unit might be a totally depleted detector or a proportional gas counter, but in the special case of low energy or heavy ions the best solution is a thin (1–5 $\mu g/cm^2$) carbon foil, from which the emitted secondary electrons are accelerated towards and detected by a multi-channel-plate (MCP). The detector giving the STOP signal might be a second MCP, or a solid state particle detector. The advantage of the first solution is its more precise timing characteristics and larger area, while using the second solution one might determine the velocity and the energy of the ions in two independent ways making it possible this way to distinguish between ions of different masses [112]. This feature is rather useful in the case of ERDA, because this way the scattered ions should not be stopped by an absorber foil that would degrade the energy resolution of the system and stop all the recoils heavier than the incident ion.

TOF detectors are reviewed e.g. in Ref. [113], while a typical solution applied mainly for medium energy ion scattering experiments can be found in refs. [114, 115] (see Fig. 32). Some considerations on choosing a suitable detector configuration for low energy RBS based on focused ion beams are presented in Ref. [116]. Typical examples on application of TOF detectors in high sensitivity RBS measurements based on low energy heavy ions are in Ref. [110, 111].

Especially good energy resolution can be achieved by magnetic spectrometers or electrostatic analysers. They are not suggested, however, for routine measurements, because their angle of acceptance is relatively low and they can measure just a very sharp energy interval at a time, so that the measurements can be rather time consuming. The above problems are partially circumvented in modern systems, e.g. in magnetic spectrometers using correction magnets and position sensitive detectors [117–119], or in toroidal electrostatic analysers with 2D position sensitive MCP-s [120]. From now on, if it is not otherwise stated, we will limit ourselves to solid state detectors.

4.4.2. Detector related components

The detector is fixed onto its position by a suitable *detector holder*. It might be fixed or movable. Fixed detector holders are generally used because of their simplicity, small size and precisely defined position. Large sized detectors (TOF, Magnetic spectrograph, etc.) generally are mounted in fixed position. Fixed solid state detectors are used to perform routine RBS measurements. Their results can be utilised as a reference, as well, if more than one detector is used simultaneously (e.g. RBS and ERDA measurements together).

It is suggested to mount a fixed solid state detector in CORNELL geometry (see Fig. 28) at $\Theta \sim 165°$ scattering angle. In this case, the spectra obtained at various sample tilt angles, α, are easy to compare: the distorted peaks representing depth profiles of various elements do not change in height, only their width (depth scale) stretches out according to $1/\cos(\alpha)$. The suggested scattering angle, 165°, is widely applied, so that cross sections for this angle are easy to find.

It might be useful to have a fixed detector in CORNELL geometry at $\Theta \sim 100°$, because in this case the damage depth profiles near the surface can be obtained through channelling measurements with a good depth resolution. Although the incident beam is nearly perpendicular to the surface in this case, i.e. $\gamma \sim 90°$, the exit angle δ is small (~10°). A detector in IBM geometry might do the job as well, but one has to be careful, because in this case the exit angle will change together with the tilt angle.

Movable detectors are applied in the following special cases. i) The detector has to be extracted from the UHV vacuum vessel during baking out. ii) If one wants to repeat the measurements at various scattering angles (e.g. to explore the angular variation of the cross section or to investigate the surface topography of the sample through performing RBS microprobe measurements at various glancing exit angles [121]). For movable detectors the IBM geometry is preferred (the mechanics of

the detector holder will not get jammed by the tilt axis). For large solid angle measurements of $\Theta \sim 180°$ scattering angle, a ring shaped solid state detector might surround the incident beam. This is necessary if one wants to deal with radiation sensitive samples (e.g. biological specimens, polymers, compound semiconductors or insulators).

If the sample is heated to high temperatures during or in between the measurements, heat resistant detectors have to be chosen, and they have to be cooled, e.g. by circulated water. If the sample emits light because its temperature is above 600°C, the detectors must be blind (see above) in the same time.

In most cases the scattering angle of the ions Θ, and the solid angle Ω, are defined simply by the sensitive area of the detector itself. In some cases, however, an entrance diaphragm is placed in front of the detector because of the following reasons: (i) to shadow the perimeter of the sensitive area of some detectors which do not work perfectly there (e.g. the response for the ion energy is different from that of the central region), (ii) to decrease the intensity of the detected ions through decreasing Ω, iii) to improve the mass end energy resolutions through decreasing the spread in Θ and/or in the exit angle of the detected ions, δ.

Commonly, a disturbing background arises due to those ions that suffer more than one scattering. Additionally to the basic scattering on the sample, other scattering events might happen not only in the sample but also at the last beam-defining slit or at the chamber wall. To minimise this background, it has to be ensured that only those ions reach the detector that are originated from the close vicinity of the beam spot on the sample. For this purpose, one can mount at a suitable distance from the detector an additional diaphragm that shields the detector from these unwanted ions. However, if this diaphragm is not precisely positioned, it might partially shadow the beam spot from the sensitive area of the detector, leading to incorrect determination of Ω. Furthermore, especially in the case of large sample holder plates, this diaphragm might hinder measurements at grazing incident angles. It is more advisable therefore, to solve the problem by antiscattering slits in the beam-line. Unfortunately, in this case the detector is not yet shielded from ions scattered first at the sample then at the chamber wall. These ions, however, would reach the detector mainly at a grazing angle, hence in most cases they will be shielded by the construction elements of the detector or the detector holder (see Fig. 33).

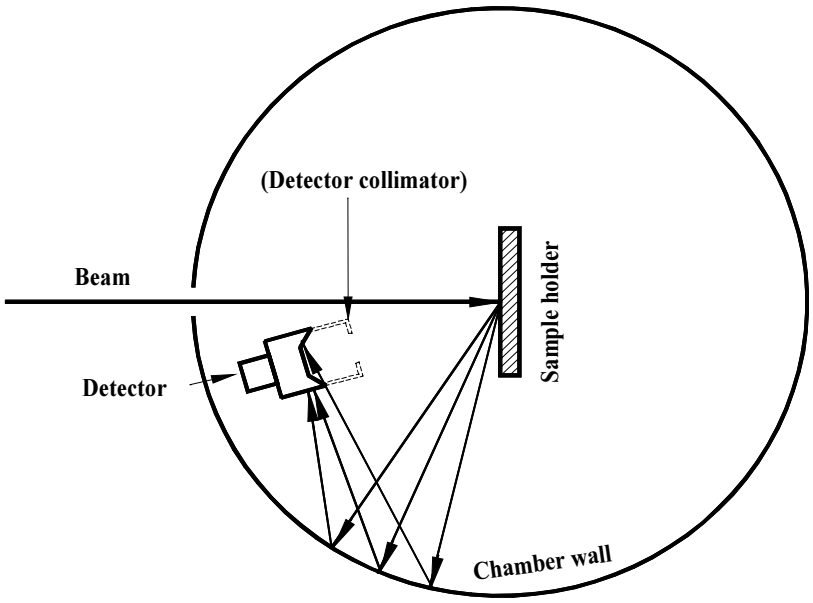

FIG. 33. Minimising the plural scattering. It is not always crucial to mount an antiscattering collimator in front of the detector, because the majority of the ions that scatter first at the sample then at the chamber wall are stopped by the construction elements of the detector or the detector holder.

The entrance diaphragm of the detector might be combined with an absorber foil that suppresses the background counts related to low energy and/or heavy ions. Typical applications are as follows. (i) elastic recoil detection analysis (ERDA), where the detector is mounted at a forward scattering angle and the scattered heavy ions are stopped by an absorber foil so that only the lighter recoil atoms can reach the detector. (ii) nuclear reaction analysis (NRA), in which case the scattered ions are stopped, and only the nuclear reaction product ions of higher energy and/or lower atomic number are detected. For typical RBS measurements no absorber foil is needed, it might be useful only if one wants to detect heavy impurity atoms on the surface of a light substrate with a high sensitivity. In this case ions scattered from the substrate with lower energy are stopped by the absorber, hence the beam current can be increased without overloading the detector and the electronics by too high counting rates. The high energy background caused by detection of two or more ions simultaneously (pile-up effect, see Sections 3.3.3.6 and 4.5.2) also will be eliminated in this case.

To minimise radiation damage to the detector during implantations followed by in situ RBS observation, a detector shutter might also be rather useful.

4.5. DATA ACQUISITION SYSTEMS

In RBS and ERDA analyses commercial nuclear instrumentation is used. These instruments were standardized by the United States Atomic Energy Commission. The basic concept is the nuclear instrument module (NIM) from which the standard gets its name. The best places to learn about fundamental elements of the nuclear electronics are the tutorial sections of the manufacturer's catalogues (e.g. ORTEC [71, 122], CANBERRA [106, 123]).

The principle of operation of the electronics setup is relatively simple as is diagrammed in Fig. 34. The solid state detector is connected to a preamplifier, which generates a pulse for each incident ion. The height of the pulse is proportional to the energy of the detected particle. This signal is further amplified and shaped by a spectroscopic amplifier and is digitized and displayed by a multichannel amplifier (MCA).

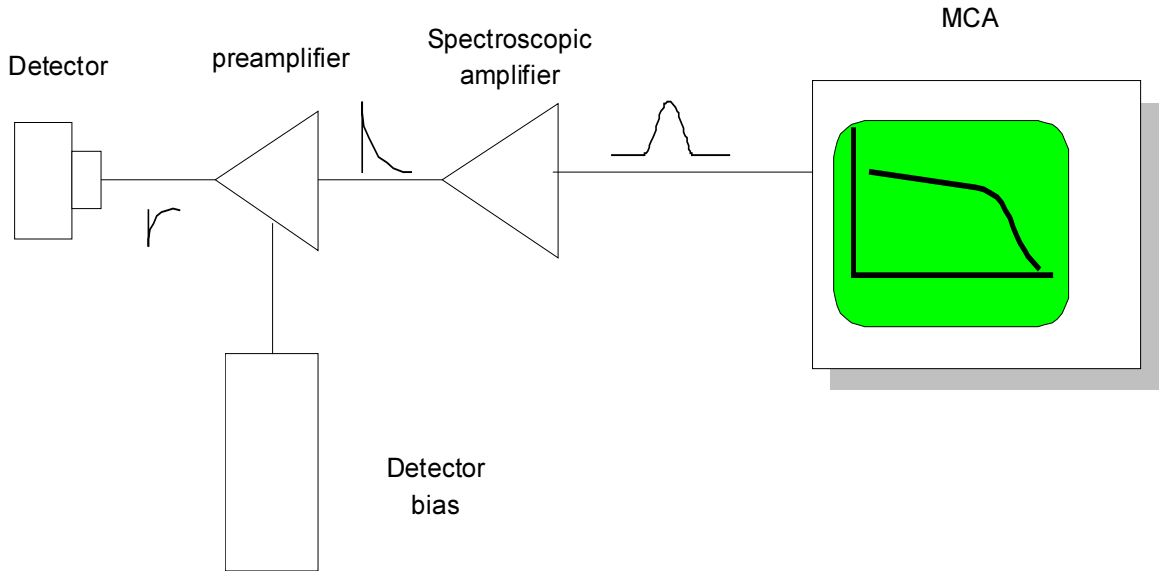

FIG.34. Basic electronics set-up for RBS measurements.

The voltage required to establish the reverse bias of the detector is supplied by a bias power supply, that is conventionally a separate module connected to the preamplifier. The power required for the operation of the preamplifier is supplied through a cable from the amplifier.

The preamplifier is usually a separate unit located as close as possible to the detector, but outside the vacuum chamber. To connect the detector to the preamplifier by minimising the capacitance and consequently the noise, a special shielded vacuum feed-through is built into the wall of the chamber. Preamplifiers for surface barrier detectors are not necessarily cooled.

Detailed descriptions of spectroscopic amplifiers and MCA are found in Sections 3.3.3 and 3.4.

In some special cases two ore more detectors are used simultaneously. For example, one detector collects the backscattered particles at $\Theta = 165^{o}$ and the other one may be used for high-resolution RBS (at $\Theta = 97^{o}$) or for collecting the recoiled particles (near $\Theta = 20–30^{o}$). Each detector must have its own preamplifier, amplifier and a separate bias power supply (see Fig. 35). Some multi-channel analysers are capable of digitalizing signals from different input sources in the same time. They use an external or an internal Mixer/Router module. Selecting the number of input channels of MCA cause the firmware to divide its memory into *n* equal parts for separate data storage for each input. It is important to notice that the MCA selects the input where the signal arrives from and analyse only this signal. During the analysis the remaining input channels are blocked.

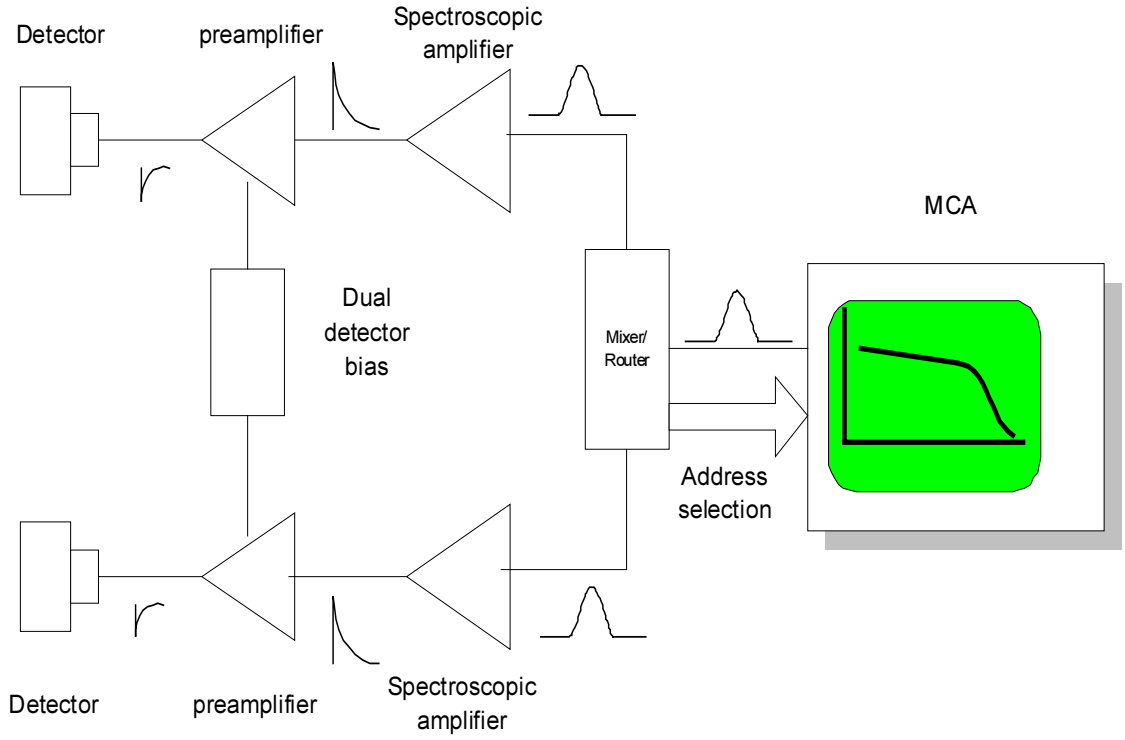

FIG.35. Set-up with two detectors.

4.5.1. Energy calibration

The energy of the detected particles is converted to a charge pulse and after suitable amplification to a voltage pulse. The height of the analog voltage pulse is converted further to the digital output of the ADC (channel number). The energy (E) of the detected particle is linearly proportional to the channel number (ch) of the MCA:

$$E = kch * ch + E_0, \tag{16}$$

where *kch* (keV/channel) and E_0 (zero offset) are the energy calibration coefficients. These parameters are needed for the evaluation of the spectra or for fitting a theoretical spectrum to the experimental one. Both parameters must be obtained to calibrate the analyser. Two channel positions of known energy values are sufficient, but it is better to have more and calculate *kch* and E_0 by linear regression. In RBS analysis the energy of the particles scattered from known surface elements can be calculated by Eq. (12). Therefore, one can use a standard sample for energy calibration, which contains at least two elements on its surface. From the position of the surface peaks or steps and the corresponding energy values the calibration coefficients are evaluated through linear regression.

4.5.2. Pile-up

When two particles arrive at the detector within the width of the output pulses of the spectroscopy amplifier, their respective amplified pulses pile-up and form an output pulse of distorted shape and amplitude. The Multichannel Analyser digitises this signal as one pulse, where height is higher then the height of any of the original signals. This leads to significant distortion in the spectrum, especially when the count rate is high. In order of reduce the pile-up effects, many spectroscopic amplifiers have a pile-up rejection circuit. These amplifiers together with the "slow" signal generate also a "fast" pulse using a very fast shaping time constant. A fast discriminator unit converts this analog signal into logic pulse. The trailing edge of the output of the fast discriminator triggers an inspection interval T_{INS}, that covers the width of the slow amplifier pulse. If a second input pulse arrives in this interval its fast discriminator pulse generates an inhibit pulse. This pulse is used to prevent the analysis of the pile-up event in the MCA. For correct rejection, the slow signal is delayed by the inspection time. This method reduces the fraction of the pile-up events at the expense of an additional "dead time" in the spectroscopic system.

4.6. DATA ANALYSIS SOFTWARE

4.6.1. History of simulation codes

The first computer codes calculated the energy spectrum of backscattering particles by numeric integration methods [124–127]. These programs for both incoming and outgoing paths evaluated the energy loss at all depths inside the target in small intervals. In 1975 Chu and Ziegler developed the basic approximate analytic expressions for nuclear elastic backscattering methods [128]. Later Ziegler, Lewer and Hirvonen published a computer code generating simplified backscattering spectra, neglecting the effect of energy straggling of penetrating ions [79]. In 1976 Borgesen, Harris and Scherzer presented a program to synthesise backscattering spectra for samples composed of successive layers of uniform thickness and composition [130]. Brice [131] investigated the effect of energy straggling and skewing of the projectile ions on the backscattering spectra of thick targets. He used various distribution functions to fit the predicted spectrum to the observed one and tried to account for the low energy tails observed in the experimental spectra. Weber and Mommsen gave a simple analytical formula to calculate the low energy tail assuming that it is produced by double-scattered particles [132]. Saunders and Ziegler have developed a versatile and interactive computer code for usual backscattering analysis [133]. A more sophisticated program providing analysis of both RBS and NRA (Nuclear Reaction Analysis) spectra has been published by Borgesen, Behrisch and Scherzer [134]. Kido and Oso have developed three types of computer code to analyse backscattering spectra for: i.) multi-elemental, multi-layered structures, ii.) inhomogeneously distributed impurity atoms and iii.) the crystallinity of damaged single crystal [135–137]. The later program was extended to simulate a channelling spectrum too. The authors took into account the effect of isotopes as well as the effects of energy fluctuation due to the system resolution and energy straggling of penetrating ions.

While these programs generate near accurate spectra, they work on large mainframe computers. Doolittle [138] presented an algorithm that can substantially reduce the number of arithmetic operations needed to compute a theoretical spectrum. Straggling and detector resolutions are among the effects included in the code.

In the last fifteen years new methods of ion backscattering spectroscopy were developed. Heavier ions were used at energies from few MeV to tens of MeV for better depth resolution or detection of light elements [139, 140]. For H and D profile analysis the elastic recoiled detection analysis method (ERDA) was also developed [141]. Light ions of low energy and selected nuclear reactions were used to enhance the sensitivity for light elements. At these energies the nuclear potential dominates.

As a consequence of progress in computer technology, the large mainframe computers were replaced by small, cheap personal computers (PCs). The low price of these PCs and programs made it possible to use these small computers as standard tools for data collection and data analysis in all laboratories. Simultaneously the graphical capacities of computers were developed too. The high resolution multicolor display is now a standard supplemental device of PCs. The first "MCA plug-in card" for IBM PCs and compatibles appeared in the second half of eighties. These were completed width integrated 2k, 4k or 8k ADC and memory. With their MCA emulation software they can transform the personal computer to a versatile multi-channel analyser while keeping its computational capabilities.

The first widely distributed PC program was developed by Doolittle (RUMP [138]). Later, in 1988, the RUMP code was modified to handle non-Rutherford ^{4}He ion backscattering spectra [142] and ERDA analysis, as well. A versatile RUMP-like code for simulation of nuclear reaction and elastic recoil spectra was described by Vízkelethy in 1990 [143]. In 1992, Saarilahti and Rauhala published a computer program package (GISA) for analysis of ion backscattering data. It included a database of non-Rutherford ^{1}H and ^{1}He scattering cross-sections for several light elements, as well [144]. The RBX code was developed by E. Kótai [145] for RBS and ERDA analysis and spectrum synthesis. This program calculates the depth distribution of selected elements and the distribution of the crystal defects in single elemental crystals. The BSCAT code was developed for analysis and simulation of complex spectra recorded in RBS, NRA and PIXE experiments [146]. It runs on MS Windows 95 and UNIX operation systems.

Another way to analyse ion backscattering spectra is to calculate the sample parameter directly from the experimental spectra. This type of program, due to the limitations of the RBS method itself, requires also some information about the sample. These programs were developing together with the RBS methods. The first codes gave only some limited information (energy conversion to surface mass, or depth, depth scales). In 1982 Borgesen, Behrisch and Scherzer developed a procedure by which the in-depth composition was determined for previously determined target components in a stepwise manner starting at the target surface [134]. Lewis published a deconvolution technique for depth profiling with nuclear microanalysis [147]. Rauhala gave the first automatic iteration methods in 1984 [148]. The input of this procedure was the parameters derived by the user from the experimental spectra. Eridon and Was in 1985 [149] and Butler in 1986 [150] published a computer code for automatic interactive fitting of ^{4}He ion backscattering spectra. Doolittle extended his RUMP code with a semi-automatic process in 1986 [151]. The computer program package GISA [144] of Saarilahti and Rauhala had automatic iteration capability and depth profiling methods, as well. In 1997 a new combinatorial optimisation algorithm based on “simulated annealing” was published and applied to the analysis of Rutherford backscattering data [152].

Modern computer codes take into account several, earlier neglected finer details, such as electronic screening, corrected Bohr straggling, non-linear detector response and effects of multiple scattering, pile-up and low-energy background tail. Szilágyi and Pászti developed a PC-code (DEPTH), that takes into account the effects of energy and nuclear spread of beam, the geometrical spread caused by finite beam spot and detector solid angle, the straggling and multiple scattering in the sample and the effects of absorber foils [153]. Itoh et al. published a method to simulate RBS spectra for a surface with periodic roughness [154]. Several programs take into account the effects of

the plural scattering, which is responsible for the background appearing at energies below the RBS signal of high Z layers (DRBS [132], SIMNRA [155], TRBS [156, 157]).

For the simulation of channelling spectra, two methods were developed: the analytical approach [158, 159] and the Monte-Carlo simulation (CASSIC [160]).

Several computer codes also provide control over the experimental setup. These programs include forms that control the sample goniometer, iterate the acquisition sequence through a number of samples, acquire lateral and angle resolved images and store the data when the accumulated charge carried by the incident ions reach a preset number of micro coulombs (DETECTOR/DETACQ [161], ARIBA [162], RBX [145]).

A collection of freeware and shareware IBA programs is available from the Internet. One of the famous sources is the SIGMABASE [163]. One can download from there the following programs:

- ALEGRIA1.2
  Conversion of ERD and NRA spectra to depth profile by F. Schiettekatte and G. Ross [164].
- DEPTH
  Depth resolution and cross section calculations by E. Szilágyi [153].
- GISA 3.3
  RBS simulation and evaluation by J. Saarilahti [144].
- RUMP ERD
  A modification of RUMP to handle ERD better by L.J.M. Jaegers and J.L.J. van Ijzendoorn.
- SENRAS
  Simulation and evaluation of NRA by G. Vízkelethy [143].
- SIMNRA
  Simulation of RBS with emphasis on Non-Rutherford Scattering by M. Mayer [155].
- SPACES (DOS)
  Calculation of energy straggling and excitation curves by I. Vickridge [165].
- SPACES for Windows
  Windows version of SPACES [165].

The IBA program developed by J.F. Ziegler is published by IBM. This package contains programs for analysis of data from ion scattering experiments (RBS), and those from target atom recoiling experiments (ERD).

4.6.2. Spectrum synthesis

In analysis of a solid by RBS or ERDA the sample is bombarded by ions of a given energy, atomic number and atomic mass, and the quantities recorded are the energy E and number of particles $Y(E)$ scattered or recoiled into a given angle. An RBS spectrum is a plot of the yield $Y(E)$ versus energy the E with δE channel width. The first step of any calculation is to define all the measuring parameters. In the standard RBS method, all parameters are described in laboratory system. The main input parameters are the following:

E_0 Energy of ions before hitting the target in keV,
Z_1 Atomic number of ions (all atoms),
M_1 Atomic mass of ions (all isotopes),
θ Detection angle measured from the beam direction,

α Target tilt (the angle between the beam direction and the surface normal),
β Angle between the outgoing particles and the surface normal,
Q Number of incident particles,
Ω Solid angle of the detector and
ΔE Detector resolution.

The relation between θ, α and β depends on the position of detector (see Fig. 36a). In the case of IBM geometry, $\beta = \theta - \alpha$, and in CORNELL geometry $\cos(\beta) = \cos(\alpha)\cos(\pi - \theta)$. The calculation of some special effects needs additional inputs too (e.g. beam current i_{beam} for pile-up calculation, shape of the beam spot and that of the detector or of its collimator diaphragm for geometrical straggling, etc.).

The next step is to describe the sample in a formal way. Most of the simulation programs consider the sample as a stack of sublayers, each of its uniform composition. The input parameters of each layer are the thickness d and the elementary composition (the atomic number z_i and the mass m_i and the relative composition n_i).

The scattering geometry is shown in Fig. 36 in three different cases: standard RBS, standard ERDA and transmission geometry (forward scattering). This schematic diagram includes the kinematics, the energy loss and the depth scale together with the shape of the spectra. There $\varepsilon(E)$ is the energy dependent stopping cross section, $\sigma(E)$ is the differential cross section, A_i and H_i are the area and height of the i-th peak, respectively. Let us consider the scattering events occurring in the target at a thin slice of thickness δx located at a given depth x.

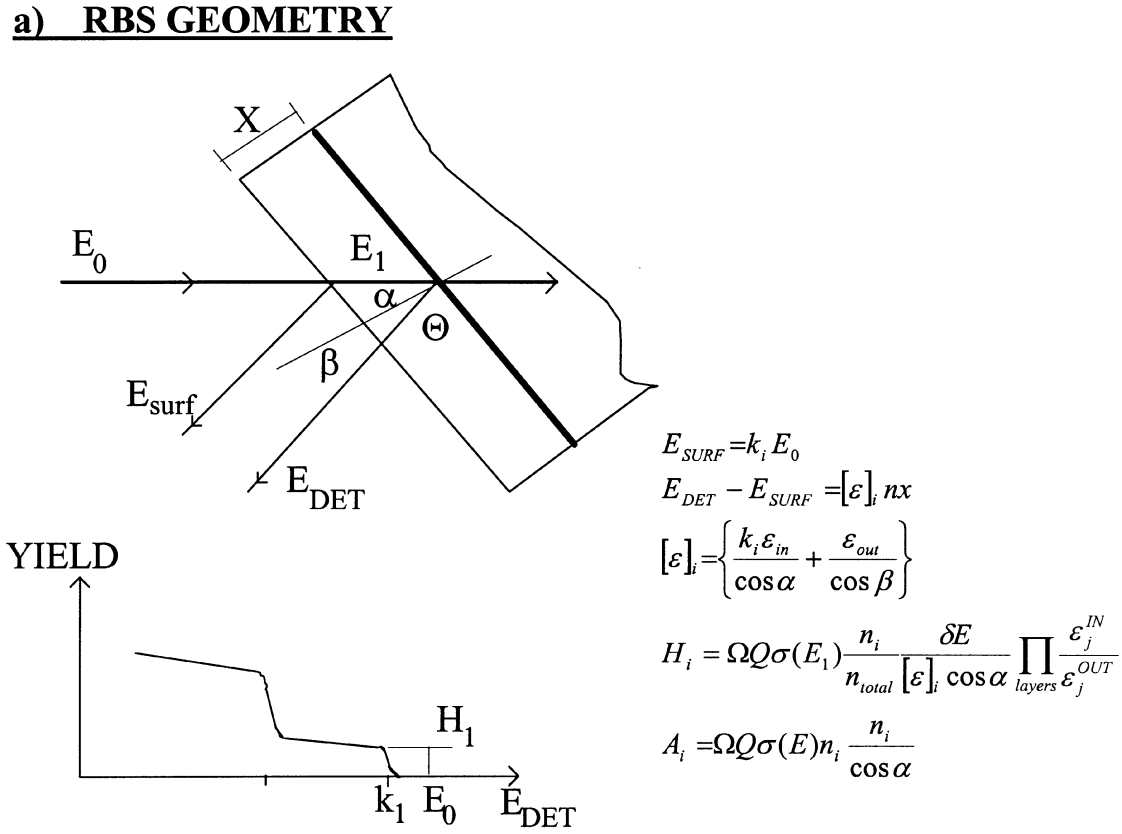

FIG. 36. (a) The scattering geometry. Conception of RBS.

b) ERDA geometry

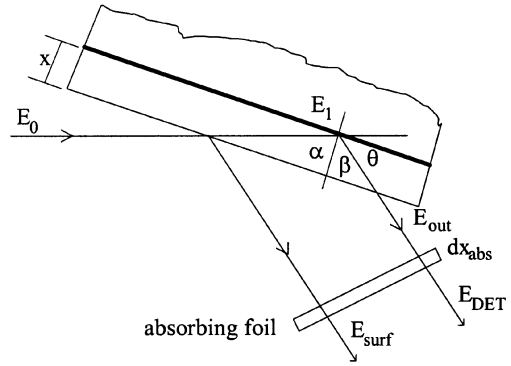

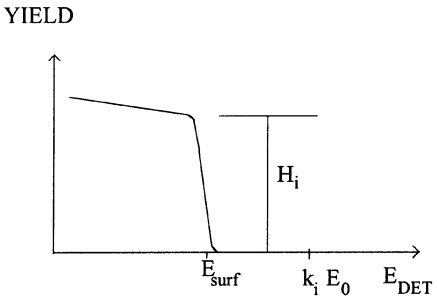

$$E_{SURF} = k_i E_0 - \varepsilon_{abs}(k_i E_0) n_{abs} dx_{abs}$$

$$E_{DET} - E_{SURF} = [\varepsilon]_i nx + (\varepsilon_{abs}(k_i E_0) - \varepsilon(E_{out})) n_{abs} dx_{abs}$$

$$[\varepsilon]_i = \left\{ \frac{k_i \varepsilon_{in}}{\cos\alpha} + \frac{\varepsilon_{out}}{\cos\beta} \right\}$$

$$H_i = \Omega Q \sigma_i(E_1) \frac{n_i}{n_{total}} \frac{\delta E}{[\varepsilon]_i \cos\alpha} \prod_{layers} \frac{\varepsilon_j^{IN}}{\varepsilon_j^{OUT}} \frac{\varepsilon_{abs}^{IN}}{\varepsilon_{abs}^{OUT}}$$

$$A_i = \Omega Q \sigma_i(E) n_i \frac{n_i}{\cos\alpha}$$

FIG. 36.(b) The scattering geometry. Conception of ERDA.

c) FORWARD geometry

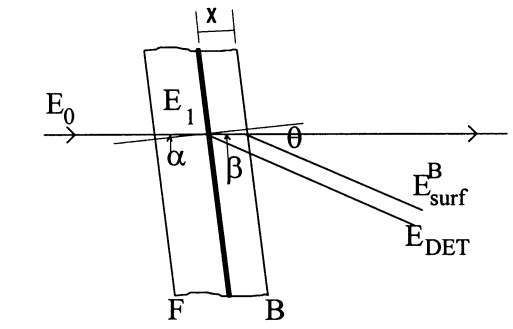

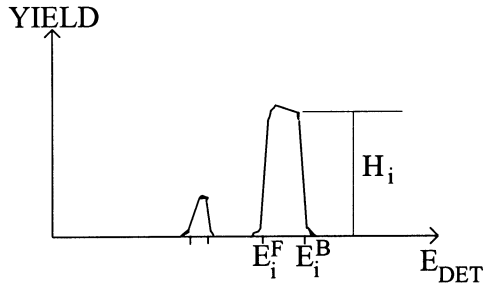

$$E^B_{surf} = k_i (E_0 - \varepsilon_{in} n \frac{dx_{foil}}{\cos\alpha})$$

$$E^F_{surf} = k_i E_0 - \varepsilon_{in} n \frac{dx_{foil}}{\cos\beta}$$

$$E_{DET} - E^B_{SURF} = [\varepsilon]_i nx$$

$$[\varepsilon]_i = \left\{ -\frac{k_i \varepsilon_{in}}{\cos\alpha} + \frac{\varepsilon_{out}}{\cos\beta} \right\}$$

$$H_i = \Omega Q \sigma(E_1) \frac{n_i}{n_{total}} \frac{\delta E}{[\varepsilon]_i \cos\alpha} \prod_{layers} \frac{\varepsilon_j^{IN}}{\varepsilon_j^{OUT}}$$

$$A_i = \Omega Q \sigma(E) n_i \frac{\Delta x}{\cos\alpha}$$

FIG. 36. (c) The scattering geometry. Conception of forward scattering.

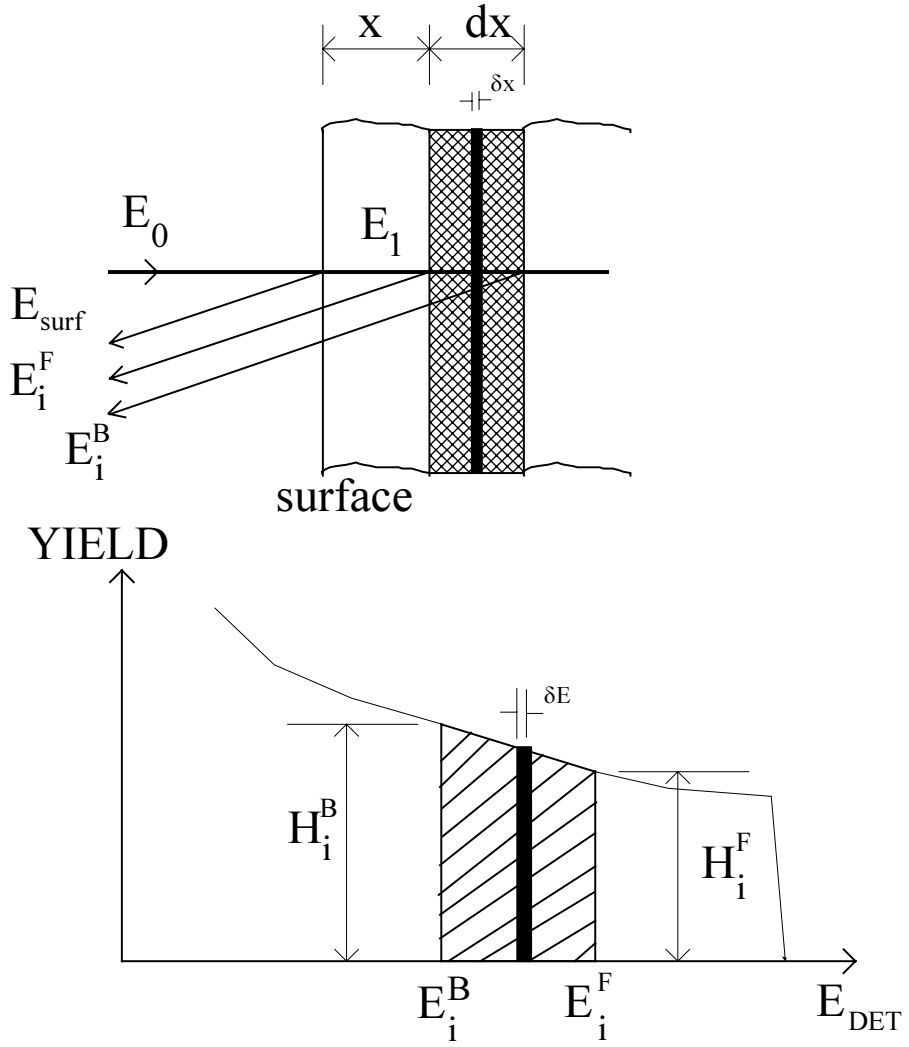

FIG. 37. Basic element of spectrum synthesis: the brick.

Particles arriving at the front surface of δx have an energy of E_1, that transforms after scattering into kE_1, where k is the kinematic factor. After leaving the target, the particles have an energy of E_{out}. The differences between E_0 and E_1 and that of kE_1 and E_{out} are due the energy loss along the incoming and outgoing path, respectively. In the ERDA method an absorbing foil is placed before the detector. In this case the detected energy E_{det} is different from E_{out} due to the energy loss of ions in the foil and it depends on the thickness and composition of absorber too.

The simulated spectrum is constructed by superimposing the contributions from each isotope of each sublayer in the sample. In the first step, we neglect the statistical energy fluctuations due to the instrumental system resolution and the energy straggling of particles. In this case the contribution is considered as a brick of height H_i^F, H_i^B, and position of E_i^F and E_i^B (Fig. 37). If the energy width of the brick of the i-th element is equal to the channel width δE of the ADC, then the detected yield is the following:

$$H_i(E) = \int_x^{x+\delta x} dx' Q \int d\Omega \frac{d\sigma_i(E(x'),\theta)}{d\Omega} \frac{n_i(x')}{n_{total}(x')} \frac{\delta E}{\cos\alpha} \frac{1}{[\varepsilon(E(x'))]} \prod_{j=\text{layers}} \frac{\varepsilon_j(E_{IN})}{\varepsilon_j(E_{OUT})} \tag{17}$$

where n_i is the atomic concentration of the i-th element at x' depth and δx is the effective thickness (the path of penetration) of the slab.

The first factor, Q, is the number of projectiles bombarding the target. In most cases, Q is determined by measuring the integrated charge carried by the ions onto the target sample. The precision of this measurement depends on the neutral fraction of the beam and the number of secondary electrons created by the collision of ions with the target and the construction elements of the beam line. The precision of determination is 5–10%, depending on the efficiency of secondary electron suppression, but it can be improved using special charge measuring systems or beam monitors. Pászti et al. found a precision better then 1% using a transmission Faraday-cup [84].

The second factor, $\frac{d\sigma}{d\Omega}$ is the differential scattering cross section. In the standard RBS methods, it is assumed that the differential scattering cross section is a Rutherford cross section. This assumption is valid for He in the range of ~800 – 2400 keV and ~50 – 700 keV for H. In the case of He ions the light atoms have some resonances above this energy (for example $^{12}C(\alpha,\alpha)^{12}C$ [166], $^{14}N(\alpha,\alpha)^{14}N$ [167], $^{16}O(\alpha,\alpha)^{16}O$ [168], etc.), but the deviation of the cross section of the heavier target atoms from the Rutherford cross section may be neglected up to 4 MeV. For H ions with energy above a few hundred keV the cross section of elements differs from Rutherford cross section, and in this range, the $\sigma(E)$ function can not be written in a general analytical equation for all the elements. Often the effects of the nuclear resonant scattering processes enhance the elastic cross section over the Rutherford values by a factor of 2–3 orders of magnitude. However, there are also some energy regions where the cross section is less then the Rutherford value.

At lower energy and for higher Z elements the core electrons screen the nuclear charges of the ions and that of the target atoms from each other, reducing the cross section somewhat below the Rutherford value. For example, 3.5% deviation was observed for 1 MeV He on Bi [169]. L'Ecuyer, Davies and Matsunami [170] gave an analytical expression for the correction factor of screening.

$$\frac{d\sigma(E)}{d\Omega} = \left(\frac{d\sigma(E)}{d\Omega}\right)^{Lab}_{Ru\,\mathrm{th}} \left[1 - \frac{0.049 Z_1 Z_2^{4/3}}{E_{CM}\,(keV)}\right] \tag{18}$$

MacDonald and co-workers measured the cross section of the He ions for O, Al and Si [171]. They have found that over the 0.6–2.3 MeV energy range the ^{4}He backscattering cross section for these elements follows within 1–2% the E^{-2} energy dependence of the Rutherford formula.

The simplest way to evaluate the non-Rutherford cross section is using tabulated values. This method is used in several simulation programs (RUMP [142], SENRAS [143] GISA [144], and RBX [145]). The advantage of this method is the easy way of modifying or supplementing the database. Time-consuming calculations creating such tables can be written as separate programs (e.g. Blanpain and co-workers [143] wrote a program to implement the calculation done by Cameron [172] for $^{16}O(\alpha,\alpha)^{16}O$ and Hill [165] for $^{12}C(\alpha,\alpha)^{12}C$. The main disadvantages of storing cross sections into tables are the large size of data and the need for interpolation to calculate the cross section values at non tabulated energies.

Non-Rutherford cross-sections may also be evaluated by fitting functions. Many fitting functions on experimental cross section data have been published in the last years. For proton scattering on light elements Knox and his co-workers gave fitting functions that are similar in form to each other and they integrated these into the RUMP program [173]. The differential cross section of recoiled atoms in He ERDA may be approached by a second-order surface [174], a polynomial [175] or a Lorentzian function [176]. The application of these functions increases the computation time but decreases the size of the memory required by the program. However, the validity of these functions is

limited only to a range of energy and scattering angle. These limits are determined in the stack of the experimental data.

Several fitting functions are built into the RBX program [145] (the $\sigma(E)$ function can be linear, polynomial, Lorentzian, Breit-Wigner, enhanced Rutherford, etc.). The energy-cross section values or the parameters and energy limits of these methods are saved in cross section library files. RBX includes a utility program to create and maintain these libraries.

In RBS and ERDA the solid angle of the detector is relatively small, therefore the integration of cross section over the detection angle can be replaced by an averaged cross section value corresponding to the centre of the detector. The variation of cross section between the front and back surface of the thin slabs depends on the energy loss of penetrating ions. In most cases these energy losses in a slab (corresponding to δE) is a few keV, and the change of the cross section can be neglected. For narrow nuclear resonances, however, numerical or analytical integration has to be performed. The calculation time can be decreased if the integrated cross section data are stored in a table. The precision of calculation depends on the density of the experimental points around the resonance energy.

The third factor in Eq. (17), $\frac{n_i}{n_{total}}$, describes the relative atomic concentration of the i-th element in the current layer. However, most of the simulation programs assume that the concentration of the elements in sublayers is uniform and concentration steps may be found at the interfaces.

The fifth factor in Eq. (17), $\left[\varepsilon\left(E(x)\right)\right]$, is the stopping cross section factor for the i-th component. It is defined in the review of Chu et al. [66] as

$$\left[\varepsilon(E)\right]_i = k_i \varepsilon(E) + \varepsilon\left(k_i E\right) \tag{19}$$

where E is the energy of the ions before scattering and ε is the energy dependent stopping cross section. The expression used for ε might be for He the Ziegler's stopping formula [177], or for H and heavy ions the calculation method suggested by Ziegler, Biersack and Littmark [178]. For stopping in compounds Bragg's rule [184] has to be applied.

The last part in the expression of H_i is a product taken over all the overlaying sublayers and the absorbent foil. The dispersion of the scattered beam must be taken into account through a correction factor.

The simulation programs create a virtual multi-channel analyser, and sum there the yields of the various nuclides of the sublayers. The first step of calculation is to determine the energy of the penetrating ions at the front and the back interfaces of the layers, E_{ion}^{F}, E_{ion}^{B}. The next step is to calculate the detected energy of the scattered or recoiled particles E_{det}^{F}, E_{det}^{B}, then the yield at these energies using Eq. (17). The computation of yield of the brick between E_{det}^{F}, and E_{det}^{B} is based on the assumption that within this thin slab the energy of the penetrating ions and the stopping factor changes slowly. For narrow nuclear resonances, $\sigma(E)$ can be replaced by its integrated value over the slab. This assumption is valid only for thin sublayers. The maximum allowable width of these sublayers depends on the stopping power of the particles in these layers along their incoming and outgoing paths (e.g. in the case of RBS using 1–4 MeV He beam, at normal incidence this thickness is ~10^{18} at/cm^2). Therefore most of the programs have a special input parameter, the maximum width of the slices Δx.

If the path-length of ions in a layer of the sample would be greater than Δx, then the program automatically cuts this layer into sublayers of widths less or equal than this value.

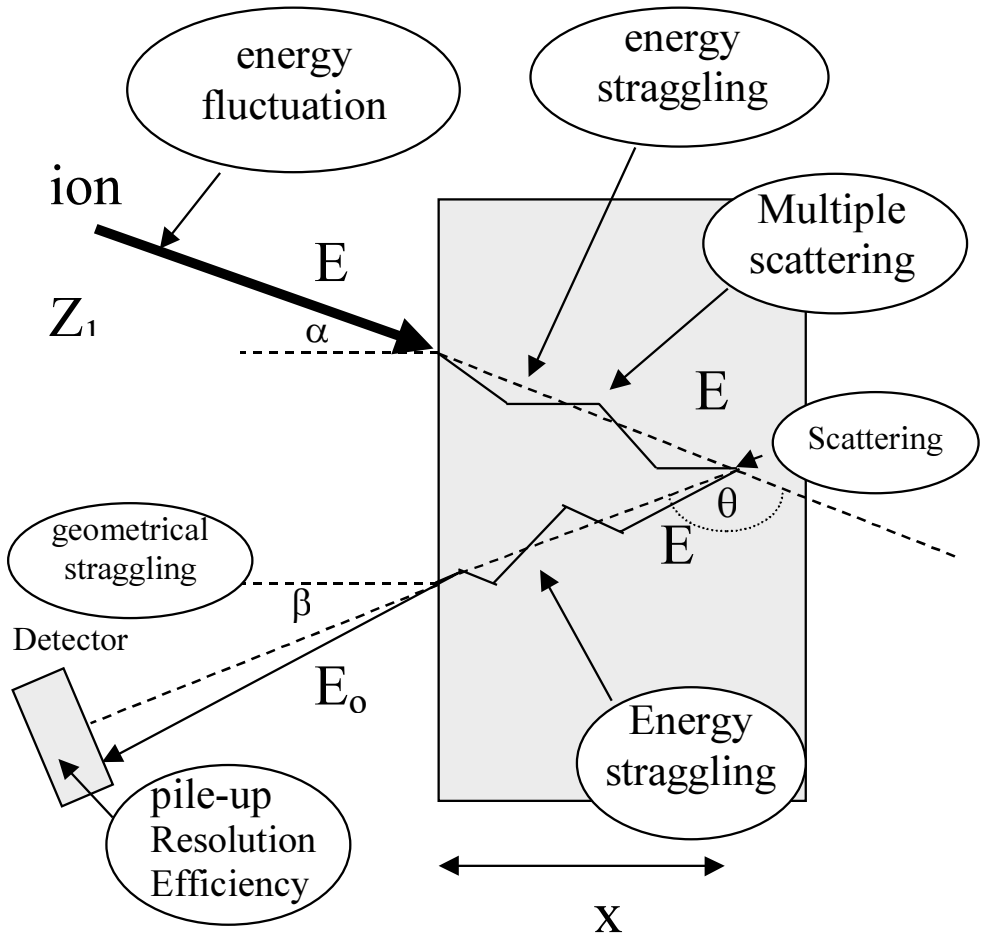

FIG. 38. Effects on system resolution.

In order to generate a realistic spectrum, we must take into account the energy fluctuations due to the following factors: i) energy straggling of the ions penetrating into the target ii) energy straggling of the detected particles along the outgoing path and in the absorbing foil, iii) multiple scattering, iv) geometrical spread due to the finite detector acceptance angle and the beam size, v) the angular and lateral spread of the particles and finally vi) the instrumental system resolution (see Fig. 38). Accounting for all these effects the program makes a great deal of extra computations.

4.6.2.1. Straggling

Doolittle published an algorithm calculating the energy straggling and built this method into the RUMP program [138]. Saarilahti and Rauhala used the Bohr theory of beam straggling in the GISA code [144]. The RBX code takes into account both the Bohr and the geometrical straggling [145]. Szilágyi and Pászti developed a computer code (DEPTH) to calculate the correct energy fluctuation caused by all the mention effects [153].

The RBX program incorporates the energy straggling of the Bohr model as an option. It also uses the simple asymptotic formula of Lindhard and Scharff [180] that consider the local electron density of the target atom as

$$\frac{\Gamma^2}{\Gamma^2_{Bohr}} = \begin{cases} L(\zeta)/2 & for\ \zeta \le 3 \\ 1 & for\ \zeta > 3 \end{cases} \tag{20}$$

where $L(\zeta) = 1.36\ \zeta^{1/2} - 0.016\ \zeta^{3/2}$. Here, ζ is the reduced energy variable defined by $\zeta = v^2/(Z_2 v_o^2)$ (v is the ion velocity and v_o is the Bohr velocity). The program provides an opportunity to modify the calculated straggling for each layer by a correction factor (e.g. to take into account the effect of the remaining energy spread contributions, or that of the sample roughness).

The calculation of the effects of the geometrical straggling as a function of depth is based on the calculation by Williams and Müller [181]. It is assumed that both this straggling and the detector resolution are Gaussian; therefore the square of standard deviation of the resulting energy straggling, Ω_E, can be computed by adding the square of the individual standard deviations. The program calculates the straggling at each side of each brick. The brick itself is built up as

$$y_r = \sum_j H_j \frac{\delta E}{\Omega_E \sqrt{2\ln 2}} \exp\left(- \frac{(i-j)^2 \delta E^2}{2\Omega_E^{\ 2}} \right) \tag{21}$$

where H_j is calculated by Eq. (17), δE is the channel width and Ω_E is interpolated between the calculated values at the front and the back surface of the sublayer. This method increases the computation time even in the case of a very complex sample by less then 10% only.

4.6.2.2. Pile-up

To calculate the pile-up contribution a simple approximation can be used [182]. If the yield in the *i*-th channel of the synthesised spectrum is denoted by *H(i)*, then the pile-up contribution is given by:

$$PILEUP(i) = p \sum_{i'=1}^{i-1} H(i')\, H(i-i') \tag{22}$$

where p is the probability of the pile-up effect. The probability is proportional to the count rates. To keep the total integrated count unchanged the program normalises the calculated spectrum.

4.6.3. Spectrum analysis

The main goal of the analysis is to get all the available information about the sample. The wish of all scientists is to "push a button" and then just wait (a short time) until the computer gives the complete description of the target. This demand is too common and needs a very complex and versatile program. In most cases the user has some knowledge about the sample and it is enough to focus the analysis on the difference between the theoretical and experimental data. A good method might be to get first some rough information about the sample, then investigate it in detail.

For interactive spectrum analysis the following tasks can be performed fast :

(1) identify surface elements,
(2) calculate and display the depth scale for a given element,
(3) calculate the areal density of a surface layer (in at/cm^2 units),
(4) calculate the energy of the penetrating ions before scattering,
(5) calculate the energy corresponding to a given channel,
(6) calculate the area or the integrated counts of a peak.

These calculations use the surface approximation. The necessary equations for such calculations are well documented and discussed in the literature [66]. For depth scale calculation the program needs the description of the surface layer too. For example, after defining an element or an energy range of interest (ROI) in the spectrum, the RBX code displays continuously all the six mentioned characteristics for the detected energy defined by the cursor position.

The main aim of the detailed analysis is to get the depth profiles of the various elements in the sample. For this, the program can use different methods, such as (i) surface approximation, (ii) comparing the yields of the elements, (iii) performing simulation and (iv) multiple iteration.

The first method is very simple and fast, but it gives correct results only in thin surface films, were the changes in the cross section and in the stopping factor are negligible. It gives the depth profile of the investigated element by the formula:

$$n_i(x) = \frac{H_i \left[\varepsilon(E_0)\right]_i}{\Omega \; Q \; \sigma_i(E_0) \; \delta E} \tag{23}$$

where H_i is the measured yield of the given element that can be obtained from the experimental spectrum by subtracting the background.

The second method calculates the relative concentration of two selected elements from their yields:

$$\frac{n_1}{n_2} = \frac{H_1}{H_2} \frac{\left[\varepsilon(E_0)\right]_1}{\left[\varepsilon(E_0)\right]_2} \frac{\sigma_2(E_0)}{\sigma_1(E_0)} \tag{24}$$

The simulation method is based on a full but approximate description of the sample, and it uses at each depth the calculated cross-sections and stopping factors. The program simulates a probe spectrum in all the layers assuming a low and constant concentration for the given element, then calculates the profile from the ratio of the yields in the experimental and the synthesised spectra. The effect of concentration gradient on the stopping within a layer is neglected. It is a useful and fast method, if the concentration of the given element is less then few percent. The last method repeats the above calculation a few times, always using the concentration profile given by the previous result.

REFERENCES

[1] High Voltage Engineering Europa B.V., Amersfoort, Netherlands.

[2] ALTON, G.D., Nucl. Instr. and Meth. **B73** (1993) 221–288.

[3] National Electrostatics Corporation, Middleton, Wisconsin, USA.

[4] HUMPHRIES, S., Jr. Principles of Charged Particle Accelerations, Wiley, New York (1986).

[5] BROMLEY, D.A., Nucl. Instr. and Meth. **122** (1974) 1.

[6] JOHANSSON, T.B., AXELSSON, K.R., JOHANSSON, S.A.E., Nucl. Instr. and Meth. **84** (1970) 141.

[7] JOHANSSON, S.A.E., CAMPBELL, J.L., MALMQUIST, K., Particle induced X-ray Emission Spectrometry (PIXE), Wiley, New York (1995).

[8] CAMPBELL, J.L., COOKSON, J.A., Nucl. Instr. and Meth. **B3** (1984) 185.

[9] JAKSIC, M., GRIME, G.W., HENDERSON, J., WATT, F., Nucl. Instr. and Meth. **B54** (1991) 491.

[10] Proceedings of the Eighth International Conference on PIXE and its Analytical Applications, Lund, Sweden, June 14–18, 1998, Nucl. Instr. and Meth. **B150** (1999) 1–694.

[11] ROTH, A., Vacuum Technology, 2nd Ed., North Holland, Amsterdam (1982).

[12] MAYER, L., Phys. Stat. Sol. **44** (1971) 253.

[13] MONTENEGRO, E.C., BAPTISTA, G.B., BARROS LEITE, C.V., DE PINHO, A.G., PASCHOA, A.S., Nucl. Instr. and Meth. **164** (1979) 231.

[14] WATT, F., GRIME, G.W., Principles and Applications of High Energy Ion Microbeams, Adam Hilger, Bristol (1987).

[15] EFMAN, M., HOMMAN, N.P.O., KRISTIANSSON, P., Nucl. Instr. and Meth. **B95** (1995) 122.

[16] ANTTILA, A., HANNINEN, R., RAIAANEN, J.J., Radioanal. Chem. **62** (1981) 441.

[17] KISS, A.Z., KOLTAY, E., NYAKO, B., SOMORJAI, E., ANTTILA, A., J. Radional. Chem. **89** (1985) 123.

[18] WILLIAMS, E.T., Nucl. Instr. and Meth. **B3** (1984) 211.

[19] MENU, M., Nucl. Instr. and Meth. **B75** (1993) 469.

[20] CALLIGARO, T., DRAN, J.C., MOIGNARD, B., SALOMON, J., presented at IBA-14 conference, Dresden (1999).

[21] DEMORTIER, G., MORCIAUX, Y., Nucl. Instr. and Meth. **B85** (1994) 112.

[22] CRC Handbook of Chemistry and Physics, CRC Press (1999).

[23] DOYLE, B.L., WALSH, D.S., LEE, S.R., Nucl. Instr. and Meth. **B54** (1991) 244.

[24] GRIME, G.W., Nucl. Instr. and Meth. **B109/110** (1996) 170.

[25] BOISSEAU, P., NETT, W., GRODZINS, L., Nucl. Instr. and Meth. **B79** (1993) 418.

[26] VAN KAN, J.A., VIS, R.D., Nucl. Instr. and Meth. **B109/110** (1996) 85.

[27] GONZALES, A.D., PACHER, M.C., MIRAGLIA, J.E., Phys. Rev. **A37** (1988) 4974.

[28] TERASAWA, M., TØRØK, I., PETUKHOV, V.P., Nucl. Instr. and Meth, **B75** (1993) 105.

[29] PETUKHOV, V.P., TØRØK, I., TERASAWA, M., Nucl. Instr. and Meth, **B109/110** (1996) 105.

[30] JOHANSSON, T.B., AKSELSSON, K.R., JOHANSSON, S.A.E., Nucl. Instr. and Meth. **84** (1970) 141.

[31] Systems, Instruments and Components (Oxford Instruments Inc. Catalogue), Nuclear Measurements Group, 601 Oak Ridge, USA; Catalogue of EG&G ORTEC, Oak Ridge, USA; Canberra Nuclear Instruments Catalog, Canberra Industries Inc., Meriden, CT, USA; Catalogue of Eurisys Mesures, St. Quentin Yvelines, France.

[32] New Product — Press Release of January 1999, Model XR-100CR, 186 eV resolution Si-Pin X-Ray Detector, Amptec Inc., Bedford, MA, USA.

[33] SILVER, E., et al., X-Ray Spectrom. **25** (1996) 115.

[34] FRANK, M., et al., Rev. Sci. Instrum. **69** (1998) 25.

[35] KALINKA, G., TANIGUCHI, K., Nucl. Instr. and Meth. **B75** (1993) 91.
[36] KNOLL, G.F., Radiation detection and measurement, Wiley, New York (1979).
[37] LEO, W.R., Techniques for Nuclear and Particle Physics Experiments, Springer Verlag, Berlin (1987).
[38] CAMPBELL, J.L., Nucl. Instr. and Meth. **B109/110** (1996) 71.
[39] INAGAKI, Y., SHIMA, H., MAEZAWA, H., Nucl. Instr. and Meth. **B27** (1987) 353.
[40] ALVES, L.C., JESUS, A.P., REIS, M.A., Nucl. Instr. and Meth. **B109/110** (1996) 129.
[41] MUSKET, R.G., Nucl. Instr. and Meth. **B15** (1986) 735.
[42] CALLIGARO, T., MACARTHUR, J.D., SALOMON, J., Nucl. Instr. and Meth. **B109/110** (1996) 125.
[43] GUI-NIAN, D., TURNER, K.E., X-Ray Spectrometry **18** (1989) 57.
[44] HOMMAN, N.P.O., Kristiansson, P., X-Ray Spectrom. **25** (1996) 66.
[45] THIBEAU, H, STADEL, J., CLINE, W., CAHILL, T.A., Nucl. Instr. and Meth. **111** (1973) 615.
[46] CAMPBELL, J.L., Nucl. Instr. and Meth. **B49** (1990) 115.
[47] KAVCIC, M., BUDNAR, M., MUHLEISEN, A., TOROK, I., Nucl. Instr. and Meth. **B138** (1998) 173.
[48] HILDNER, M.L., ANTOLAK, A.J., BENCH, G.S., Nucl. Instr. and Meth. **A373** (1996) 124.
[49] BUDNAR, M., MUEHLEISEN, A., Nucl. Instr. and Meth. **B75** (1993) 81–85.
[50] JOHANSSON, G.I., X-Ray Spectrom. **11** (1982) 194.
[51] SWANN, C.P., FLEMMING, S.J., Nucl. Instr. and Meth. **B49** (1990) 65.
[52] SERA, K., FUTATSUGAWA, S., Int. J. of PIXE **5** (1995) 181.
[53] ORLIC, I., SHIJUN ZHOU, SANCHEZ, J.L., WATT, F., TANG, S.M., Nucl. Instr. and Meth. **B150** (1999) 83.
[54] VEKEMANS, B., JENSENS, K., VINCZE, L., ADAMS, F., VAN ESPEN, P., X-ray Spectrom. **23** (1994) 278–285.
[55] REIS, M.A., ALVES, L.C., Nucl. Instr. and Meth. **B68** (1992) 300.
[56] RYAN, C.G., COUSENS, D.R., SIE, S.H., GRIFFIN, W.L., Nucl. Instr. and Meth. **B49** (1990) 271.
[57] MAXWELL, J.A., CAMPBELL, J.L., TEESDALE, W.J., Nucl. Instr. and Meth. **B43** (1989) 218.
[58] CLAYTON, E., PIXAN, The Lucas Heights PIXE Analysis Computer Package, **AAEC/M113** (1986).
[59] SZABO, G., BORBELY-KISS, I., Nucl. Instr. and Meth. **B75** (1993) 123.
[60] SERA, K., FUTATSUGAWA, S., Nucl. Instr. and Meth. **B109/110** (1996) 99–104.
[61] BOMBELKA, E., KOENIG, W., RICHTER, F.W., WATJEN, U., Nucl. Instr. and Meth. **B22** (1987) 21.
[62] POTOCEK, V., TOULHOAT, N., Nucl. Instr. and Meth. **B109/110** (1996) 197–202.
[63] ORLIC, I., et al., Nucl. Instr. and Meth. **B130** (1997) 133.
[64] WEBER, G., ROBAYE, G., DELBROUCK, J.M., ROELANDTS, I., ALOUPOGIANNIS, P., Nucl. Instr. and Meth. **B109/110** (1996) 186–191.
[65] LIPWORTH, A.D., ANNEGARN, H.J., KNEEN, M.A., Nucl. Instr. and Meth. **B75**(1993)127.
[66] CHU, W.-K., MAYER, J.W., NICOLET, M.-A., Backscattering Spectrometry, Academic Press, New York (1978).
[67] LEAVITT, J.A., MCINTYRE, L.C., Jr., WELLER, M.R., in Handbook of Modern Ion Beam Materials Analysis (TESMER, J.R., NASTASI, M., BARBOUR, J.C., MAGGIORE C.J., MAYER, J.W., Eds), Materials Research Society (MRS), Pittsburgh (1995) 37.
[68] MORGAN, D.V., (Ed.), Channelling: Theory, Observation and Applications, Wiley Interscience, New York (1973).

[69] SWANSON, M.L., in Handbook of Modern Ion Beam Materials Analysis (TESMER, J.R., NASTASI, M., BARBOUR, J.C., MAGGIORE C.J., MAYER, J.W., Eds) Materials Research Society (MRS), Pittsburgh (1995) 231.
[70] TESMER, J.R., MAGGIORE C.J., NASTASI, M., BARBOUR, J.C., MAYER, J.W., (Eds), High Energy and Heavy Ion Beams in Materials Analysis, Materials Research Society (MRS), Pittsburgh (1990).
[71] Modular Pulse-Processing Electronics and Semiconductor Radiation Detectors, Catalogue of EG&G ORTEC, Oak Ridge, USA.
[72] BERGSTRÖM, I., BJÖRKQVIST, K., DOMEIJ, B., FLADDA, G., ANDERSEN, S., Can. J. Phys. **46** (1978) 2679.
[73] ZIEGLER, J.F., Nucl. Instr. and Meth. **B136/138** (1998) 141.
[74] STEINBAUER, E., et al., Nucl. Instr. and Meth. **B85** (1994) 642.
[75] Mars Pathfinder Rover Alpha Proton X-ray Spectrometer (APXS), National Space Science Data Center, Code 633.2, NASA Goddard Space Flight Center, Greenbelt, MD USA.
[76] RIEDER, R., WANKE, H., ECONOMOU, T., TURKEVICH, A., J., Geophys. Res. **102** (1997) 4027.
[77] GRIME, G.W., DAWSON, M., MARSH, M., MCARTHUR, I.C., WATT, F., Nucl. Instr. and Meth. **B54** (1991) 52.
[78] INOUE, K., et al., Nucl. Instr. and Meth. **B30** (1988) 580.
[79] MIMURA, R., SAWARAGI, H., AIHARA, R., TAKAI, M., Nucl. Instr. and Meth. **B85** (1994) 756.
[80] KAMIYA, T., SUDA, T., TANAKA, R., Nucl. Instr. and Meth. **B118** (1996) 447.
[81] JAMIESON, D.N., Nucl. Instr. and Meth. **B136/138** (1998) 1.
[82] BREESE, M.B.H., JAMIESON, D.N., KING, P.J.C., Materials Analysis with a Nuclear Microprobe, Wiley, New York (1996).
[83] LEGGE, G.J.F., Nucl. Instr. and Meth. **B130** (1997) 9.
[84] PÁSZTI, F., MANUABA, A., HAJDU, C., MELO, A.A., DA SILVA, M.F., Nucl. Instr. and Meth. **B47** (1990) 187.
[85] SITTER, C., DAVIES, J.A., JACKMAN, T.E., NORTON, P.R., Rev. Sci. Instr. **53** (1982) 797.
[86] L`ECUYER, J., BASSARD, C., CARDINAL, C., TERREAULT, B., Nucl. Instr. and Meth. **149** (1978) 271.
[87] PÁSZTI, F., et al., Nucl. Instr. and Meth. **B15** (1986) 486.
[88] Charles Evans & Associates, Rutherford Backscattering System-400, Redwood City, CA, USA; High Voltage Engineering Europa B.V., Amersfoort, Netherlands.
[89] HARRIS, N.S., Modern Vacuum Practice, McGraw-Hill Int., Cambridge (1989).
[90] ROTH, A., Vacuum Technology, North Holland, Amsterdam (1990).
[91] MÖLLER, W., PFEIFFER, TH., SCHLUCKEBIER, M., Nucl. Instr. and Meth. **182/183** (1981) 297.
[92] PÁSZTI, F., et al., Nucl. Instr. and Meth. **119** (1983) 26.
[93] JEYNES, C., BARRADAS, N.P., BLEWETT, M.J., WEBB, R.P., Nucl. Instr. and Meth. **B136/138** (1998) 1229.
[94] Pfeiffer Vacuum — Vacuum Technology ‘97 Catalogue, Pfeiffer Vacuum GmbH, Asslar, Germany.
[95] Edwards Vacuum Products 1997–1998 Catalogue, Edwards High Vacuum International, Crawley, United Kingdom.
[96] Varian Vacuum Products 1997/1998 Catalog, Varian Vacuum Products Lexington, Lexington, MA, USA.
[97] Kurt J., Lesker co., Vacuum Products Catalog 6, Clairton PA, USA.
[98] Alcatel Product Catalog, Paris, France.
[99] Leybold Vacuum Complete Catalogue, Cologne, Germany.
[100] Caburn MDC Vacuum components 1997/98 Catalogue, Caburn-MDC Limited, Glynde, East Sussex, United Kingdom.

[101] Vacuum Generators Products Catalog, Hastings, East Sussex, England.
[102] NOBLING, R., CIVELEKOGLU, Y., POVH, B., SCHVALM, D., TRAXEL, K., Nucl. Instr. and Meth. **130** (1975) 325.
[103] KNEIS, H., MARTIN, B., NOBLING, R., POVH, B., TRAXEL, K., Nucl. Instr. and Meth. **197** (1982) 79.
[104] SCHERER, J., BRAUN-DULLAEUS, K.-U., TRAXEL, K., Nucl. Instr. and Meth. **B30** (1988) 265.
[105] DAVIES, J.A., LENNARD, W.N., MITCHELL, I.V., in Handbook of Modern Ion Beam Materials Analysis (TESMER, J.R., NASTASI, M., BARBOUR, J.C., MAGGIORE C.J., MAYER, J.W., Eds), Materials Research Society (MRS), Pittsburgh (1995) 343.
[106] Canberra Nuclear Instruments Catalog Edition Nine, Canberra Industries Inc., Meriden CT, USA.
[107] OXFORD Systems, Instruments and Components — Catalog, Fifth Edition, Oxford Instruments Inc., Nuclear Measurements Group, Oak Ridge, TN, USA.
[108] TAKAI, M., MIMURA, R., SAWARAGI, H., AIHARA, R., Scanning Microsc. **7** (1993) 815.
[109] PARK, Y.K., et al., Nucl. Instr. and Meth. **B148** (1999) 25.
[110] KNAPP, J.A., BRICE, D.K., BANKS, J.C., Nucl. Instr. and Meth. **B108** (1996) 324.
[111] BANKS, J.C., et al., Nucl. Instr. and Meth. **B136/138** (1998) 1223.
[112] JANICKI, C., et al., Nucl. Instr. and Meth. **B34** (1988) 483.
[113] WHITLOW, H.J., in High Energy and Heavy Ion Beams in Materials Analysis (TESMER, J.R., et al., Ed.), Materials Research Society (MRS), Pittsburgh (1990), 243.
[114] MENDENHALL, M.H., WELLER, R.A., Nucl. Instr. and Meth. **B47** (1990) 193.
[115] MENDENHALL, H.M., WELLER, R.A., Nucl. Instr. and Meth. **B59/60** (1991) 120.
[116] PÁSZTI, F., PARK, Y.K., TAKAI, M., Nucl. Instr. and Meth. **B130** (1997) 247.
[117] DOLLINGER, G., Nucl. Instr. and Meth. **B79** (1993) 513.
[118] BOERMA, D.O., ARNOLDBIK, W.M., WOLFSWINKEL, W., Mat. Sci. Forum **248/249** (1997) 451.
[119] ARNOLDBIK, W.M., et al., Nucl. Instr. and Meth. **B118** (1996) 566.
[120] TROMP, R.M., et al., Rev. Sci. Instrum. **62** (1991) 2679.
[121] SIMON, A., PÁSZTI, F., UZONYI, I., MANUABA, A., KISS, Á.Z., Nucl. Instr. and Meth. **B136/138** (1988) 350.
[122] ORTEC Experiments in Nuclear Science, AN34, Laboratory Manual, 3rd Ed., 1984., Revised, EG&G ORTEC, Oak Ridge.
[123] Canberra Laboratory Manual, Canberra Industries, Meriden, USA.
[124] ZIEGLER, J.F., BAGLIN, J.E.E., J. Appl. Phys. **42** (1971) 2031.
[125] FOSTER, C., et al., Radiat. Eff. **16** (1972) 139.
[126] BEHRISCH, R., SCHERZER, B.M.U., Thin Solid Films **19** (1973) 247.
[127] VAN WIJNGAARDEN, A., MIREMADI, B., BAYLIS, W.E., Can. J. Phys. **49** (1971) 2440.
[128] CHU, W.K., ZIEGLER, J.F., J. Appl. Phys. **46** (1975) 2768.
[129] ZIEGLER, J.F., LEWER, R.F., HIRNOVEN, J.K., Ion Beam Surface Layer Analysis, Plenum, New York (1976) 163.
[130] BORGESEN, P., HARRIS, J.M., SCHERZER, B.M.U., RADC-TR-76–182.
[131] BRICE, D.K., Thin Solid Films **19** (1973) 121.
[132] WEBER, A., MOMMSEN, H., Nucl. Instr. and Meth. **204** (1083) 559.
[133] SAUNDERS, P.A., ZIEGLER, J.F., Nucl. Instr. and Meth. **218** (1983) 67.
[134] BORGESEN, P., BEHRISCH, R., SCHERZER, B.M.V., Appl. Phys. **A27** (1982) 183.
[135] KIDO, Y., OSO, Y., Nucl. Instr. and Meth. **B9** (1985) 291.
[136] KIDO, Y., et al., J., Appl. Phys. **58** (1985) 3044.
[137] KIDO, Y., KAWAMOTO, J., J., Appl. Phys. **61** (1987) 956.
[138] DOOLITTLE, L.R., Nucl. Instr. and Meth. **B9** (1985) 344.
[139] COHEN, B.K., FINK, C.L., DEGNAN, J.H., J., Appl. Phys. **43** (1972) 19.

[140] MOORE, J.A., MITCHELL, I.V., HOLLIS, M.J., DAVIES, J.A., HOWE, L.M., J., Appl. Phys. **46** (1975) 52.
[141] DOYLE, B.L., PEERCY, P.S., Appl. Phys. Lett. **34** (1979) 811.
[142] BLANPAIN, B., RÉVÉSZ, P., DOOLITTLE, L.R., PURSER, K.H., MAYER, J.W., Nucl. Instr. and Meth. **B34** (1988) 459.
[143] VÍZKELETHY, G., Nucl. Instr. and Meth. **B45** (1990) 1.
[144] SAARILAHTI, J., RAUHALA, E., Nucl. Instr. and Meth. **B64** (1992) 734.
[145] KÓTAI, E., Nucl. Instr. and Meth **B85** (1994) 588.
[146] RAJCHEl, B. Nucl. Instr. and Meth. **B113** (1996) 300.
[147] LEWIS, M.B., Nucl. Instr. and Meth. **190** (1981) 605.
[148] RAUHALA, E., J. Appl. Phys. **56** (1984) 3324.
[149] ERIDON, J.M., WAS, G.S., Nucl. Instr. and Meth. **B9** (1985) 505.
[150] BUTTLER, J.W., Nucl. Instr. and Meth. **B15** (1986) 232.
[151] DOOLITTLE, L.R., Nucl. Instr. and Meth. **B15** (1986) 227.
[152] BARRADAS, N.P., JEYNES, C., WEBB, R.P, Appl. Phys. Lett. **71** (1997) 291.
[153] SZILÁGYI., E., PÁSZTI, F., Nucl. Instr. and Meth. **B85** (1994) 616.
[154] ITOH, Y., et al., Nucl. Instr. and Meth. **B117** (1996) 161.
[155] MAYER, M., Report IPP 9/113, Garching 1997.
[156] STEINBAUER, E., BAUER, P., BIERSACK, J., Nucl. Instr. and Meth. **B45** (1990) 171.
[157] BAUER, P., STEINBAUER, E., BIERSACK, J., Nucl. Instr. and Meth. **B79** (1993) 443.
[158] GARTNER, K., Nucl. Instr. and Meth. **B132** (1997) 147.
[159] KÓTAI, E., Application of Accelerators in Research and Industry (Proc. Fourteenth Int. Conf. Denton, 1996 (DUGGAN, J.L., MORGAN, I.L., Eds) AIP CP **392**, AIP Press, New York (1997) 631.
[160] KLING, A., Nucl. Instr. and Meth. **B. 102** (1995) 141.
[161] STRATHMAN, M.D., Application of Accelerators in Research and Industry (Proc. Fourteenth Int. Conf. Denton, 1996 (DUGGAN, J.L., MORGAN, I.L., Eds) AIP CP **392**, AIP Press, New York (1997) 643.
[162] BRIJS, B., DELEU, J., DE COSTER, W., WILS, D., VANDERVORST, W., Application of Accelerators in Research and Industry (Proc. Fourteenth Int. Conf. Denton, 1996 (DUGGAN, J.L., MORGAN, I.L., Eds) AIP CP **392**, AIP Press, New York (1997) 673.
[163] SIGMABASE, Idaho State University, Physics Department, Pocatello, Idaho, USA.
[164] SCHIETTEKATTE, F., ROSS, G., Application of Accelerators in Research and Industry (Proc. Fourteenth Int. Conf. Denton, 1996 (DUGGAN, J.L., MORGAN, I.L., Eds) AIP CP **392**, AIP Press, New York (1997) 711.
[165] VICKRIDGE, I., Nucl. Instr. and Meth. **B45** (1990) 6.
[166] HILL, R.W., Phys. Rev. **90** (1953) 845.
[167] SILVERSTEIN, E.A., SALISBURY, S.R., HARDIE, G., OPPLIGER, L.D., Phys.Rev. **124** (1961) 868.
[168] LEAVITT, J.A., et al., Nucl. Instr. and Meth. **B44** (1990) 260.
[169] ANDERSEN, H.H., BESENBACKER, F., LOFTAGER, P., MÜLLER, W., Phys. Rev. **A21** (1980) 1891.
[170] L'ECUYER, J., DAVIES, J.A., MATSUNAMI, N., Nucl. Instr. and Meth. **160** (1979) 337.
[171] MACDONALD, J.R., DAVIES, J.A., JACKMAN, T.E., FELDMAN, L.C., J. Appl. Phys. **54** (1983) 1800.
[172] CAMERON, J.R., Phys. Rev. **90** (1953) 839.
[173] KNOX, J.M., MCLEOD, R.J., MAYO, D.R., QIAN, X., Nucl. Instr. and Meth. **B45** (1990) 26.
[174] SZILÁGYI, E., PÁSZTI, F., MANUABA, A., HAJDU, C., KÓTAI, E., Nucl. Instr. and Meth. **B43** (1989) 502.
[175] BAGLIN, J.E.E., KELLOCK, A.J., CROCKETT, M.A., SHIH, A.H., Nucl. Instr. and Meth. **B64** (1992) 469.

[176] QUILLET, V., ABEL, F., SCHOTT, M., Nucl. Instr. and Meth. **B83** (1993) 47.
[177] ZIEGLER, J.F., Helium Stopping Powers and Ranges in All Elements, Pergamon Press, Oxford (1977).
[178] ZIEGLER, J.F., BIERSACK, J.P., LITTMARK, U., Stopping and Ranges of Ions in Solids Pergamon Press, New York (1985).
[179] BRAGG, W.H., KLEEMAN, R., Phil. Mag. **10** (1905) 318.
[180] LINDHARD, J., SCHARFF, M.K., Dan. Vidensk. Sesk. Mat. Fys. Medd. **28** (1954) 8.
[181] WILLIAMS, J.S., MÜLLER, W., Nucl. Instr. and Meth **157** (1978) 213.
[182] ZOLNAI, L. SZABÓ, GY., Nucl. Instr. and Meth. **B34** (1988) 118.

CONTRIBUTORS TO DRAFTING AND REVIEW

Budnar, M.	Josef Stefan Institute, Slovenia
Calmpbell, J.	University of Guelph, Canada
Fazinic, S.	International Atomic Energy Agency
Jakšić , M.	Rudjer Bošković Institute, Croatia
Kobzev, A.	JINR, Russian Federation
Kótai, A.	KFKI- Research Institute for Particle and Nuclear Physics, Hungary
Lanford, W.	University of Albany, United States of America
Orlic, I.	ANSTO, Australia
Pászti, F.	KFKI- Research Institute for Particle and Nuclear Physics, Hungary
Rauhala, E.	University of Helsinki, Finland
Turos, A.	Institute of Nuclear Studies, Poland